Raman spectroscopy for unlabelled detection and quantification of drugs in tissue

By Nathan P Woodhouse

Supervised by Prof. Ioan Notingher

Thesis submitted to the University of Nottingham

for the degree of Doctor of Philosophy

June 2022

School of Physics and Astronomy

Abstract

Raman spectroscopy is an optical analysis technique for chemical analysis of samples. In this thesis, we have assessed its applicability in quantitative detection of drugs within animal tissue. This involved the design, construction, and optimisation of a Raman microscope for this application, considering the specific requirements of the samples.

A Raman microscope was designed to efficiently measure Raman spectra from thin (16 µm) tissue sections with >1 cm field-of-view. Two of these were built, one with a 671 nm and one with a 785 nm wavelength excitation laser, to assess the relative benefits of each for drug detection specifically in the Raman silent region of the Raman spectrum (~ 1800 – 2800 cm^{-1}), in both low and highly autofluorescing tissue. These instruments, and the acquisition parameters used, were optimised to maximise Raman throughput while minimising the effects of noise on the measurements from autofluorescence.

Control tissue cryosections with drug solution pipetted on top was used as a feasibility test for qualitative detection of drugs in tissue. A model for prediction of the spectra and required measurement times for detection of different drug/tissue combinations at different concentrations was developed. The most promising drugs from this study were then used to generate mimetic tissue models, homogenous mixtures of drug and tissue with known mass ratios, to assess the quantifiability of Raman spectroscopy in drug detection in tissue. Detection limits as low as 18 µg/g were calculated for ponatinib in rat brain mimetic tissue models with 2-hour measurement times, and 34 µg/g for the ponatinib in rat liver mimetic tissue models.

Publication

Woodhouse, N.; Majer, J; Marshall, P; Hood, S; Notingher, I. “Quantification of drugs in brain and liver mimetic tissue models using Raman spectroscopy”, Appl. Spectrosc., 2022 (Accepted for publication)

Conference Contributions

Facilitating prolonged Raman mapping in thin biological samples, *Bioimaging Expertise Network (BEN) Symposium*, 2019

Raman Mapping of Thin Tissue Sections (Poster), *Infrared and Raman Discussion Group (IRDG) student meeting*, 2019

Raman Spectroscopy of drugs in spiked tissue samples, *Bioimaging Expertise Network (BEN) Symposium*, 2021

Raman Spectroscopy of silent region – labelled drugs in tissue, *Drug Metabolism Discussion Group (DMDG) open meeting*, 2021

Quantification of drugs in brain and liver mimetic tissue models using spontaneous Raman spectroscopy (RS), *Society for Applied Spectroscopy (SAS) – Coblenz virtual Conference*, 2022

Acknowledgments

I would like to thank my supervisor Professor Ioan Notingher for the opportunity to study and perform research in his group. His guidance and input have turned basic thoughts and ideas into good science, without which I would have been completely lost. I am also thankful for the having opportunity to design, build and operate instrumentation that would have been impossible outside of academia.

Thanks to Steve, Pete and Jan at GSK, who have been fundamentally essential in doing the work in this thesis. They provided sample generation and analysis facilities that were completely out of our reach in the school of Physics, they have provided a biology and pharmaceutical viewpoint on the research done from a biology and mass spectrometry perspective that we did not have, which has proven essential.

Thanks to the other members of the Biophotonics group in Nottingham. They have always been there to help, be it in the form of programming, choosing the right filters for a microscope, and even light plumbing. Without their assistance, I would still be frantically searching the labs for the right metric posts to attach different mirror mounts together. There have been too many to name individually, but I appreciate all of what each of them have done.

Finally, thanks to my friends and family, who have always been there for anything and everything else. That’s quite a lot when you think about it.

Table of Contents

1. List of Abbreviations

Abbreviation	**Definition**
CARS	*Coherent anti-Stokes Raman spectroscopy*
CCD	*Charge-coupled device*
CW	*Continuous wave*
DESI	*Desorption electrospray ionisation*
FOV	*Field of view*
FWHM	*Full-width half-maximum*
GFP	*Green fluorescent protein*
H&E	*Haematoxylin and eosin*
HPLC	*High-performance liquid chromatography*
LC-MS/MS	*Liquid chromatography – tandem mass spectrometry*
MALDI	*Matrix-assisted laser desorption ionisation*
MALDI-TOF	*Matrix-assisted laser desorption ionisation – time-of-flight*
MSI	*Mass spectrometry imaging*
MS/MS	*Tandem mass spectrometry*
NIR	*Near-infrared*
PCA	*Principal component analysis*
PLS	*Partial least squares*
SERS	*Surface-enhanced Raman spectroscopy*
SIMS	*Secondary ion mass spectrometry*
SNR	*Signal to noise ratio*
SORS	*Spatially-offset Raman spectroscopy*
SRS	*Stimulated Raman Spectroscopy*

2. Introduction

The aim of this project was to design and build an optimised Raman microscope for measuring drug concentrations in tissue samples. The instrument was then used to measure drug-tissue analogue models, determining the sensitivity of the microscope for drug delivery applications, as well as determining the ability to make quantitative measurements of drugs in tissue.

2.1. Drug delivery

Drug delivery is a field of research studying the pharmacokinetics, metabolism and excretion of drugs introduced into an organism. It is an integral component of assessment of the efficacy of novel drugs, as the applicability of a drug explicitly requires the drug to reach the site of action within the organism. The experimental action of a drug is irrelevant if, when introduced into a patient, its metabolism pathway never passes the intended target of the drug.

In recent years, innovative drug delivery systems have been at the forefront of pharmaceutical research, including nanoparticle-based carriers, stimuli-responsive systems and biomimetic drug delivery systems[1]. These methods exploit the biomechanics and pharmacokinetics of the body to optimise drug delivery to the target site in the body. They have also been used to bypass otherwise challenging areas of the body, for example penetrating the blood-brain barrier[2]. Stimuli-responsive systems can be used to manually control the activation of the drug, using external or internal methods at the target site. This maximises action at the target, while minimising the risk of toxicity in the rest of the body. This application is especially useful in cancer drug delivery, where drug toxicity due to accumulation outside of the target tumour is of great concern[3]. The introduction of new drug delivery systems also, in utilizing fundamentally different drug structures, enables the use of different techniques in the analysis of drug delivery within dosed organisms. For example, gold nanoparticles operate as stimuli-responsive drug carriers[4], but also act as contrast agents in surface-enhanced Raman spectroscopy[5,6].

Analysis of drug delivery within animals is performed at several length scales to determine the effect of different-scale transport and diffusion mechanisms within the body. Methods range from whole-body compartmental models down to super resolution scanning techniques measuring drug distribution at the organelle level. As biological systems operate in unique ways at all these scales, means to measure drug distribution at all these levels are also necessary to fully understand the pathways and mechanisms involved after drug introduction to the recipient.

Verification of drug delivery to the intended target is only one application of spatially-resolved drug measurement techniques. Another is in drug toxicity studies. This is the study of the effects of the drug accumulating in areas and at concentrations that cause negative consequences to the recipient. Toxicity studies determine the effects of overexposure to the drug on different parts of the body, which itself requires knowledge of where the drug accumulates. This is one example of a need for large-scale analysis of drug distribution within the body, outside of the specific region where the intended target is located.

Another application for spectrometric techniques in drug distribution measurement is analysis of the metabolism of the drug within the body. A key capability of a novel drug is the excretion of the drug and drug products after target engagement. With techniques like Raman spectroscopy, molecular information about the target site is available beyond drug concentration. Structural and molecular changes to the tissue may be assessed, the drug and drug degradation products can be analysed, and a greater understanding of the real effects on the drug target can be acquired.

2.2. Key considerations when selecting a drug detection method

As different drug detection methodologies vary considerably in their relative strengths, the choice of detection methodology depends on the specific application. Several of the primary attributes are listed below.

Sensitivity

The sensitivity of the methodology is the ability to detect low amounts of the drug of interest, either by mass or by volume. For drugs with novel transport mechanisms, high sensitivity is required as the sites of accumulation are not well known beforehand. For high resolution imaging, high sensitivity to low absolute masses of the drug is necessary due to the low sampling volumes involved, but the concentrations in small areas of high accumulation may be sufficiently high that the sensitivity to drug concentration is not as important.

Labelling

Label-free drug detection is generally preferred to labelled drug detection, depending on the label being used. This is because large protein markers may affect the drug transit through transport channels of the organism, resulting in non-representative drug distribution. For example, green fluorescent protein (GFP), has a mass of 27 kDa, while some drugs have molecular masses of substantially less than 1 kDa (caffeine, acetaminophen, for example). The labels themselves also may degrade over time, temporally limiting the sensitivity of the instrument to the drug. This is the case for radiolabels and some fluorophores. In certain tissues, the optical response of a labelled drug to the instrument may overlap with the autofluorescence intrinsic to the organism, reducing the signal-to-noise ratio (SNR) of the method.

Destructiveness

Destructive detection techniques are those in which the organism is fundamentally altered by the detection process. This is the case in chromatographic techniques, where the sample is destroyed in the separation process, or in mass spectrometry, where the molecules comprising the sample are ionised and detected individually in the spectrometer. Non-destructive techniques are necessary for live imaging of non-fixed samples, be they cell cultures or live animals. They also enable repeated measurements of samples. This allows both time-course measurements of samples and allows for consecutive measurement of the same sample using different methodologies. These factors enable prolonged measurements and minimise the amount of the sample required, which is crucial for reducing the number of animals required in studies.

Drug and tissue of interest

Different detection methodologies are sensitive to different drugs and environments. Depending on the methodology, there may be specific molecular features that highly improve the detection abilities of different techniques, be they specific molecular bonds as in Raman spectroscopy, isotopic mass markers as in mass spectrometry, or drugs that are readily compatible with specific markers.

The choice of tissue is also an important consideration. Different lipid content, autofluorescence characteristics, or even structural composition making sectioning difficult all play a part in predicting which methodology will be applicable for what sample.

Detection Speed

In vivo studies have inherently limited time constraints that require certain detection speeds for the methodology to be applicable. As the measured biological system is still dynamic at the time of measurement, the drug distribution is subject to change over long-time scales, requiring fast measurement. For imaging techniques, this is even more necessary, as the effective number of measurements to generate an image is typically greater than 10^4. High-speed scanning techniques like confocal fluorescence microscopy and coherent Raman spectroscopy enable scanning at sampling times of milliseconds or less, which combined with their non-destructive nature and high spatial resolution, are ideal for live cell studies[7–11]. For single-point measurements or whole-organ measurements, the speed is less important as the entire sample is measured simultaneously.

For fixed samples the speed of the detection method is not an integral component of determining the accuracy of the results, but still affects the overall instrument throughput and therefore utility of the method.

Spatial Resolution

Analysis of drug kinetics within the body is performed at several length scales to determine the effect of different-scale transport and diffusion mechanisms within the body. Methods range from whole-body compartmental models down to super resolution scanning techniques measuring drug distribution at the organelle level. As biological systems operate at all these scales, means to measure drug distribution at all these levels is also necessary to fully understand the pathways and mechanisms involved after drug application.

The choice of instrument based on its spatial resolution depends on what scale the drug distribution is to be measured at. Certain detection methodologies have intrinsic resolution limits that preclude them from measuring drug distribution at intracellular scales, making them only viable for organ and sub-organ level distribution analysis at the lowest. Conversely, microscopy methods that have heavily increased sensitivity and spatial resolution as a result of using objectives with very high numerical apertures, are essentially limited in the largest scales at which they can measure drug distribution. Their very low sampling volumes result in either very long scanning times or the requirement of undersampling in large samples to determine the distribution across the entire sample.

Quantifiability

The ability to measure absolute drug concentration distribution is integral to different studies involving drug detection, by being able to determine not only relative uptake in different regions, but also being able to determine if the drug uptake at the targeted site was sufficient and that the uptake everywhere else was at safe levels[12].

The quantifiability of a methodology is not binary, there are several different levels. From absolute drug concentration in chromatographic methods, to relative concentration distributions that can be calibrated to standard samples on a per-instrument basis as in Raman spectroscopy, to relative concentration distributions that can be calibrated on a per-sample basis as in mass spectrometry. The limit of quantification will also always be higher than the limit of detection, which again must be considered when selecting a detection methodology.

The most common methodologies used for drug delivery studies are listed in the following section. Different Raman spectroscopy techniques and their applications in drug detection and drug delivery are discussed in more detail in Chapter 3.

2.3. Current methods of drug detection in tissue

Chromatography

Chromatography refers to a family of chemical analysis techniques where samples are physically separated into their constituent components. High-performance liquid chromatography (HPLC) is a chromatographic method where the separation phase occurs in a liquid state.

This is a chemical analysis technique that separates a mixture of chemicals into its individual components. The separation is performed by flowing the mixture through a column containing a material or structure that restricts the flow of the liquid. This is generally an adsorbent material. The interaction of the column with the components of the analyte varies, individually varying the flow rate of the components and thus spatially separating them. The output of chromatography is a series of separated components, which can then be individually analysed and quantified. As the sample is physically separated into its components, they can be individually analysed using other methods, as is done in liquid chromatography – tandem mass spectrometry (LC-MS/MS), where the separated product of LC is then analysed using mass spectrometry.

Chromatographic methods are extremely sensitive to low concentrations of drugs, as the drug itself can be separated fully from the biological material. Relevant drugs have been measured at concentrations as low as 1.5 ng/mL in blood plasma[13]. The limitation of variants of LC is that do not retain spatial information; the region of interest must be physically isolated from the bulk of the sample to be measured on its own. The minimum volume of the sample is also relatively large, with a lower limit of ~5 µL typically used[14]. On an organ-level scale this is sufficient, as for example rat organs are typically of the order of 1000 µL[15]. However, for cell-level measurements, a sampling volume of order of 10 μm^3 (10^{-8} µL) is needed to ensure single-cell level discrimination. Larger sampling volumes risk overlap with neighbouring cells, reducing the specificity of the measurement. Subcellular sampling volumes depend on the specific subcellular structure/organelle of interest.

Autoradiography

Autoradiography is a method of tracking drug distribution within tissue by means of a radiolabel incorporated into the drug molecule prior to dosing. Tissue from the animal is then sectioned, dehydrated, and mounted to a phosphor detector. The decay products from the radiolabel are then detected in a spatially resolved way, enabling mapping the drug concentration within the tissue.

This method has a spatial resolution in the range of 30 µm[16], depending on the detector used. As the method is a direct imaging technique, not a scanning technique, the acquisition time is not dependant on the per-pixel acquisition time but the pixel density of the sensor and the sensitivity of the system to radiolabel being used. This enables whole-body sections to be measured rapidly, which in turn allows for simultaneous sub-organ and whole-body level drug distribution measurement.

Quantification can be performed, by including a calibration standard ladder of radiolabel concentrations in parallel to the imaged sample. This enables both quantification of the concentration of isotopes within the tissue, and calibration of the system for signal decay over time. Radiolabelled drugs have been measured at concentrations as low as 0.03 µg/g measured in rat brain, and as low as 0.037 µg/g in rat kidney[17].

As it is exclusively detecting the presence of the radiolabel, not the drug itself, it is impossible to discriminate the drug from its metabolites using this technique. Some radiolabels are also prone to being separated from the drug and attaching to other molecules, like ^{3}H with water, resulting in erroneous drug distribution images[18,19]. The active decay of the radiolabels also imposes time limitations on the dosing schedule being assessed, along with the timing of the imaging itself. Other imaging techniques can be performed on the sample with much more flexibility between excision and measurement. Additionally, the presence and procurement of radiolabels makes autoradiography more technically difficult to accomplish safely.

Mass Spectrometry

Mass spectrometry is a family of analytical techniques for assessing the molecular composition of materials. It has seen widespread use in pharmacokinetics, where its high sensitivity can be used to detect and quantify drug molecules in biological samples. More recently, mass spectrometry imaging (MSI), a group of spatially resolved mass spectrometry techniques, has been used to map the distribution of drugs in biological materials.

Mass spectrometry, generally, is a means of analysing a material by measuring the relative molecular masses of the constituent molecules or molecular fragments of a material. The mass spectrum can then be processed to determine the molecular composition of a material, either by searching for spectral fingerprints belonging to known molecules, or by determining the molecular composition of a material purely from the mass spectrum itself.

Mass spectrometry is performed by ionisation of the sample of interest. This is achieved through different means, from ion beams as in secondary-ion mass spectrometry (SIMS), charge transfer from an electrically charged liquid as in desorption electrospray ionisation (DESI), or high energy laser absorption as in matrix-assisted laser desorption ionisation (MALDI). Once the sample has been ionised, a plume of ions from the sample pass into a mass spectrometer, where the molecules are discriminated by electrical or magnetic manipulation using their differing mass/charge ratio. The specific requirements of an experiment determine which ionisation method and which mass spectrometry method are to be used. The specific MSI methods currently of interest for drug delivery research are described, along with their applications, below.

Tandem Mass Spectrometry (MS/MS)

MS/MS is a mass spectrometry technique for measuring the mass spectrum of specific components of an analyte. The analyte is ionised and separated by mass/charge ratio by standard mass spectrometry. From this, one specific mass/charge ratio ion of interest is diverted to another section of the machine, where it is fragmented into smaller ions. These ions are then sent into another mass spectrometer for further analysis. This method allows the acquisition of the mass spectra of specific components of a sample, reducing background from contaminants and sample preparation compounds.

Liquid Chromatography – Tandem Mass Spectrometry (LC-MS/MS)

LC-MS/MS is a serial combination of LC and MS/MS. The sample is first separated by LC and then individual components are analysed by MS/MS. This method requires relatively high sample volumes (order of whole rat organ), so using it for sub-organ mapping is not feasible. It has, however, been used for producing a calibration curve for quantifying Matrix-assisted laser desorption-ionisation mass spectrometry (MALDI-MS) data [14].

Matrix assisted laser desorption ionisation time-of-flight mass spectrometry (MALDI-TOF MS)

MALDI-TOF MS imaging (MALDI-TOF MSI, abbreviated here as MALDI for simplicity) is a mapping technique that enables spatially resolved mass spectrometry of the surface and shallow bulk of a sample (up to ~ 40 µm)[20] , with lateral resolution as low as ~5µm[21].

MALDI is generally[22] performed by ionising a sample using a pulsed laser. The ionised ablated material is then analysed using time-of-flight (TOF) spectrometry. TOF spectrometry is a method of separating and measuring the constituent mass fragments of a material. The ionised material is sent through an electric field, applying an identical force to all the ions. The acceleration of the ions when subject to the same force differs based on the mass of the individual ion, so the TOF of heavier ions through the spectrometer is longer than that of the lighter ions. The ions are then measured using a microchannel plate detector. The mass spectrum is generated by calibrating the time series output of the detector to a mass series. Imaging is performed by scanning the laser over the sample and individually measuring the mass spectrum of each position within the sample. The sample itself is first sprayed with a matrix solution, which facilitates ablation of the sample by the laser.

This matrix is then hit with a pulsed laser, ablating part of the matrix/sample mixture to be sent into the TOF-MS system for spectrometry.

While the laser optics used to ablate the sample can be diffraction-limited, the practical limit of spatial resolution is determined by the matrix application step of the process. The dissolution of the sample into the aqueous matrix solution inevitably causes some lateral drift, where the sample molecules disperse within the matrix solution before the solvent evaporates, and the matrix crystallises.

While quantitative studies of drug delivery in dosed animals using MALDI have been performed [23], the calibration process requires a calibration standard performed for every sample. This is because the matrix application stage is insufficiently consistent between samples and heavily affects the signal strength from the constituent components of the sample. The matrix application stage involves uniformly spraying the entire sample with the matrix solution, allowing it to crystallise, then re-spraying the sample multiple times depending on the specific experiment being performed. This application method is uniform across the sample, but minute differences in the spraying technique and geometry between samples results in measured mass spectra signal strength between samples. This makes instrument-level quantification calibration impossible.

Quantification of drug distribution using MALDI therefore requires a calibration sample that has been prepared for imaging at the same time as the actual sample. This calibration sample can be either an undosed sample of the same tissue type that has had a known concentration of drug introduced, or an adjacent section of the same sample for use in LC-MS/MS. Using the first method, the MALDI drug signal can be calibrated to the concentration curve of the calibration sample. The second method involves homogenising the adjacent section and using LC/MS to determine the absolute mass of the drug of interest within the section. This value can then be used to normalise the MALDI image, based on the assumption that the same mass of drug will be also present in the MALDI section[23].

MALDI has recently become much more popular in studying drug delivery in organs, as it enables spatially resolved label-free drug detection in tissue. This is a strong advantage over other LC and MS/MS, which are more sensitive and much easier to quantify, but have no real mapping ability. MALDI enables label-free drug mapping on a sub-organ level, with a spatial resolution generally in the range of >30 µm, but has been achieved as low as 5 µm in certain tissues, using certain matrices[24,25]. As the method is destructive, the sensitivity of the technique is limited by the volume of each measurement – a 50 µm spot measurement on a thin tissue section will have ~100 times the mass and therefore drug content relative to the same sample measured with a 5 µm spot due to the decreased area of tissue being ablated[26,27].

The minimum detectable concentration of the drug of interest is entirely dependent on both the drug of interest, and the tissue the drug is to be detected within. Drug concentrations on the order of 1 µg/g have been quantitatively detected with an predictive error of ~10%[28].

The detection limit of a specific drug within a specific tissue is dependent on the chemical interaction between the drug and the tissue prior to measurement. Some drug-tissue interactions inhibit the probability of ionisation, reducing the sensitivity of the overall method. Conformal changes to the drug molecule itself during metabolism may affect the overall structure of the drug molecule, resulting in different ionised fragments being measured. The mass range of MALDI is very wide, ranging from ~100-100 000 Da[29,30]. This enables the measurement of most relevant molecules in pharmacokinetics, such as proteins, lipids, drugs, and metabolites.

As a scanning technique, the image acquisition rate of an entire sample depends on the sample size, the spatial resolution of the scan, and the per-pixel acquisition time. While the first two factors are entirely dependent on the specific experiment, the pixel acquisition rate is typically limited by the desired sensitivity of the system, sensor readout electronics and the scanning mechanism of the mass spectrometer. Speeds in the 10s of pixels per second are standard, with some systems capable of measuring over 100 pixels/s[31].

Desorption electrospray ionisation (DESI) mass spectrometry

Desorption electrospray ionisation is a sample ionisation technique that sprays the sample with an electrically charged liquid, which ionises the sample. Ionised molecules from the sample are desorbed by the spraying process, and directed to the mass spectrometer for analysis[32].

DESI has the benefit over other MSI ionisation techniques that it requires no previous sample preparation, and that the measurement process can be performed at ambient conditions, unlike other methods which require the ablation process to be done at vacuum.

The spatial resolution of DESI is limited by the spraying process itself, typically a resolution of 40 µm can be achieved[33]. The dynamics of the spraying and collection process limits the spatial resolution, unlike in other ionisation methods where the absolute theoretical limit of spatial resolution is determined by the ion beam or laser optics used.

DESI has been used in quantitative drug detection studies previously, with detection limits as low as 2.5 µg/g reported[34].

Secondary-ion mass spectrometry (SIMS)

Secondary-ion mass spectrometry is a sample ionisation technique that sputters the surface of the sample with a focussed ion beam, both ionising and ablating the sample simultaneously. This technique has the smallest spatial resolution of MSI techniques, as the limit of the spatial resolution is determined by the ion beam optics[35]. Spatial resolutions below 100nm are readily achievable[36]. In addition, as the technique is ablative and has a very small spatial resolution, consecutive measurements of a single surface can be used to produce 3D maps of molecular content, removing thin layers of tissue during each pass. As the spatial resolution of SIMS is purely determined by the ion optics, the spot size can easily be manipulated. This enables large scale, poor resolution mapping of whole samples followed by nanoscale resolution mapping of certain regions of interest within the sample. This enables the acquisition speed of low-resolution scanning to be combined with the high resolution of small spot scanning.

Relative to DESI and MALDI, the ionisation method of SIMS limits the range of molecules that can be detected. While it is capable of detecting lipids at attomolar concentrations[37], proteins, peptides and nucleotides are less detectable relative to in MALDI or DESI[38]. The differences in ionisability of the different methods is primarily due to the differences in mass between the molecules, and also of the ability of the matrix to extract the different molecules from the sample in the case of MALDI.

Limitations of MSI in drug delivery analysis

As an inherently destructive technique, *in vivo* applications are not readily feasible. As the molecules of interest are also destroyed by the measurement process, the sensitivity to the molecule of interest is fundamentally limited to the signal that can be obtained in one measurement. Unlike some non-destructive optical techniques, where light from the sample is measured, direct removal and analysis of the sample during the ablation process removes the possibility to simply repeat measurements and combine the signals to increase the signal-to-noise ratio (SNR) and thus detection limit of the sample. To increase the signal using a destructive technique, more sample must be analysed. This limits the spatial resolution of the method by forcing increased sampling volumes to reach desired detection limits.

Generally, the ionisation procedure is a limiting factor on quantification of the mass spectra produced. Inter-sample differences in this step generally necessitates a per-sample calibration to enable quantitative imaging[39,40]. This increases the imaging time or requires separate quantitative measurements on chromatography devices and necessitates the use of more control tissue for the creation of these reference calibration standards.

Confocal fluorescence microscopy

Confocal fluorescence microscopy is an optical imaging method whereby the molecule of interest is either tagged with a fluorescent marker or is inherently autofluorescent. A laser is focussed into the dosed sample, which excites the marker, causing detectable fluorescence. A lens in the collection pathway of the microscope focusses the fluorescent light onto a spatial filter, typically a pinhole. The light that passes through the pinhole is then re-imaged and detected using a high-speed detector, typically a photomultiplier tube. The pinhole blocks any out of focus light from reaching the detector, reducing background signal. The laser spot is scanned through the sample to generate an image showing the relative accumulation of the fluorescent marker within the sample. The rejection of out-of-focus light also decreases the depth of focus of the microscope, which makes three-dimensional analysis of samples feasible by scanning the laser axially as well as laterally.

As a method of analysing drug delivery, it provides a spatial resolution in the range of ~100-1000 nm, depending on the fluorophore used, the specific imaging techniques and the geometry of the sample itself. Microscopy techniques with sub-diffraction limited spatial resolutions have been shown to be capable of imaging nanoparticles in fixed HeLa cells with sub-100 nm resolution[41], and resolving filaments with diameters of ~9 nm[42], although sub-diffraction limited microscopy methods typically require much more expensive instrumentation and have greater limits on the available fluorophores.

A wide range of fluorescent markers are available, varying in size, from small-molecule based fluorophores[43] to fluorescent proteins with molecular masses greater than 20 kDa. The size of the markers should be taken into consideration for marking small (< 1 kDa) molecules, as large fluorescent markers may affect the activity and kinetics of the drug itself[44]. Other important characteristics affecting choice of label include the absorption and emission spectrum, the mechanism by which the label is added to the molecule of interest, and the photobleaching properties of the label. Photobleaching is the process by which the label is rendered permanently non-fluorescent due to chemical alteration of the label because of the laser illumination[45,46]. This process sets a general upper limit on the number of times a given molecule can fluoresce before becoming undetectable. As a result, the ability to perform repeated measurements in time-series experiments or for higher signal-to-noise ratio are heavily affected by the number of absorption/emission events the label can undergo.

Fluorescence microscopy has been used in drug delivery research as a labelled drug detection method. It has been used to image the distribution of fluorescent nanoparticles in 4T1 cancer cells incubated in a nanoparticle solution of 80 µg/g[47].

While confocal microscopy can be quantitative, it has significant limitations that make it difficult[8]. As the fluorophores themselves degrade with measurement, detection calibration is problematic. The emission wavelength of the label may overlap with the autofluorescent emission spectrum of the biological material being measured in, which must be subtracted from the measurement prior to quantification. Detection of weak light sources is intrinsically susceptible to quantisation noise, which can only be minimised by collection of more light.

3. Raman spectroscopy

Raman spectroscopy is the study of the molecular composition of a sample by measuring the inelastically scattered light from the sample, when illuminated with a typically monochromatic light source. Spontaneous Raman spectroscopy uses a single laser to acquire this information. Other more complex instrumental techniques, like Stimulated Raman spectroscopy (SRS), Coherent anti-Stokes Raman spectroscopy (CARS), and surface-enhanced Raman spectroscopy (SERS) have been used for drug delivery research, as they use additional light sources or specialised substrates to significantly enhance the Raman scattering rate of samples.

3.1. Spontaneous Raman Spectroscopy

Spontaneous Raman spectroscopy is an optical analysis technique that measures inelastically, or Raman, scattered light to acquire chemical information about an analyte. First measured in 1928[48], Raman scattering has been used extensively for chemical analysis of materials. Later inventions of the laser and the charge-coupled device (CCD) detector have led to rapid improvements in the applicability of Raman spectroscopy to the life sciences.

The scattering of a photon by a molecule can be elastic or inelastic. Elastic, or Rayleigh, scattering imposes no net energy transfer between the photon and the molecule, so there is no change in wavelength of the incident photon. Raman scattering, however, does impose a net transfer of energy. The energy transfer is a two-step process, whereby the photon energises the molecule to a ‘virtual’ state in between the current energy state of the molecule and the next energy state. This state very rapidly decays back to the original energy state, but in a different vibrational state. The energy difference between the original and final vibrational state is transferred to or from the photon, which is then emitted from the molecule. For a pictorial description of the process, see Figure 1.

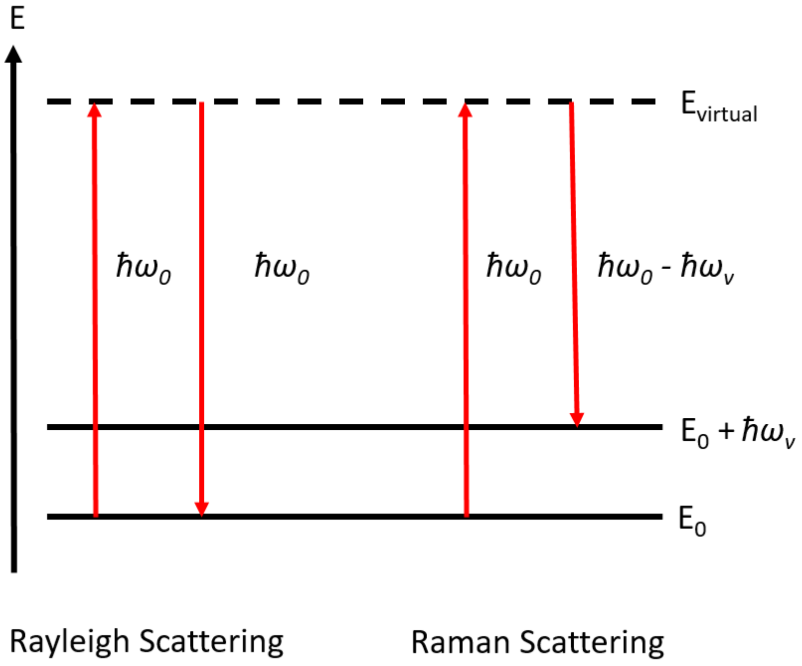

Figure 1: Energy diagram of Rayleigh scattering and Raman scattering. The solid horizontal lines represent the vibrational states of a molecule with ground state energy E_0*, and the dotted line the virtual state. The red arrows show the energy changes in the process. The Raman shift of the photon is represented by* $\hbar\omega_v$*.*

The energy change, or Raman shift, of the photon corresponds to the energy difference between different vibrational modes of the molecule. As such, knowledge about the structure of the molecule can be inferred by analysing the energy differences between different vibrational modes in the molecule. This specifically can be used to interrogate the bonds and functional groups within the molecule.

The Raman spectrum of a sample is generally obtained by illuminating it with monochromatic light. The light scattered from the sample is then analysed using a spectrometer, which spatially separates the light depending on its wavelength and therefore energy. If the energy of the illuminating light is known, the energy difference between that and the scattered light can be used to generate a Raman spectrum. As the Raman scattering process is quantised, the entire net energy transfer from the molecule goes to a single photon, so the absolute energy change in the molecule can be directly measured by measuring the energy difference in the photon. This also means that the

Raman spectrum can be accurately generated by measuring the bulk spectrum of scattered light from the sample as a whole.

A negative energy change in the photon, corresponding to positive changes in the energy of the molecule, is known as Stokes shift. The Raman shift results in the detected light having a longer wavelength than the light incident on the sample. Likewise, Raman scattering causing a negative change in the molecule energy is known as anti-Stokes scattering.

The Raman activity of a particular vibrational mode of a bond is dependent on if the vibrational mode confers a change in the polarisability, α, of the bond. If there is no change in the polarisability, the mode is not Raman active. If there is, the bond is Raman active. The scattering coefficient, $\mu_{S,}$ of a particular vibrational mode is proportional to the square of the induced dipole moment P,

$$P = \alpha E, \qquad (1)$$

where E is the electric field producing the dipole moment, such that

$$\mu_S \propto \alpha^2. \qquad (2)$$

. A vibrational mode causing a change in dipole moment is active in infrared spectroscopy, a related analysis technique.

As most molecules are in the ground vibrational state, it is much more common that the result of Raman scattering is a net increase in the vibrational energy of the molecule.

This means that Stokes Raman scattering is a much more common effect than anti-Stokes scattering in standard conditions. The relative populations of each state determine the relative intensities of each is given by the equation

$$\frac{I_S}{I_{AS}} = \frac{\nu-\nu_i}{\nu+\nu_i} e^{\frac{h\nu_i}{k_B T}}, \tag{3}$$

Where I_S is the intensity of the Stokes Raman scattering, I_{AS} is the intensity of the anti-Stokes Raman scattering, ν is the energy of the ground vibrational state, ν_i is the energy of the raised vibrational state, h is Planck's constant, k_B is Boltzmann's constant, and T is the temperature of the sample[49].

As the two types of scattering are fundamentally measuring the same energy differences, the Stokes spectrum and anti-Stokes spectrum are qualitatively identical but inverted around 0 Raman shift. The benefit of choosing anti-Stokes over Stokes is that most inelastic optical effects result in a negative change in photon energy, so confounding sources of light like autofluorescence are much stronger in the Stokes region of the spectrum. Anti-Stokes Raman spectra are in a different region of the spectrum to standard autofluorescence, so typically have lower noise levels at the cost of reduced signal. Other sources of light like second-harmonic generation and two-photon excitation fluorescence are however present. Stimulated and coherent variants of Raman spectroscopy that amplify the Raman scattering rate of a sample by multiple orders of magnitude often operate in the anti-Stokes region where reduced signal is less of a concern than the issue of other light sources. All our measurements in this project have been performed in the Stokes region of the Raman spectrum.

More sophisticated methods of Raman spectroscopy exist, utilising coherent and/or nonlinear optical techniques to enhance specific Raman bands from a sample. Other methods use specific sample substrates to enhance the Raman signal from a sample. These methods and their application in drug detection in biological systems are described later in the chapter. This project has entirely been performed using spontaneous Raman spectroscopy so, unless otherwise specified, ‘Raman spectroscopy’ refers specifically to spontaneous Raman spectroscopy.

Units of measurement

The standard description of a Raman shift is in its wavenumber, or spatial frequency, with the most commonly used unit being cm^{-1}. The wavenumber of a photon is proportional to its energy, so the Raman shift in cm^{-1} of a measured photon is also proportional to the energy difference between the vibrational modes of the measured molecule. As a measurement of the difference of two energy states, the Raman shift is illumination-wavelength agnostic; the Raman spectrum emitted from a sample using one laser is qualitatively the same as that for another of a different wavelength.

Regions of the Raman spectrum

In biological applications, the Raman spectrum of a sample is typically segregated into three regions, defined by the Raman bands that are present in those spectral regions. The specific regions are not rigorously defined, so their ranges given here are approximate.

Fingerprint region

The fingerprint region, typically defined as the range ~600 – 1800 cm^{-1}, is the range in which most biologically common molecular bonds have Raman bands.

Silent region

The range of ~1800 – 2800 cm^{-1} is known as the silent region, due to the general absence of any Raman bands in typical biological materials. Very few molecules naturally present in biological samples have peaks in this area, resulting in the Raman spectrum here looking essentially flat, excluding any autofluorescence. This makes the silent region a very useful asset in choosing Raman tags for a molecule of interest. Bonds that do exhibit Raman features in the silent region include carbon-deuterium (C-D) bonds, which present a range of features depending on the specific group the bond is present in, nitrile groups (C≡N), and alkyne (C≡C) bonds, which exhibit a very sharp single peak in the range of 2080 - 2260 cm^{-1}, with the specific location of the peak dependant on the other groups present in the entire molecule, and presence of multiple adjacent alkyne bonds (C≡C-C≡C)[50]. Carbon-deuterium bonds within larger molecular structures also affect the vibrational modes of these structures, such that the Raman spectrum of deuterated molecules generally shares few Raman bands with the non-deuterated equivalent.

As bonds that are not naturally present in animal tissue , their silent region bands are spectrally separated from the Raman bands of tissue, making the identification of their presence from tagged molecules simpler than the identification of drugs from Raman bands in the fingerprint or high wavenumber region. In heterogeneous materials like tissue, the varying bands intrinsic to the tissue can also make discrimination of overlapping drug bands difficult, both visually and analytically.

High wavenumber region

The high wavenumber region of the Raman spectrum is typically defined as the range ~2800 – 3800 cm^{-1}. This region contains stretching bands from CH_2, CH_3 and O-H bonds and as such is extremely useful in studies of lipids, proteins and in water studies. The bands in this region are broad and smooth, so changes in the large molecules being measured can be inferred from the change in the shape of the bands, unlike in sharper bands from the other regions which are usually analysed by their position in the spectrum and relative strength.

Optical resolution

The lateral spatial resolution of Raman spectroscopy depends entirely on the detection optics. A Raman microscope can measure the Raman spectrum of a sample with the minimum resolution determined by the Abbe diffraction limit[51]:

$$d = \frac{\lambda}{2NA}, \tag{4}$$

where *d* is the minimum resolvable lateral distance between two point sources of light, *λ* is the wavelength of the light measured, and *NA* is the numerical aperture of the imaging system. The numerical aperture is a dimensionless number that relates to the refractive index of the imaging medium *n* and the maximum angle of light collection of the system θ by

$$NA = n \sin\theta. \tag{5}$$

For a microscope using an air objective, the ideal diffraction-limited lateral resolution is *λ/2*, which for typical laser wavelengths used in Raman spectroscopy of biological materials (~500-1000 nm), is ~ 250-500 nm. The spatial resolution limit can be reduced by using shorter illumination wavelengths or liquid immersion objectives with higher *n* immersion media. The axial resolution of a microscope is given by

$$d = \frac{2n\lambda}{NA^2}. \tag{6}$$

This is reduced in confocal microscopy, depending on the size of the pinhole/slit. If a spatial filter is used, the factor of 2 can be reduced to as low as a factor of 1.4. For the same wavelengths used in the example above, the axial resolution can be in the range 0.7 – 2 µm.

Optical methods that have smaller resolutions than the conventional diffraction limit are known as super-resolution microscopy. These methods use advanced scanning optics and computational analysis to spatially resolve features closer than described above. They often require specific fluorescent markers with special quenching and emission properties, enabling super-resolution by also acquiring temporal information about the fluorescent markers. These methods typically require specialised fluorescent markers to produce reliable results.

Illumination wavelength considerations

The choice of laser wavelength for Raman spectroscopy depends on multiple conflicting factors, that vary based on the form of the experiment, the form and structure of the sample, and the spectral requirements of the results. These factors are explained in greater detail in the following sections.

Raman scattering coefficient

As Raman scattering is such a weak effect, the first consideration to be made in choosing a laser wavelength is the relative strength of the Raman spectrum as a function of the laser wavelength. The scattering coefficient, μ_s, determining the probability of a photon to scatter within a material, is related to the wavelength of the photon λ by[52]

$$\mu_S \propto \frac{1}{\lambda^4}. \tag{7}$$

The strong dependence on the scattering coefficient heavily favours shorter wavelengths for Raman spectroscopy measurements. For example, a change of excitation wavelength from 785 nm to 532 nm increases the theoretical scattering rate of a sample by a factor of ~4.7. There is also a contribution in the Raman scattering coefficient depending on how close the photon energy is to a electronic transition energy of the molecule, see Chapter 3.2 for more detail.

Measurement optics and detection hardware efficiency

The optical properties of all the optics in a Raman microscope are wavelength-dependent. The reflectance efficiency of mirrors, the attenuation of glasses in lenses and the efficiency of diffraction gratings are all affected by the wavelength used. Longer wavelengths of laser will result in a wider bandwidth of Raman spectrum for the same range: a Raman shift of 1800 cm^{-1} from a 532 nm laser is 588 nm, whereas the same shift for 785 nm is 914 nm. This is more than double the bandwidth required (from 56 to 129 nm), which will require more care in compensating for chromatic aberration in the system.

The detector in a Raman spectrometer is typically a charge-coupled device (CCD) array, a semiconductor-based system which detects photons by using the energy from the photons to transfer electrons within the semiconductor. As this is a quantised method of measurement, the efficiency of the detector is described by its quantum efficiency. This is the average fraction of photons incident on the detector that are converted to charges. The quantum efficiency is dependent on the wavelength of the photon being detected, with CCDs typically being most efficient in the 400-900 nm range. For measurement of Raman spectral features above 1000 nm, InGaAs based infrared detectors are used due to their increased quantum efficiency at those wavelengths. Outside this range, CCDs are much less sensitive to light. As a result, the laser wavelength should be chosen to maximise the quantum efficiency of the detector used. For a general comparison of the efficiency ranges of different detector types, see Figure 2.

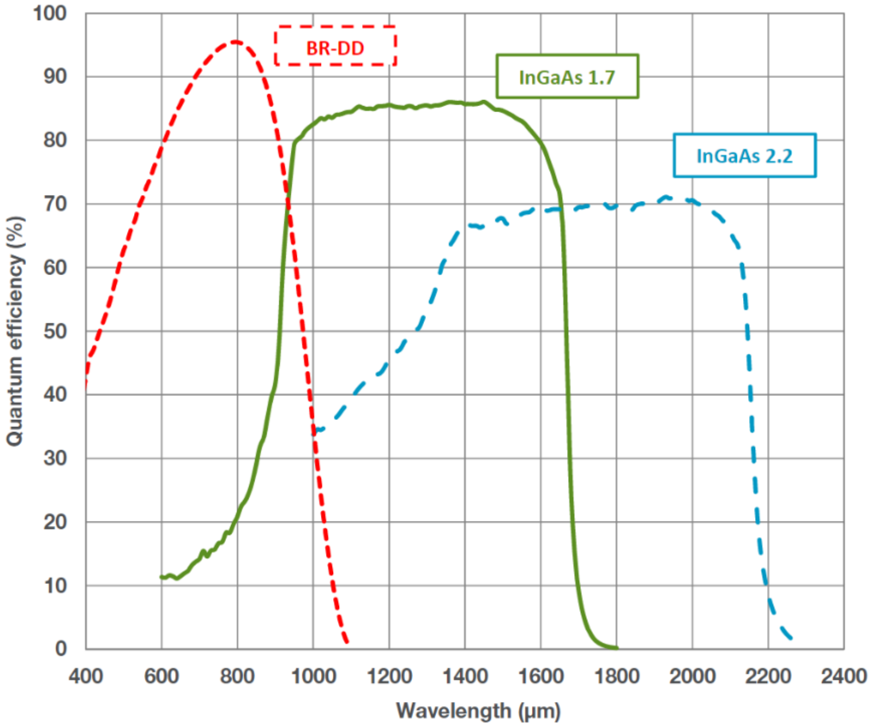

Figure 2: Quantum efficiency spectrum of different detector types sold by Andor. Here, the BR-DD curve is for an NIR-optimised CCD. From Andor.oxinst.com

Sample attenuation

For measurements of the bulk of a sample, the sample itself becomes part of the optical pathway of the microscope. Imaging of deep regions of materials using methods like confocal Raman microscopy or spatially offset Raman spectroscopy (SORS) depends on a laser wavelength that is not overly attenuated by the sample itself. For biological samples on tissue or cells, red and near-infrared (NIR) wavelengths are minimally attenuated in the ranges typically measured using Raman spectroscopy (<1 cm). For shorter wavelengths, the increased scattering coefficient may be offset by attenuation within the sample[53], especially as in epi-illumination Raman spectroscopy the effective optical path distance through the sample is double the imaging depth.

Sample autofluorescence

In tissue, the primary source of unwanted light in Raman spectroscopy is autofluorescence. While fluorescence spectra are smooth and slowly varying in shape, making them easy to visually differentiate from the much sharper peaks of Raman spectra, they increase the total amount of noise in the system due to the quantised detection of the CCD. The laser light used for Raman scattering also excites fluorescent molecules that are naturally present in tissue. Common fluorophores include elastin, collagen, lipopigments, flavins, and NADH[54]. The excitation spectra of these molecules are strongest around 300-500 nm, with emission spectra strongest in the 400-500 nm range. As a result of this, Raman spectroscopy of biological materials is typically done using a laser with a wavelength no shorter than 532 nm.

The fluorescence spectra of autofluorophores in tissue do extend higher in wavelength than these ranges, such that it is still a significant source of noise for NIR laser-based Raman systems. The main fluorophores emitting in this region are believed to be porphyrins and porphyrin degradation products. This makes the measurement of tissues with high blood content or other porphyrins, like lung, kidney, and liver, difficult due to the strong fluorescent background.

Autofluorescence can be mitigated by photobleaching, computational background subtraction, confocal Raman microscopy, or fluorophore removal prior to measurement, but it has a strong effect on the quality of the spectra acquired and as such is a key consideration in choosing a laser wavelength.

Instrumental changes that can be used to reduce autofluorescence include anti-Stokes Raman spectroscopy[55,56] and time-gated Raman spectroscopy[57–59]. Spontaneous anti-Stokes Raman spectroscopy confers a significant reduction in Raman scattering due to the lower population of molecules out of the vibrational ground state, while time-gated Raman spectroscopy exploits the longer lifetimes of excited states of fluorophores relative to those of Raman vibrational modes to suppress the measured fluorescence at the detector without suppressing the measured Raman scattering.

Benefits and limitations of Raman spectroscopy in drug detection in tissue

Spatial resolution

As the spatial resolution is of the magnitude ~ 500 nm, Raman spectroscopy is suitable for measuring the chemical composition of biological systems at several different length scales. As an optical analysis technique, the sampling volume is primarily limited by the optics of the system. The spatial resolution and therefore sampling volume can be reduced or increased depending on the application, with the sampling scale ranging from ~500 nm up to several mm. This allows for chemical mapping of tissue structures from as high is organ-level length scales to individual organelles within cells. Structures smaller than this scale like drugs, proteins and lipids, cannot be spatially resolved. They can however still be detected as part of the bulk of the sampling volume.

Sample preservation

As Raman spectroscopy interrogates the chemical composition of a sample by measuring the optical response of the sample, it is fundamentally non-destructive. High-laser power-based Raman systems may cause thermal damage to the sample, but this can be avoided by careful sample preparation, good laser wavelength choice and laser power choice. As thermal damage is likely to impose chemical changes to the sample, thermal damage can also inhibit the ability to acquire representative Raman spectra.

Non-destructive analysis techniques have several advantages over destructive techniques. They are suitable for *in vivo* studies[60,61], they can be used to perform time-series analysis on a single sample[62–64], and they leave the sample intact after measurement, enabling consecutive measurement of the same sample with other techniques if required. These factors make it more flexible in what studies are possible, and importantly reduce the amount of tissue required for studies.

Another important benefit of a non-destructive analysis technique is that of improved sensitivity. Destructive techniques, like mass spectrometry, inherently expend the sample in measuring it. In drug detection studies, this limits destructive techniques by the sensitivity to the total mass of the drug present in the sampling volume. If the drug is not detected in a measurement, it fundamentally cannot be detected with that system. In Raman spectroscopy, as the measurement is of photons from the sample and not the sample itself, more than one measurement can be made of each molecule within the sample by performing repeat measurements. These measurements can then be added together, increasing the signal-to-noise ratio (SNR) of the measurement. As a result, the theoretical detection limit of a drug within the sample is not limited by a certain concentration threshold, but by the maximum acquisition time that can be feasibly used for the given experiment. In *in vivo* studies, measurement time must generally be short, limiting the minimum drug concentrations that can be detected. In fixed or stable samples however, the detection limit is not fundamentally fixed. There are practical limitations of Raman spectroscopy that also affect the detection limit. Due to the generally shot-noise limited SNR, the detection limit is not linear with acquisition time, instead decreasing as the inverse square root of the acquisition time – this means that an order of magnitude reduction in detection limit requires an increase in acquisition time of two orders of magnitude. For a more comprehensive explanation of this relation, see section 6.

Another benefit of the repeatability of measurements is that the sampling volume is not a limiting factor in finding the minimum detectable concentration of a drug. Destructive methods reduce their sensitivity by reducing their sampling volume. This means that minimising the spatial resolution of destructive methods also impairs their detection limit. Using Raman spectroscopy, the inverse is essentially true: reducing the sampling volume is performed by increasing the NA of the system, which simultaneously increases the detection efficiency and therefore throughput of the system.

Sample preparation

Sample preparation for Raman spectroscopy is not essential. The only inherent requirement is that the region of interest in each sample is optically accessible- in biological applications this generally means that the region of interest needs to be close (<~ 1mm) to the surface of the sample, although different imaging modalities like spatially offset Raman spectroscopy have recently overcome this requirement[65].

No chemical fixation is required on tissue samples, unadulterated tissue can be measured. Due to the speed of Raman spectroscopy, there may be sample degradation during scanning that could be ameliorated using sample fixation. The lack of radioactive or fluorescent markers removes the ability for the tags used to bleach or radioactively decay, so the time between sample acquisition and Raman measurement only depends on the stability of the sample itself.

In the tissue section measurements performed in this project, the sample preparation was simply cryosectioning followed by slide mounting. The lack of required contrast medium or other sample preparation makes the Raman spectra of one sample directly comparable to that of a different sample, if prepared carefully. This contrasts with staining or spraying required by other methods that may affect the overall sensitivity of the instrument on a per-sample basis. The inter-sample comparability also facilitates quantification. While some other drug detection methods require a per-sample calibration method, Raman spectroscopic quantification can theoretically be calibrated on a per-instrument level. This reduces the amount of calibration standards needed, making the method require less unadulterated tissue to produce the calibration standards. As the calibration does not have to be performed on each sample, it also improves the throughput of the system.

Linearity

Spontaneous Raman scattering is a linear optical phenomenon, in that the number of Raman scattered photons in a specific band corresponding to a specific molecular structure is directly proportional to the number of that molecular structure within the sampling volume. This correspondingly means that, in a well calibrated Raman microscope with regular samples, the concentration of a specific molecule in the sample is linear with the Raman response of the system. This makes quantification mathematically simple, as the total Raman spectrum of a sample is a linear combination of the Raman spectra of the constituent molecules in the sample. A more detailed model of the Raman intensity of a band given a particular molecule is described in Chapter 6.2.

Sampling Rate

In biological applications, Raman spectroscopy is generally relatively slow. Tissue measurements are typically greater than 0.1 s per spectrum. Highly scattering tissue components like lipids can be detected at such speeds[66], whereas specific DNA[67] markers can take several seconds to be discriminable, in their endoginous concentration and using non-damaging laser powers. In this project, measurement times of up to 2 hours have been used to make quantitative measurements of low concentration drugs in tissue. This can make imaging very slow compared to other chemical analysis techniques like fluorescence microscopy, coherent or stimulated Raman techniques, or MSI techniques, where sampling times of milliseconds or lower are possible. There are a few ways to accelerate the acquisition times for spontaneous Raman spectroscopy. For example, if the sample is not susceptible to laser damage, the laser power can be increased.

For experiments where whole Raman spectra are required, line-scanning Raman microscopes measure the individual Raman spectra of multiple points along a 1D line in the sample illuminated by a laser focussed to a line using a cylindrical lens[68]. This instrumental geometry utilises the full scale of 2D CCD arrays, at the cost of reduced spatial resolution due to overlap between the point-spread functions of the individual points of interest in the sample when not spatially separated by enough distance. Programmable spatial filters and spatial light modulators have been used to allow for multi-point simultaneous spectral acquisition with high confocality, by using a spatial light modulator to create multiple spatially separated laser spots in the sample, and digital-micromirror devices as a programmable reflective pinhole array[69].

For experiments where only specific wavenumbers of the Raman spectrum, wide-field Raman imaging is a very fast technique for multiplexed measurement[70]. In wide-field Raman imaging, the whole imaging area is illuminated by the pump laser and collimated by an objective. This light is then passed through a filter that blocks all but the specific wavenumber of interest and is then focused onto a 2D CCD array. This produces an image of the illuminated region, with the pixel intensity corresponding to the Raman intensity of the wavenumber from the area. This method is very fast as it allows for simultaneous measurement the entire sampling area but has slightly reduced spatial resolution compared to confocal Raman spectroscopy, filter-limited spectral resolution, and only measures one wavenumber at a time. Changing the wavenumber measured requires either change of the filter used, or a tuneable filter.

Additionally, for wide-FOV scanning applications, selective sampling algorithms have been used to reduce overall measurement times. These can be done by subsampling[71], Raman sampling based on images acquired through faster means (i.e. autofluorescence)[72] and by selecting subsequent scanning points based on past Raman spectra to maximise locations of cancer in large tissue samples[73].

3.2. Resonance Raman spectroscopy

The Raman scattering rate of a photon interacting with a molecule can increase by a factor of up to 10^5 if the photon energy is close to the energy gap between electronic states of the molecule, with the increase becoming higher the closer the photon energy and electronic energy gap[74]. Practically speaking, it is the situation where the temporary ‘virtual state’ of spontaneous Raman scattering is replaced with a real electronic state.

The band gaps in biological materials tend to correspond to photon wavelengths of ~ 200 nm or lower, although it has been used to detect breast cancer tissue using 532 nm excitation.

The application of resonance Raman to biological samples is impeded by this general requirement for lower illumination wavelengths. This increases the intensity of autofluorescence as the wavelength decreases[54]. It also increases the likelihood for laser damage to the sample, which would be exacerbated in our samples by the specific tissues being measured.

The instrumental implementation of resonance Raman is also more difficult, as it benefits highly from a tunable laser if more than one Raman band is of interest. Tunable lasers tend to have wider linewidths, and have finite tuning times, making fast hyperspectral imaging difficult.

3.3. Stimulated Raman spectroscopy (SRS)

Stimulated Raman spectroscopy (SRS) is a variant of Raman spectroscopy whereby an additional light source of a specific wavelength is focussed into the same sampling volume as the pump laser as used in spontaneous Raman spectroscopy, to selectively amplify the scattering rate of a specific Raman shift by several orders of magnitude[75].

A pump laser is focussed into the sample with spatial frequency ω_p. A 'Stokes' laser of spatial frequency ω_S is focussed to the same position[76]. The interaction of these frequencies with the sample causes an amplification of the Raman scattering rate of shifts of the size $\omega_p - \omega_S$. A simple energy diagram of this process is shown in Figure 3.

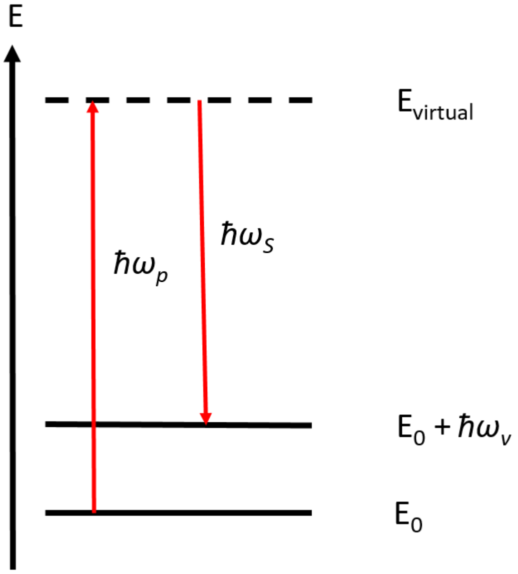

Figure 3: Energy diagram of Stimulated Raman scattering. A pump laser ω_p raises the vibrational energy state of a molecule. The Stokes laser ω_{S+} amplifies the energy state change with the same energy difference as the Stokes photon.

The pump photon acts identically as in spontaneous Raman spectroscopy, temporarily raising the vibrational state of a molecule to a virtual state. The Stokes laser is tuned to the same energy as the desired Raman shift. This state then decays to a lower vibrational state, amplified by the Stokes laser. This reduction in state energy emits a photon of the same energy, which is then detected. This increase in the Stokes frequency fluence is offset by the decrease in the Pump frequency fluence.

Practically, as the Raman scattered photon has the same wavelength as the Stokes laser, it cannot be measured separately from the Stokes laser light– the Raman scattered light manifests as a very slight increase in power at the Stokes laser wavelength. This makes standard spectrograph-based measurement impossible, and so instead lock-in amplifiers are used to measure changes in the power at the pump frequency and the Stokes frequency. The loss in the Pump intensity can be measured in the same way. To measure a range of the Raman spectrum of a sample, the Stokes laser is typically a tuneable laser that can be swept through a range of wavelengths, with a measurement recorded at each corresponding wavelength.

3.4. Coherent anti-Stokes Raman spectroscopy (CARS)

CARS is a coherent Raman scattering technique that uses three lasers to amplify the anti-Stokes Raman scattering signal of a sample by several orders of magnitude. A pump laser and Stokes laser are used in the same way as in SRS.. As the SRS process selectively raises some of the molecules in the sample to a higher vibrational energy state beyond that of spontaneous Raman spectroscopy, these higher energy molecules are raised again to a higher virtual state by the same pump laser. The transition from this state to the ground vibrational state emits an anti-Stokes photon, as shown in Figure 4. This process enables amplification of the anti-Stokes region of the Raman spectrum, which is free of standard autofluorescence. Combining this with the amplification of Raman scattering, the fluorescent background in CARS is significantly reduced. A non-resonant background at the same energy as the anti-Stokes photon is generated by the four-wave mixing of the pump photons, Stokes photons and anti-Stokes photons[77]

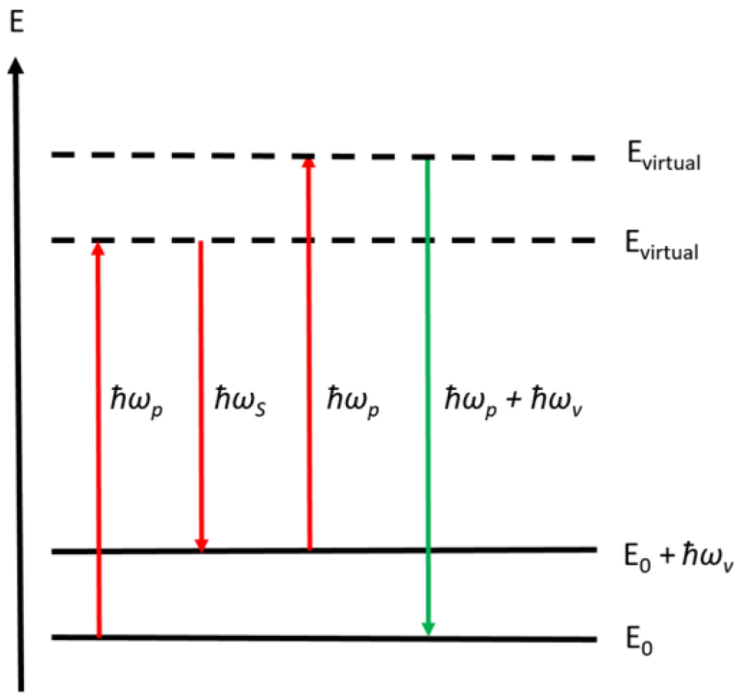

Figure 4: Energy diagram of the four steps of CARS. The molecule is brought to a high virtual state by the pump laser, and the transition to the desired vibrational state $E_0 + \hbar\omega_v$ is amplified by the Stokes laser. The state is then raised to a higher virtual state by

the same pump laser, where it emits an anti-Stokes photon and returns to the ground state..

3.5. Surface-enhanced Raman spectroscopy (SERS)

SERS is a variant of Raman spectroscopy whereby the Raman scattering rate of a molecule is amplified by several orders of magnitude due to its adsorption onto metal surfaces. This can be achieved either by deposition of the sample onto a metal (typically roughened gold or silver) surface, or by introduction of metal nanoparticles into the sample[6,78–80]. This second method can be exploited to use gold nanoparticles as molecular tags, further enhancing detection of molecules of interest[5,81].

Compared to spontaneous Raman spectroscopy and SRS, the amplification of the Raman scattering rate is dependent on the quality of the enhancing surface. While the signal enhancement is very high, it can be difficult to maintain consistently. As a result, quantification using SERS-based measurements is difficult.

3.6. Multimodal spectroscopy

As it is non-destructive, Raman spectroscopy can be combined with other methodologies to acquire further information about a sample, or to increase acquisition times

Raman spectroscopy has been combined with autofluorescence imaging in tissue for rapid tumour diagnosis[82] and with MALDI-MS to acquire greater tissue information than could be gathered by either methodology individually[83]. As MALDI is a destructive imaging technique that is typically performed on thin tissue sections, multimodal Raman-MALDI is performed on consecutive sections of tissue as opposed to the same section being measured using both devices[84,85,86].

3.7. Raman spectroscopy in drug delivery

Spontaneous Raman spectroscopy

Raman spectroscopy has been used heavily in cell-based drug delivery studies[87,88]. The diffraction-limited spatial resolution enables mapping drug uptake at an organelle level scale without labels or fixation of the cells. By scanning a laser over a tissue sample, the spatially resolved Raman spectra of the tissue can be measured and, from that, localisable chemical information about the sample can be generated.

Raman spectroscopy has been used for detecting changes in cancerous tissue due to drug application[89], detecting isotope-labelled lipid transport parasites and cells[90], isotope-labelled measurement of cancer cell metabolism for drug sensitivity measurement[91,7], and drug uptake within *E.coli* cells[92].

Confocal Raman microscopy was used to measure the penetration of caffeine into excised human skin (stratum corneum), up to a depth of 10 µm. A quantitative calibration curve was developed using HPLC as a scale. Concentrations of caffeine as low as 4 mg/g were quantified, however no lower detection limit was stated[93]. Raman spectroscopy has been used to quantify the Retinoid content in liver tissue from mice[94]. Retinoid concentrations were measured quantitatively down to 20 mM (~10 mg/g). The change in Retinoid content over time post-dose was also measured by animal sacrifice at different time frames. This paper exhibits the ability of Raman spectroscopy for quantitative measurement of dosed chemicals at biologically relevant concentrations in animals. This work was built on by measuring retinoic acid uptake in liver cells in vitro[95]. Cells were incubated in 50ug/mL solution of poly(methyl methacrylate) (PMMA) nanoparticles for 1-3h, upon which qualitative mapping was performed.

This previous work has already shown the capability of Raman spectroscopy in quantitative detection of drugs in tissue. However, they operated at relatively high concentrations (> 1000 µg/g)[96]. This was suitable for the specific applications (measurement close to topical application of a drug, and natural chemical accumulation in the liver), but in general drug delivery many therapeutic doses of drugs are applied at much lower (<100 µg/g) concentrations[97]. Accumulation of drugs in specific organs or regions of organs leads to higher peak concentrations that may then be detectable, at the cost of lost sensitivity elsewhere (for more information about drug delivery in general, see section 2.1. For this purpose, this project has focussed on determining the minimum quantifiable concentrations of different drugs within tissue analogues in reasonable time scales (~hrs).

SRS and CARS

While spontaneous Raman and SRS produces a linear response in Raman intensity versus the concentration of the relevant molecule in the sample, making quantification mathematically simple, CARS exhibits a quadratic response, which combined with the nonlinear background features in its spectra, makes quantification difficult. +Spectral decomposition methods have demonstrated the ability to separate the signal from the chemical of interest from the rest of the measured signal[98].In the context of drug delivery, CARS has been used to qualitatively map deuterated nanoparticles in brain[99], liver and intestine of mice that had been dosed orally (200uL of 75mg/mL) and intravenously (200uL of 10.4mg/mL) [100]. SRS has been used to image drug delivery in skin[101,102], measure isotopically-labelled glucose for metabolism imaging[103], and measure transport of alkyne-tagged molecules in cells[67].

4. Instrumentation, materials and methods

4.1. Experimental requirements of the Raman spectrometer

The aim of this thesis was the investigation of Raman spectroscopy as a tool for detecting the presence of a dosed drug in tissue. This involves the measurement of trace compounds within samples that have relatively much stronger Raman signal, as well as much stronger background. These factors, along with the physical geometry of the samples used, meant that the design of the Raman measurement had very strict specification requirements. For this reason, two bespoke Raman microscopes were built for this thesis. As the parameters of the samples dictated the parameters of the instruments used, the samples are described in this section prior to the subsequent design, construction and characterisation of the resulting Raman microscopes.

Tissue

Measurement of any tissue using Raman spectroscopy is affected by several practical limitations. These include the relatively low scattering rates of tissue leading to weak Raman scattering, susceptibility to laser damage limiting the throughput of spectral acquisition using Raman spectroscopy, degradation of unfixed tissue during long Raman scanning measurements, and high noise contributions to the Raman spectra from the autofluorescence that is prevalent in tissue. These factors are all present in most tissue measurements using Raman spectroscopy and so must be considered when designing a Raman instrument.

The following are the design requirements that are present for almost all tissue measurements, not only for the specific requirements of our experiments.

Spatial resolution

As one of the primary benefits of optical imaging over other methodologies described in the first chapter, the spatial resolution of Raman spectroscopy can enable subcellular analysis of tissue. For this to be possible, the Raman spectrometer had to be configured as a microscope, where the laser is focussed into the sample and the Raman scattered light is collected and collimated, using a microscope objective. To resolve different organelles, a spatial resolution of ~ 1 µm was required. The spatial resolution of a Raman microscope is limited by the spot size of the laser and the NA of the collecting objective lens. Using a collimated laser that fully back-fills the objective, and using the system in an epi-illumination arrangement, results in the spatial resolution being limited primarily by the objective. Additional factors like scattering within the sample material and aberrations in the rest of the microscope were mitigated. Sample scattering was mitigated by using thin samples (<20 µm) and a confocal system. Optical aberrations in the microscope were mitigated by exclusively measuring in the optical axis, and using optics with chromatic aberration correction in the wavelength range of interest.

Spectral resolution

Different tissue types and different structures within tissue exhibit different Raman features. To discriminate these, the instrument required a sufficiently high spectral resolution. Increased spectral resolution increases the shot noise in the system, as the spectrum is binned into smaller bandwidths. Using twice as many bins with half the individual bin width results in twice as many measurements being taken for the same total amount of light. This would result in a √2 increase in the shot noise, if the bins are then numerically added together. The spectral sampling rate of the CCD detector had to be balanced with the spectral resolution of the rest of the instrument, to avoid under or oversampling.

The requirements of the spectral resolution also meant that the laser source itself required a very small bandwidth, as a large wavelength laser source fundamentally limits the spectral resolution of the detected spectra.

Laser damage

Tissue itself is susceptible to thermal damage from the laser used in Raman spectroscopy. To avoid this damage, the laser power density in the sampling volume must be below the threshold where detectable spectral change occurs in the timeframe of the experiment. For a two-hour series of 10-second measurements of a single point in a sample, the only significant difference between any of the individual measurements should be the reduction in the autofluorescent background due to inherent photobleaching during the experiment.

Raman detection efficiency

As the laser power limitation puts a maximum throughput rate on the Raman detection, it was imperative that the detection pathway efficiency of the microscopes was as high as possible. To achieve this, only the necessary optics could be present in the detection pathway, using the most efficient optics available.

Spectral acquisition rate

The required acquisition rate depended on the experiment and were a balance between acquisition speed and spectral quality in the form of SNR. For basic tissue discrimination, spectral acquisition rates of ~1 Hz were possible, which enabled imaging in reasonable timeframes. For single point analysis, much longer acquisition times could be used.

Laser wavelength

The wavelength of the laser used affects the background strength, Raman signal strength, Raman signal detection efficiency, spatial resolution and potential damage to the tissue. These factors potentially differed between tissues, so there was no certain ‘ideal’ laser wavelength for all tissue measurements. To this end, wavelengths below ~500 nm could not be used for autofluorescence and damage reasons. Wavelengths above ~800 nm could not be used with the detection methods we had available, and also significantly hamper the strength of the Raman spectra that could be acquired. To determine the ideal wavelength, we built two Raman microscopes, one using a 671 nm laser, and one using a 785 nm laser. These were both in the range that most tissue Raman measurements are performed in but were sufficiently different to potentially compare the relative benefits of each.

Thin tissue sections

Part of the work for this thesis involved considering the combination of Raman spectroscopy with MALDI-MSI for multimodal imaging purposes. For multimodal imaging using different instruments in physically different locations, it is much more practical to be able to use duplicate samples that are individually measured in the different instruments than consecutive measurement of a single sample in all of the different instruments. This is due to the potential of sample degradation during measurement and transport, and as certain imaging methods require non-compatible mounting media or preparation. For example, the ITO-coated glass slides used in the MALDI measurements were not suitable for Raman measurement, and re-mounting of thin tissue sections used in MALDI was not feasible. As the tissue was being sectioned thinly (~16 µm) for the MALDI measurements, using adjacent sections for Raman measurements was chosen to maximise inter-sample regularity. Any tissue structure larger than the combined thicknesses of the samples were unlikely to materially differ between adjacent sections of this size. The limitations of using different tissue sections were that A) any features at close to or smaller than the section thicknesses would not be directly registerable or comparable between sections, and B) that tissue sectioning and subsequent mounting caused some physical warping of the sections. These factors meant that small physical features could not be directly compared between the sections, as they physically weren’t present in the same locations, and the warping meant direct registration was impossible- only feature-based comparison could be used. In practice, we never reached the stage of direct multimodal tissue imaging, so it didn’t become an issue in our studies. Separate Raman mapping of tissue was performed on unique tissue samples, and multimodal comparison between point-based Raman and MALDI imaging on adjacent sections of tissue models was performed. Further multimodal imaging of tissue would require complex registration or significant spatial resolution limiting.

Additionally, previous work has shown the use of thin tissue sections as a means of minimising autofluorescence within measurements by physically removing out-of-focus fluorophores that contribute heavily to the background of spectra while simultaneously being minimally bleached by the laser[104,105].

For the purpose of Raman microscope design, this sample geometry introduced additional instrumental requirements.

Depth of focus

The instruments had to be capable of efficiently measuring Raman spectra from tissue sections of thickness ~10-20 µm. This required a depth of focus similar in scale to maximise the sampling volume of the system without losing axial resolution, which required a matched NA objective (NA of ~ 1.2) paired with a high-quality laser source. A depth of focus larger than the thickness of the sample would result in loss in axial resolution, whereas a depth of focus smaller would necessitate higher laser power density to the volume of the tissue being measured, unnecessarily risking thermal damage to the sample.

Focal stability

As the samples were of the scale of rat organs in width (~1 cm), but only 10-20 µm in thickness, the microscopes needed to be capable of retaining focus in very high width : thickness ratio samples.

4.2. Drug detection in tissue

Beyond the efficient measurement of thin tissue sections, our project in the evaluation of Raman spectroscopy for low concentration (1-500 µg/g) drug detection in those sections imposed further requirements of the microscopes.

Increased acquisition times

Further to the extended detection times required for tissue measurement, the times were much longer for drug detection. The required SNR for drug detection almost always required summation of multiple consecutive spectra acquired at each position in the tissue. This was because the fluorescent background never fully attenuated, so single acquisitions with an integration time of longer than ~ 10 s would be prone to saturation of the CCD detectors used. This meant that the CCDs used had to have both a large well depth and low readout noise, as repeated measurements would cause repeated addition of readout noise. If this were too high, the SNR would not appreciably increase when adding repeated spectra together.

Spectral range

The drugs used in this work all contained bonds that exhibit Raman peaks in the silent region. These peaks are theoretically easier to detect than drug peaks in the fingerprint region or high wavenumber region due to the reduced background from the tissue Raman signal, and the reduced variation in the background due to heterogeneity in the tissue. In the silent region, only autofluorescence contributes noise from the tissue, and the autofluorescent spectral shape is much more consistent between different regions of a tissue than the Raman spectra. As a result, the silent region is both lower in noise and less variable than the other two spectral regions. Additionally, as the background is essentially flat, the Raman peaks from the drugs generally exhibit as the same shape as they do from pure samples- this means that background subtraction is simpler, and that identification of the drug peaks does not require high spectral resolution. This was to the benefit of our work, as it meant that a lower density grating can be used to increase the spectral range of the measurements, enabling simultaneous measurement of the fingerprint region and silent region. The fingerprint region allowed analysis of the structure of the tissue while the silent region could be used in tandem to detect and quantify the drug.

Noise minimisation

Due to the very low concentrations of drug measured, the expected strength of the Raman peaks from the drugs were very low. This very low predicted signal necessitated both very long integration times and all possible reductions of noise. To reduce the noise, the tissue was exposed to the laser of the microscope prior to Raman measurement to photobleach the fluorophores naturally present in the tissue. Autofluorescence contributions to the noise were the only tissue sources of noise that could be practically removed from the Raman spectra. While heterogeneity in the tissue causing variation in the Raman spectral contributions could be considered noise in a drug detection experiment, it is a property that cannot be removed from the tissue without homogenising the tissue. For the quantitative drug detection study, we did homogenise the tissue to produce a calibration standard-level of accuracy. For real tissue measurements, tissue heterogeneity must be considered when attempting to detect drug presence. Again, we avoided this problem by simply using the silent region. In the silent region, variation in the drug signal measured should only be due to heterogeneous drug distribution irrespective of tissue heterogeneity.

4.3. 785 nm Raman microscope

Design considerations and relative benefits

785 nm is one of the most commonly used laser wavelengths for Raman spectroscopy of biological materials, due to it being a compromise between the high autofluorescence from shorter wavelengths and the reduced Raman scattering rate from longer wavelengths. A higher wavelength than 785 nm would also significantly compromise the quantum efficiency of the detectors commonly used, especially in the Raman-silent region which is detected at a longer wavelength than the fingerprint region. Fewer naturally occurring fluorophores absorb 785 nm, and with less intensity, than for shorter wavelengths. Additionally, tissue is less absorbent of NIR light than visible light, reducing the attenuation of the signal within the sample (which is not a real concern for our thin

tissue sections), and minimising the heating rate of the sample. 785 nm is also a convenient wavelength for designing optics, with several laser source types at different powers and common availability of filters for the wavelength available.

Construction

I constructed a Raman microscope consisting of three optical pathways, separated by a dichroic beam splitter: The laser source, the sample stage, and the spectrometer. For a complete schematic of the optical pathway of the microscope, see Figure 5. The laser source is the pathway that provides the laser light for Raman spectroscopy and contains the optics necessary for creating a collimated beam of the appropriate specifications for the rest of the microscope. The sample stage is the pathway that contains the sample itself, the objective lens, the microscope body, and the brightfield-imaging optics. The spectrograph pathway is the pathway that separates the Raman scattered light from the laser light and analyses it.

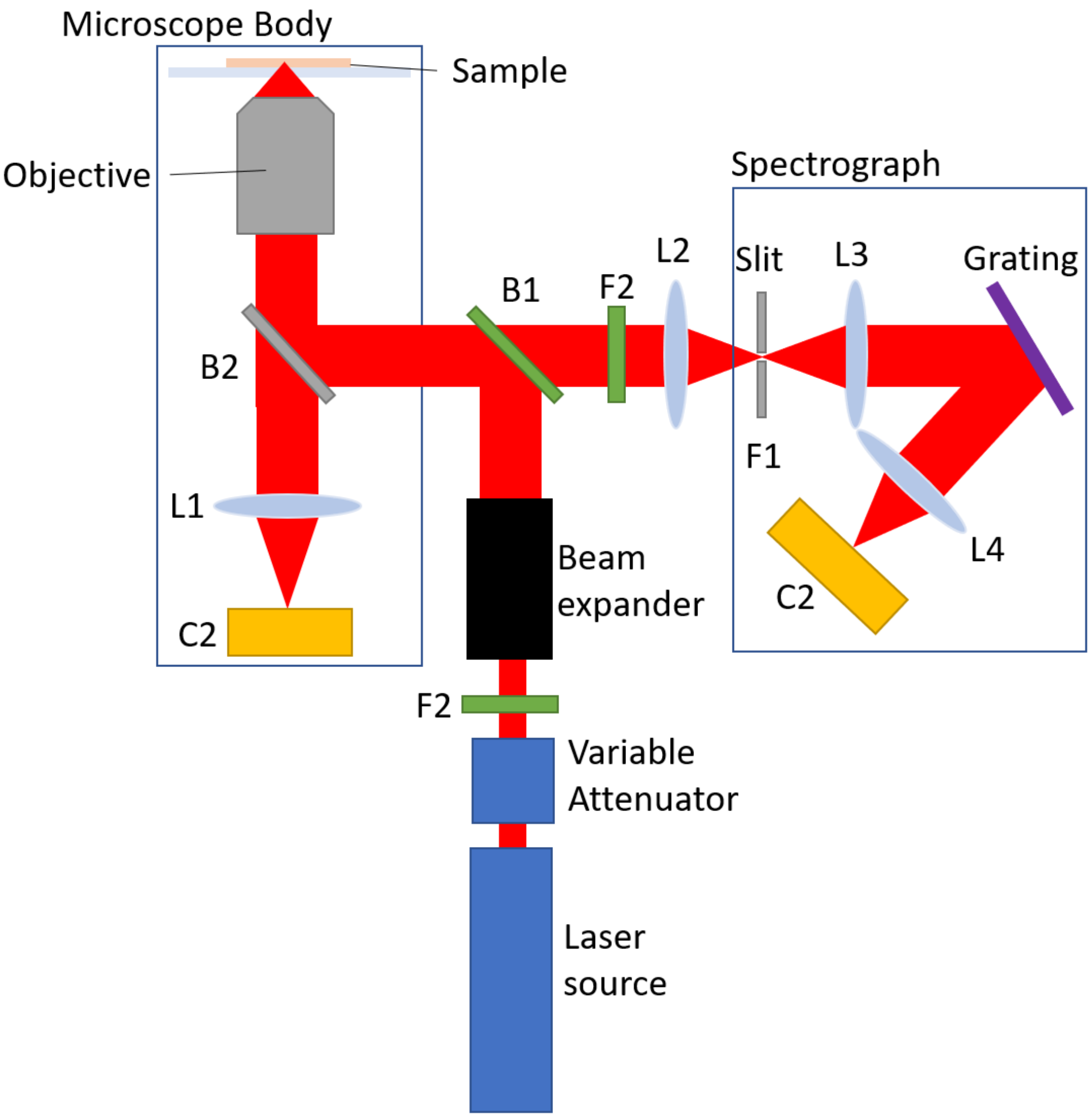

Figure 5: Optical schematic for the 785 nm Raman microscope. F: 785 nm Laser clean-up filter; B1: 800 nm cut-off dichroic beam splitter; B2: Beam splitter/mirror/none (switchable depending on imaging mode); L1: Microscope Tube lens; C1: Microscope camera; F2: 800 nm long pass filter; L2: 60 mm lens; L3 & L4: focussing optics in spectrograph; C2: CCD detector. Alignment mirrors and optical isolator are excluded to simplify the diagram.

Laser source pathway

The laser used in the microscope is a 3.3W continuous wave (CW) 785 nm Ti:Sapphire laser (3900s, Spectra-Physics) tuned to 785nm, pumped by a 10W CW 1064 nm Nd:YAG laser frequency-doubled to 532 nm (Millenia Pro, Spectra-Physics). The pump laser power is variable and is coupled to a polariser-waveplate-based variable attenuator to allow low laser powers (< 250 mW) without stopping lasing. A 785 nm laser line filter (Semrock) is used to minimise the laser linewidth beyond the wavelength selection optics already present in the Ti:Sapphire laser.

A 1-8x variable beam expander (Edmund Optics) is used to expand the beam diameter from 2 mm to ~8 mm. This was done to optimise the depth of focus of the microscope and will be explained along with the description of the objective lens.

The laser beam is then reflected from the 800 nm dichroic beam splitter (Semrock), into the back port of the microscope body itself.

Sample stage pathway

This is the part of the microscope that is physically inside the microscope body, a Nikon Eclipse Ti-U inverted microscope. Functionally, it is used to manipulate the sample, and the laser spot itself, along with allowing for laser spot analysis and bright-field imaging using the side camera port.

The laser beam is fed into the back port of the microscope, where it meets with the filter wheel. For Raman spectroscopy, the filter wheel contains a mirror to allow the laser to pass uninhibited to and from the objective. For laser spot imaging, a 10/90 reflective beam splitter is used to send some of the back-reflected laser from the sample to the monochrome microscope camera (Thorlabs), and for bright-field imaging, the filter wheel is empty. In bright-field imaging, the light is provided by an overhead bright light source and condenser unit, so the laser and spectrometer pathways can be blocked off. A monochrome camera is used as the sensitivity to 785 nm light must be high for laser spot analysis.

With no filter in the wheel in position, the system is ready for Raman spectroscopy. Here, the laser beam is directed into the back aperture of the objective lens. The objective used is a 1.2 NA 63x quartz-immersion fluid corrected, infinity corrected objective (RiverD). This objective was designed for on-axis Raman spectroscopy in the NIR range, and as such is ideal for the application. It is corrected for use with quartz-matching immersion fluid (*n* = 1.45), with a working distance of 1.2 mm. This allows us to use quartz microscope slides, which are necessary for Raman spectroscopy due to the high background found in regular glass slides. Without additional lens elements for correcting off-axis aberrations (coma, astigmatism, field curvature), the objective itself has a minimum amount of glass, minimising the optical attenuation of the objective. The beam diameter of the laser determines the effective laser spot size of the system, as the spot size is limited by the numerical aperture of the objective. If the beam does not fill the back aperture of the objective, the effective NA is reduced, resulting in an increased spot size. The back aperture of the objective is 10 mm, but we expanded the beam to 8 mm. This was because we wanted the depth of focus, or essentially the length of the laser spot, to be slightly smaller than the thickness of the tissue sections we were using (~16 µm). With a diffraction-limited spot, the depth of focus was slightly too small. For the resulting depth of focus, see the instrument characterisation section below.

The laser light is focussed using the objective, passing through the quartz-matching immersion fluid (Cargille) and the 1 mm thick quartz slides (UQG Optics), to a laser spot centred in the thickness of the sample. The samples were mounted onto thick slides to reduce the risk of breakage during transit. No coverslips were used to minimise the intensity of in-focus signal from the substrate. Back-scattered light, both Raman and Rayleigh, and autofluorescent light are then collected and collimated by the same objective and directed back towards the dichroic beam splitter. As the Raman-scattered and fluorescent light is mostly longer than the cut-off wavelength of the dichroic, it passes through towards the spectrometer.

The sample itself is mounted in a temperature control block, which is described later. The temperature control block is mounted on a 3-axis (x,y,z) motorised stage (Prior Scientific), which is how both the Raman scanning and autofocus system (described later) are operated.

Spectrometer pathway

The Raman-scattered and fluorescent light from the sample pass through the dichroic beam splitter towards the spectrometer. It first passes through an 800 nm long-pass filter to block any laser light that passed through the dichroic. This is necessary as the Raman scattered light is many orders of magnitude weaker than the backscattered laser light, so the airy disc of the laser line on the CCD can overlap and affect the Raman lines that are desired. To stop this, as much laser line light must be blocked from the spectrometer.

After the filter, the light is focussed through a mechanical slit of width 20 µm using a 60 mm lens. The slit blocks out-of-focus light in one dimension from entering the spectrometer, making the system confocal. The other dimension of out-of-focus light is blocked by the CCD itself, explained below.

Through the slit, the light is re-collimated within the spectrograph itself. The spectrograph (Acton LS 785, Princeton Instruments) consists of a lens group that collimates the light onto a reflective grating (1200 mm^{-1}), and another lens group that focusses the light diffracted by the grating onto the CCD detector. The grating disperses the light, imparting a varying diffraction angle depending on the wavelength of the light. This dispersed light is focussed by the lens group, where the diffraction angle determines the axial offset of the light in the focal plane. This means that the light is spatially separated by wavelength in the plane of the CCD, where it is detected.

The CCD used is a 1024x127 thermoelectrically cooled CCD array (iDus 401, Andor). The CCD is aligned on the spectrograph such that the long axis is parallel to the diffracting plane of the grating, and perpendicular to the slit. This arrangement allows for the long axis to be the axis along which the light is dispersed, and also spatially filtered by the slit. The light is spatially filtered perpendicular to the grating by choosing the number of rows of pixels that are actually measured during an acquisition. As the CCD pixels are 26 µm, the effective pinhole size can be any multiple of 26 µm vertically, and a continuous value controlled by the mechanical slit horizontally.

In practice, the use of thin tissue sections along with the objective lens used meant that the out of focus light was from either the slide, or the air above the sample. Both of these are very weak sources of light, so the confocality of the system was not essential.

A programmatically controlled mechanical shutter blocked light from entering the spectrograph and hitting the CCD outside of a measurement, and during CCD readout.

Instrument characterisation

To verify the instrument was operating with the desired specification, validation experiments were performed.

Spatial resolution

The spatial resolution of the instrument determines the smallest features that can be resolved. It is theoretically equal in both lateral (perpendicular to optical axis) dimensions but is larger in the axial dimension.

Lateral resolution

The lateral resolution was determined by scanning a Raman map of polystyrene beads. These have consistent sizes and a strong Raman signal. As spheres, they act as physically extensive sources of light in Raman measurements when there is overlap with the laser spot and the bead. A Raman map of a polystyrene bead is shown in Figure 6.

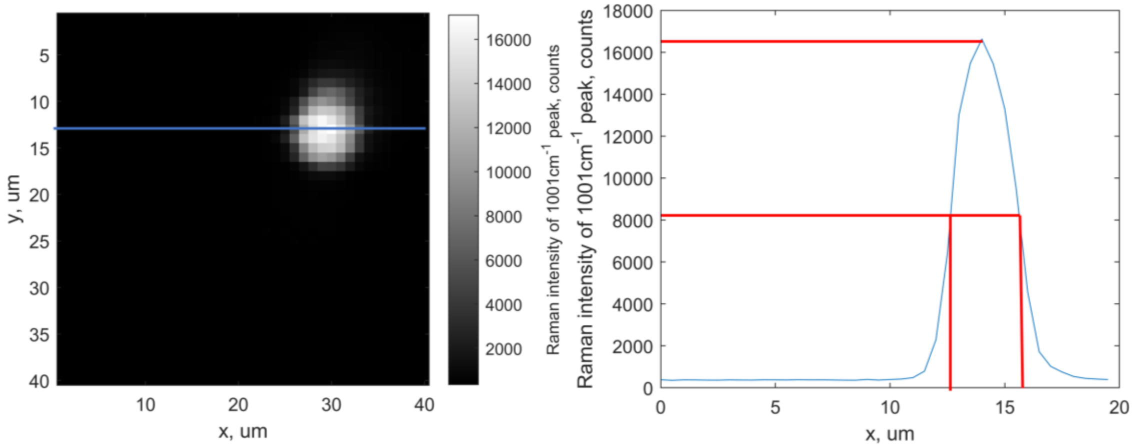

Figure 6: Left: Raman map of 3 µm diameter polystyrene bead, signal under 1001 cm^{-1} peak from 0.5 s 200mW exposure. 500 nm step size. Right: Intensity plot of single line of map, denoted on the map with a blue line. The red lines demonstrate how the FWHM was measured. The FWHM of the plot is 3.7 µm.

The lateral resolution was determined by calculating the full width half maximum (FWHM) of an intensity plot of a single scan line through the centre of a polystyrene bead. The difference between this value and the physical diameter of the bead was used to characterise the lateral resolution. This value was calculated to be 0.7 µm.

Axial resolution

The axial resolution of the instrument was determined by calculating the axial FWHM of the laser spot. To do this, quartz-matching fluid was dropped onto the top of the slide. The interface between the quartz slide and the matching fluid has no change in refractive index but does have a change in the Raman spectrum measured. When focus is moved across this interface, the measured Raman spectrum changes from that of pure quartz to that of pure immersion fluid. The FWHM of the gradient of the strength of the immersion fluid peaks was used as the definition of the axial resolution. This result is graphically shown in Figure 7. The FWHM of the laser spot was calculated to be 13 µm, which allowed for measurement of almost the entire depth of the 16 µm tissue sections with a small amount of extra tissue to account for possible focal drift during measurement. A slit width of 20 µm was used as a compromise between fluorescence reaching the CCD and the spectral resolution of the system.

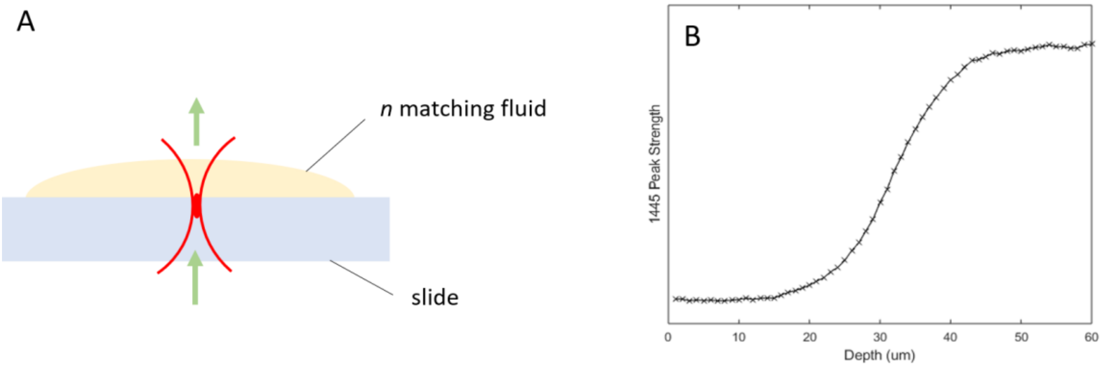

Figure 7: Axial resolution evaluation method. A: Diagram showing how the laser spot is stepped up from the bulk of the slide, through the slide/fluid interface, into the bulk of the fluid. In red: laser beam profile and laser spot shape. In green: laser traversal direction. Not to scale. B: Raman strength of 1445cm^{-1} peak from matching fluid spectrum as function of laser spot position.

Spectral resolution

Spectral calibration of the Raman spectrometers was done by measuring the spectrum of a sample with known peak wavenumbers and producing a calibration curve by fitting the pixel numbers of the spectral peaks to the known wavenumbers measured by FT-Raman (McCreery group), an interferometer-based Raman spectrometry method that is capable of measuring spectra with absolute wavelength. The Raman spectrum of polystyrene and the Raman spectrum of acetaminophen were measured using the instrument. The wavenumber pixel assignment curve was generated by fitting the location of the polystyrene peaks on the CCD to the reference wavenumber values. The accuracy of this calibration was determined by then comparing the wavenumbers of the peaks from the acetaminophen spectrum to the wavenumbers of the reference source. The results of this are shown in Figure 8.

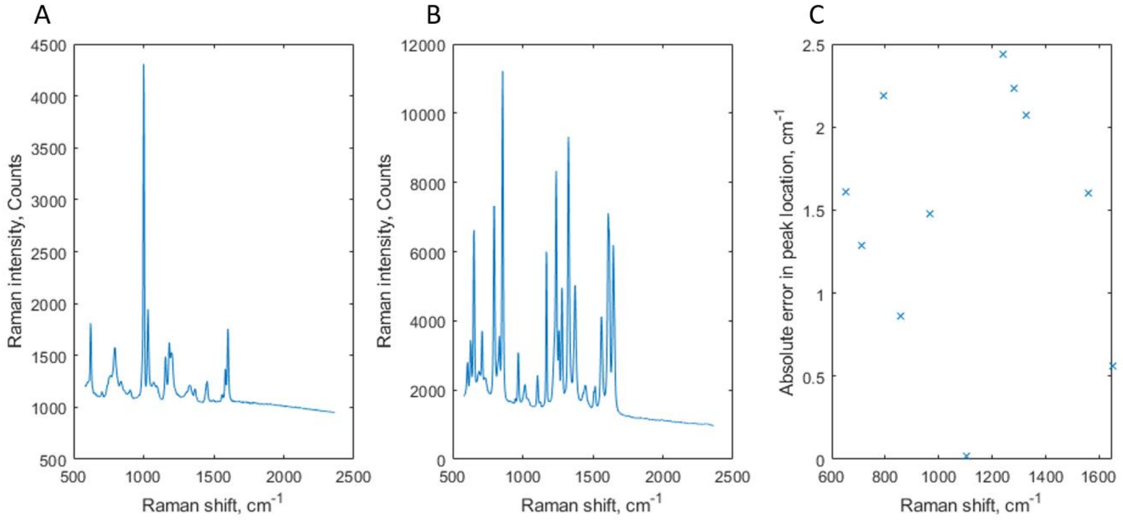

Figure 8: Spectral calibration assessment for 785 nm Raman microscope. A) Raman spectrum of polystyrene. B) Raman spectrum of acetaminophen. C) Absolute error between acetaminophen peak locations from calibration and standard reference.

The absolute difference between the calibration assignments and the true wavenumber values was never more than 2 cm^{-1}. The standard deviation of the errors was 1.73 cm^{-1}. Some of the error was due to the discrete nature of the CCD pixels – each pixel bin was approximately 2 cm^{-1} wide depending on the location in the spectrum. Otherwise, the finite spatial resolution of the system and finite pinhole size also affects the width of the Raman peaks.

4.4. 671 nm Raman microscope

Design considerations and relative benefits

For the silent-region tagged molecules we were interested in detecting within tissue, there were several benefits to 671 nm over 785 nm that led to it being considered worth examining. The samples we used were of the same order of thickness as the depth of focus of the laser, meaning that the entire thickness of the sample was being photobleached equally. The low thickness also limited the amount of energy absorbed by the sample, allowing for higher laser powers without sample heating and consequent thermal damage. This meant that the resultant samples exhibited autofluorescence that bleached quickly relative to in bulk tissue. When combined with the long integration times needed to detect the drugs, the initial autofluorescence was considerably reduced. There were two main benefits to 671 nm illumination over 785 nm for our experiments. The first is the increased Raman scattering rate – the scattering rate for 671 nm is ~ 1.9x higher than it is for 785 nm, due to the $1/\lambda^4$ dependancy. The second is the increased quantum efficiency of the detector in the Raman-silent region. At 2220 cm^{-1} (the general location of the alkyne-peaks in the silent region), the quantum efficiency of a 671 nm-based microscope using our detectors is approximately 93%. For a 785 nm-based microscope, the efficiency is approximately 55%. These two factors alone confer a ~ 3.2x increase in Raman spectral throughput for the same laser power in otherwise identical microscopes in the silent region. For drug detection experiments, the Signal-to-noise ratio of the system is the key parameter, which necessitates a balance between the Raman intensity and the intensity of the noise contributions from the sample.

Construction

The overall design of the 671 nm Raman microscope is qualitatively the same as that of the 785 nm microscope, in that it is a confocal epi-illumination Raman microscope. A diagram of the optical pathway is shown in Figure 9.

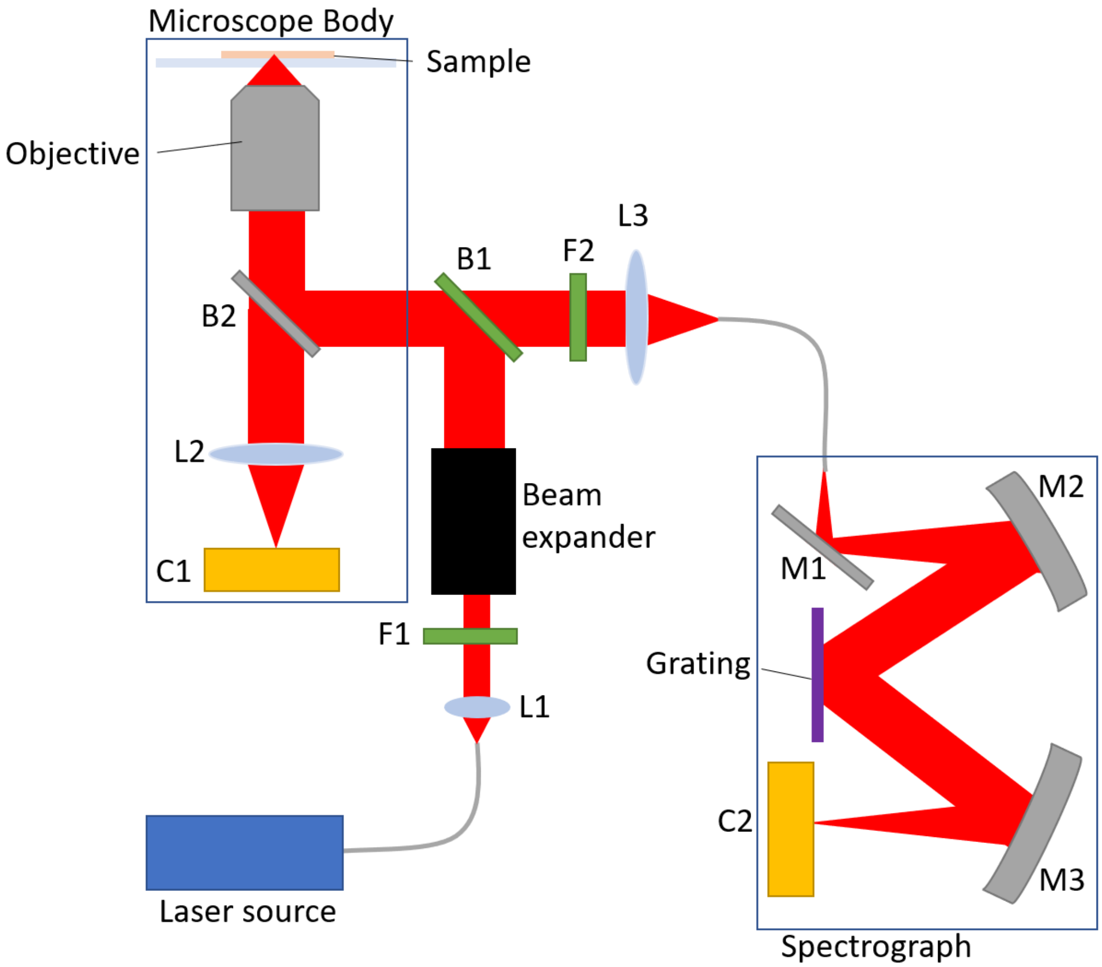

Figure 9: Optical schematic for 671 nm Raman microscope. L1: Laser collimating lens; F1: Laser line filter; B1: Dichroic beam splitter; B2: Microscope filter wheel (Mirror, semi-reflecting beam splitter, or empty); L2: Microscope tube lens; C1: Microscope camera; F2: Long pass filter; L3: Fibre input lens; M1: Spectrograph mirror; M2 & M3: concave mirrors; C2: CCD detector. Alignment mirrors excluded to simplify diagram.

The laser light is sourced from a 150 mW 671 nm CW laser (Gem 671, Laser Quantum), fed to the microscope using an optical fibre and collimated using a 2 mm aspheric collimating lens (Thorlabs). The collimated laser beam then passes through a 671 nm laser line filter (Semrock) to minimise the linewidth. A beam expander is used to make the beam diameter approximately 8 mm, for the same reasons explained in the 785 nm microscope. A 700 nm dichroic beam splitter reflects the laser light into the back port of a Nikon Eclipse Ti-U inverted microscope. The filter wheel can be rotated between a mirror for Raman spectroscopy, semi-reflective beam splitter for laser spot imaging, or empty for brightfield imaging, as in the 785 nm microscope. The microscope camera used is a colour camera (Infinity). The microscope objective lens used is the same as used in the 785 nm microscope, a 1.2NA 63x oil immersion objective (RiverD). This objective was used due to it being optimised for the quartz slides used, and the other factors that are functionally the same as in the 785 nm microscope. The sample is mounted on a motorised stage (Prior Scientific), which is moved to scan the laser spot through the sample during Raman imaging.

Back-scattered light is collimated using the same objective, and Raman scattered light passes through the dichroic beam splitter and long-pass filter (Thorlabs). This light is then focussed into an optical fibre using a 20 mm fibre coupling lens mounted on a x-y stage. The fibre is a 50 µm optical fibre (Ocean Optics), and acts as a 50 µm pinhole, replacing the slit used in the other system. The opposite end of the fibre is mounted to the input port of the spectrograph (Shamrock 303i, Andor), which functionally operates the same as the Acton LS785 in the other system, only using reflective focussing optics as opposed to refractive optics, and with a motorised grating turret, allowing for easy swapping and adjustment of the grating. This spectrometer was also used due to instrumentation access limitations in the lab. The grating primarily used was a 600 mm^{-1} grating, allowing a spectral range of ~ 800 – 2600 cm^{-1}. The diffracted light is then re-focussed onto the detector, a back-illuminated, deep depletion thermoelectrically cooled 1024x255 CCD (Newton 920 Br-DD, Andor). The detector was maintained at -70 °C during measurements to minimise the dark current.

Instrument characterisation

The optical characteristics were validated in the same way is in the 785 nm instrument.

Lateral resolution

A 3 µm polystyrene bead was scanned with a 0.5 µm step size. The integration time was 0.5 s, and the laser power was set to 30 mW. The lateral resolution was calculated by the increase in extent of the 1001 cm^{-1} peak image relative to the known size of the bead. The map is shown in Figure 10.

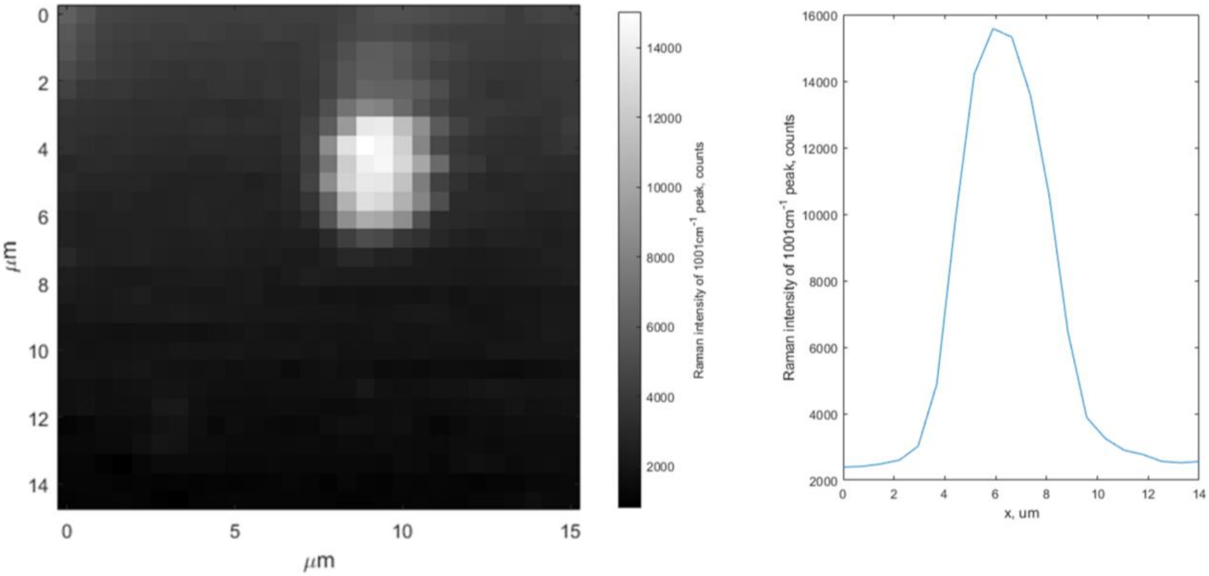

Figure 10: Left: Raman map of 3 µm diameter polystyrene bead, signal under 1001 cm^{-1} peak from 0.5 s 200mW exposure. 500 nm step size. Right: Intensity plot of single line of map.

The effective lateral resolution of the 671 nm microscope was 1.5 µm.

Axial resolution

As with the 785 nm system, the axial resolution was defined as the FWHM of the gradient of the immersion oil 1450 cm^{-1} peak as a function of the depth through the slide/immersion oil interface. The result is shown in Figure 11.

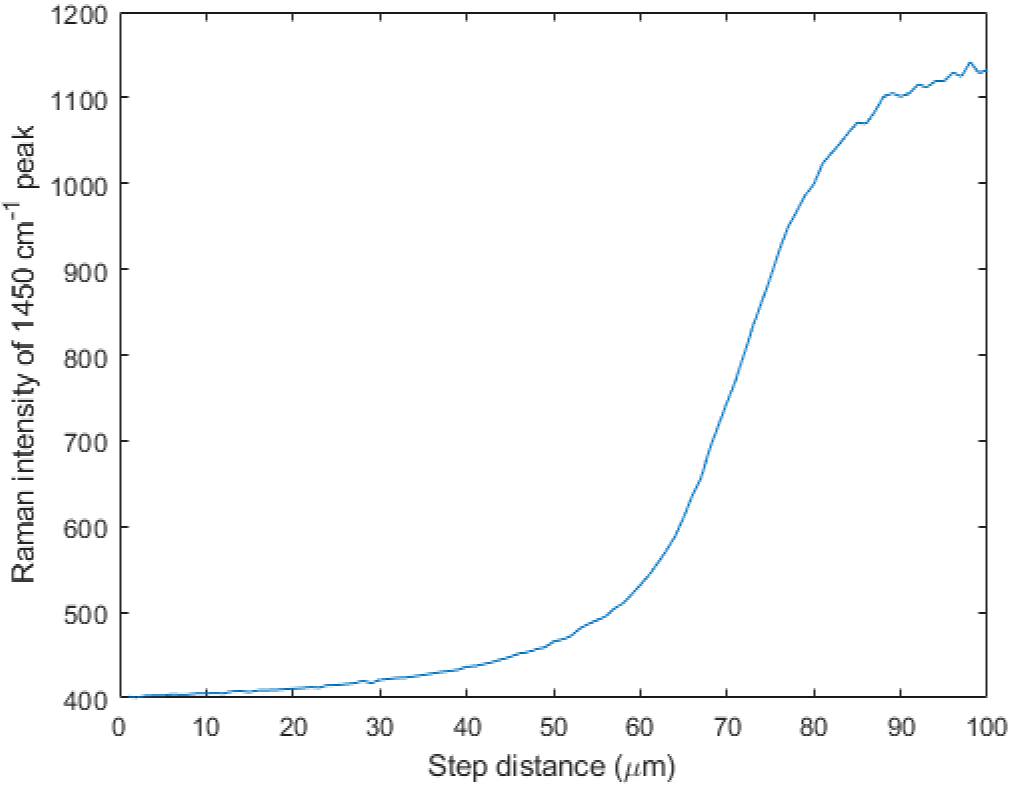

Figure 11: Raman strength of 1445cm^{-1} peak from matching fluid spectrum as function of axial laser spot position.

The FWHM of the gradient was 14 µm. In measurements of bulk samples, like the immersion fluid on the slide here, the relatively large effective pinhole of the optical fibre resulted in an increased depth of focus due to the increased presence of out-of-focus material. This was likely the reason for the longer depth of focus relative to the 785 nm system. As discussed previously, the confocality of the system is not a primary concern when we are measuring the full depth of very thin samples.

Spectral resolution

In the same way as was done for the 785 nm instrument, the spectral resolution of the 671 nm instrument was calculated by comparing the difference between the wavenumbers of the peaks of a Raman spectrum as sourced from reference literature and the wavenumbers from the calibrated spectrum.

The Raman spectra of polystyrene and acetaminophen were measured. The locations of peaks of the polystyrene spectrum were used to create a wavenumber-pixel calibration. This calibration was used to measure the wavenumber locations of the acetaminophen peaks. The difference between the two sets of acetaminophen peak locations was used to evaluate the spectral resolution, as shown in Figure 12.

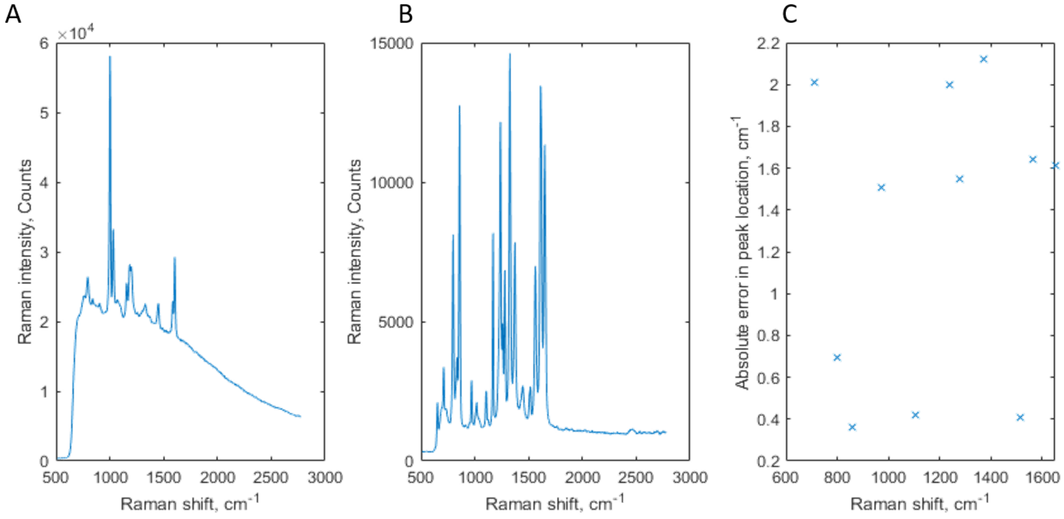

Figure 12: Spectral calibration assessment for 671 nm Raman microscope. A) Raman spectrum of polystyrene. B) Raman spectrum of acetaminophen. C) Absolute error between acetaminophen peak locations from calibration and standard reference.

The absolute difference between the calibration assignments and the true wavenumber values was never more than 2.2 cm^{-1}. The standard deviation of the errors was 1.28 cm^{-1}. Some of the error was due to the discrete nature of the CCD pixels – each pixel bin was approximately 2.2 cm^{-1} wide depending on the location in the spectrum. Otherwise, the finite spatial resolution of the system and finite pinhole size also affects the width of the Raman peaks. The strong background in the polystyrene spectrum was not an erroneous measurement, this background was present in all polystyrene measurements using the 671 nm instrument. It is unknown what caused this feature.

4.5. Autofocus mechanism

Motivations

With the intention of mapping whole rat organs (order of magnitude 1 cm diameter) with a thickness of ~16 µm, maintenance of focus during scanning was essential. The depth of focus of ~13 µm allowed for a shift from focus in the centre of the thickness of the sample by ~2 µm either way before the laser spot was not completely within the tissue. This loss of focus reduced the total Raman signal measured, and potentially increased the background if the focal loss was into the slide and not into the air above the sample. These requirements meant we needed a way to laterally scan a sample of size ~ 1 cm with a maximum loss of focus of ~ 2 µm.

This very narrow focal range required active compensation during scanning, as the listed parallelism between the two sides of the slides used caused an effective gradient of up to ~ 5 µm / cm. Other factors, like non-parallelism between the imaging plane and the scanning stage plane could easily cause problems in measurements.

The focal correction mechanism could not use additional lasers as many autofocus modules do, as that could have interfered with the Raman spectrum or autofluorescence in the samples. These methods also correct the focus during the scan, which for our application would have unnecessarily increased the already very long scan times. The implementation described below works by measuring the angle between the scanning plane of the laser spot and the sample plane prior to the scan and evaluating a 3D coordinate transformation for the scanning path to compensate for this, moving the laser spot in (x,y,z) to where it predicts the sample will be.

Algorithm and implementation

Once the sample has been mounted on the stage, a series of calibration positions are manually recorded as described in Figure 13.

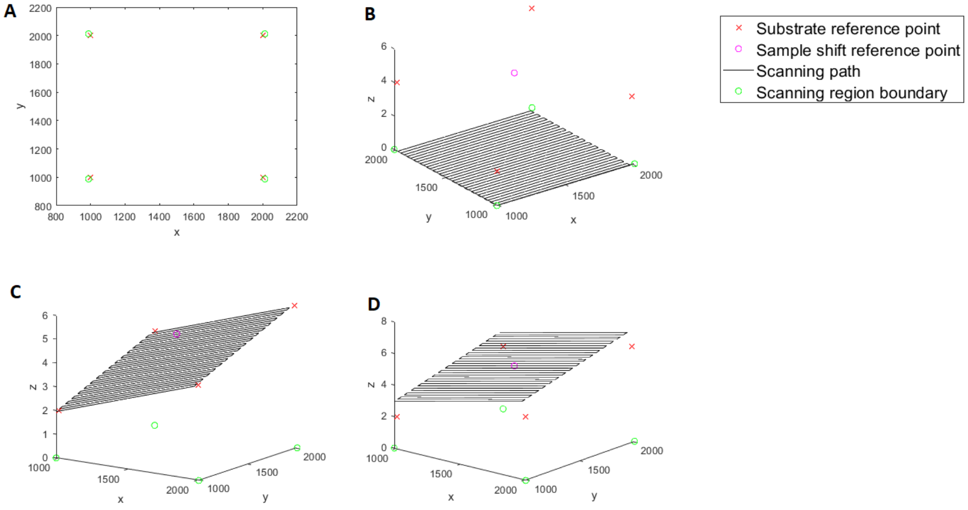

Figure 13: Autofocus correction calibration algorithm. A: A bounding box of the sample is generated by recording corners in 3D of the sample. The laser is focussed on each of these points on the upper surface of the slide, using the microscope camera. B: A 2D scanning path is generated filling this box, using the step size parameters desired. The microscope is focussed into the centre of the sample by maximising the Raman spectrum at this point (pink circle). C: The scanning path is skewed in 3D to the plane of the corner points. D: The tilted scanning path is then shifted vertically to intersect with the focus of the sample. Axes in µm. The algorithm is scalable to any size.

The sample is moved using the stage to record the corners of a bounding shape of the sample. The corner positions are focussed manually such that the laser spot is focussed on the upper surface of the slide. At each corner, the stage coordinates are recorded in (x,y,z). These coordinates are all on the same plane, that of the upper surface of the slide. This algorithm assumes that A) the upper surface of the slide is sufficiently flat to be approximated as such, that B) the sample plane is parallel to the slide surface, and C) that the sample plane-imaging plane angle is very small. The flatness of the slides used were negligibly sufficient (< 1 λ), and as the tissue is thaw-mounted to the slide, it must be parallel to the slide.

A scanning pathway is generated as a list of 3D coordinates for the scanning software to step through during the scan. Without any correction, this set of coordinates has constant z, which is how it is initially generated.

The slide surface coordinate points are interpolated to generate a flat plane at some angle to the initial imaging plane (constant z). The coordinates of the scanning pathway are then individually shifted in z to intersect with the plane. This shifts the entire scanning pathway to stay in focus on the upper surface of the slide. As the ideal focus for the system will be approximately half the thickness of the sample above this, another focal position is recorded. The Raman spectrum of a point near the centre of the sample is measured, with the focus adjusted to maximise the Raman signal at that point. The 'optimal' focus coordinates for this point are recorded, then the tilted scanning pathway is again shifted in z to intersect with this point.

The scanning pathway is now tilted to remain parallel to the sample plane and shifted axially to be in focus in the sample plane. This calibration process takes approximately 2 minutes prior to the scan, and as it requires no measurement during the scan, adds no time to the scan itself. During the scan, the focal correction is performed by the stage adjusting its position in z, so the laser spot is always in the centre of the sample thickness.

Additionally, as the scan coordinated process produces a list of absolute coordinates instead of differential coordinates, the bounding coordinates can be used as reference points for registering separate maps taken in different regions of a sample, or at different scanning step sizes. For an example of this, see the large-scale Raman mapping section of the Results chapter.

Characterisation

To evaluate the performance of the autofocus mechanism, a slide with three spatially separated clusters of 3 µm polystyrene beads directly deposited onto the slide with no fixing medium was prepared. The clusters were separated by approximately 1 cm, as shown in Figure 14. The autofocus algorithm was performed in a large rectangular region encompassing the locations of all the bead clusters measured. Brightfield images of all the clusters, as well as their (x,y) coordinates, were recorded. The algorithm was applied as described above for the entire slide, shifting the mapping coordinates for the individual bead clusters. They were then scanned with a step size of 1 µm using the 785 nm microscope with a 0.5 s integration time and laser power of 200 mW. If the Raman maps were in focus for all the bead clusters across this lateral range, then the system was capable of retaining focus for relatively much thicker samples like tissue.

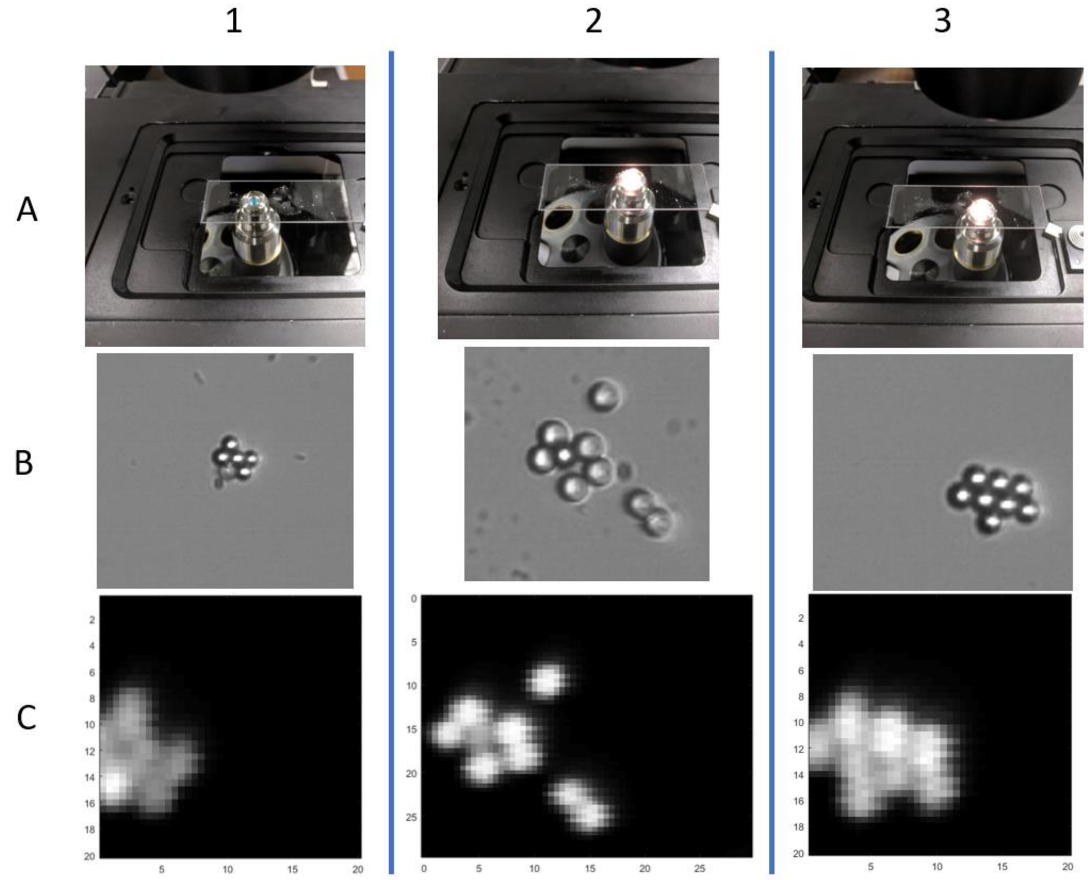

Figure 14: Evaluation of autofocus mechanism at three spatially separate locations. Bead cluster results individually numbered 1, 2, and 3. A: Location of 3 µm diameter polystyrene bead cluster on 75x25 mm microscope slide, to show physical separation. B: Brightfield image of measured polystyrene bead cluster. C: Raman intensity (1001 cm^{-1} peak) map for each cluster. Axes show size in µm.

The resulting bead maps were in focus to an error of <3 µm (measured manually by the difference in focus between the algorithmic value and that of the manual focus at each mapping position), with the intensity varying for the beads not in-plane with the rest of the clusters. As demonstrated by the lateral size of the beads in the maps not being substantially larger than that of the spatial resolution test of the microscope, the focal loss must have been small. The high numerical aperture and low depth of focus of the microscope causes rapid defocus when the z position of the stage is changed, which causes a concurrent rapid increase in object image size. This result showed that the system could maintain focus laterally. The high NA of the objective would result in a corresponding increase of the apparent bead size by ~1.7 / µm outside of the depth of focus.

Additionally, the plane tilting algorithm was applied to a blank slide intentionally mounted at a slight angle. The difference between the computed focal and the actual plane along a 5 mm length of the slide was measured, as shown in Figure 15.

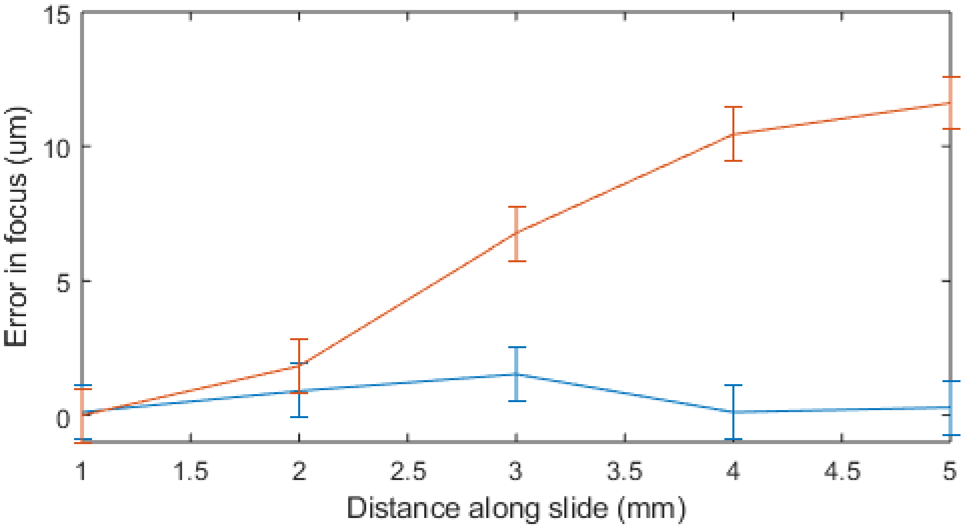

Figure 15: Change in focus on intentionally tilted slide and resultant correction from algorithm. Red: Distance between surface of slide and focal plane when uncorrected. Blue: Distance between surface of slide and focal plane when automatically corrected. Error bars due to 1 µm granularity in stage motor control, smaller steps cannot be reliably applied without risk of losing absolute stage position.

The propagation of defocus as the slide is scanned along was completely negated over 5 mm, with a total error in position of 2 µm. This result agreed with the bead cluster measurement that the focal error is less 3 µm, as required for the tissue samples.

4.6. Sample stage cooling system

Motivations

For large scale Raman mapping or for low concentration drug detection, the total measurement times can be very long - up to several days. As the samples were unfixed, they were still susceptible to tissue degradation when left on the microscope at room temperature. To minimise the potential tissue degradation, a temperature-controlled sample holder was produced. The cooling method needed to be able to maintain the sample at just above the dew point of the lab, to avoid any condensation build-up on the optical surfaces. For this purpose, the system was designed to be able to maintain as low as 5 °C indefinitely. It had to do this without any vibration of the sample, as this could cause a loss of focus – any axial shift of more than ~3 μm would bring the sample sufficiently out of focus to reduce the Raman detection efficiency and the spatial resolution of the system.

Implementation

The cooling system, shown in Figure 16, comprises an aluminium sample holder, which sandwiches the sample slide onto itself using rubber shims. This keeps the ends of the slide in thermal contact with the sample holder while leaving an open space on the underside for the objective to interface with the slide. Another open area (not shown in the figure) in the upper half of the system allows light from the brightfield condenser to the reach the sample. The temperature of the sample holder is monitored by a microcontroller, which controls the power to the Peltier modules.

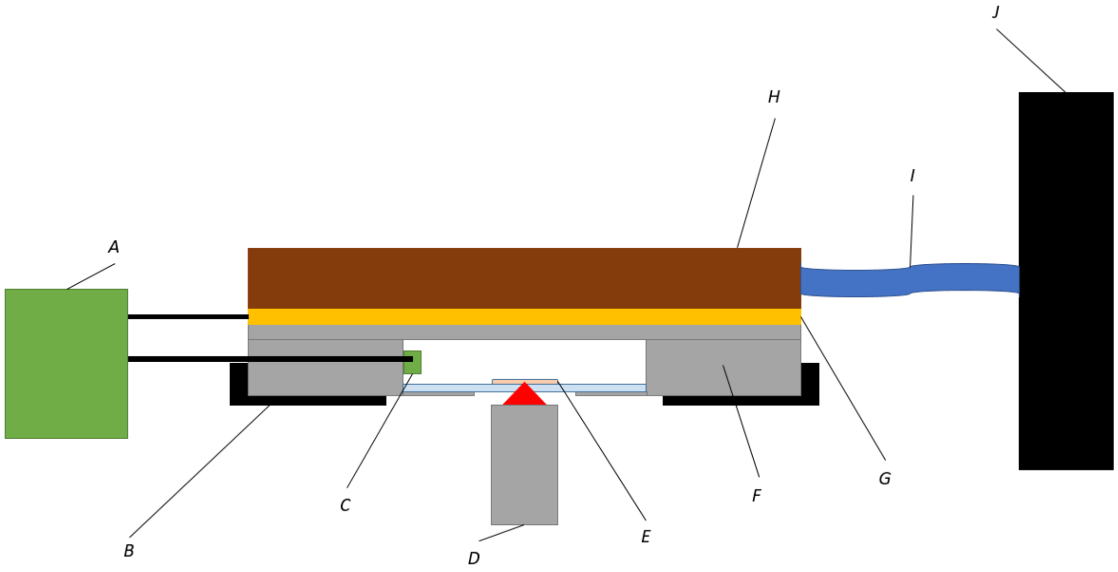

Figure 16: Sample temperature control system. A: microcontroller; B: 3D printed stage adaptor; C: temperature sensor; D microscope objective; E: sample mounted on slide; F: cooled sample holder; G: Peltier modules; H: water-cooled heat sink; I: flexible tubing; J: Radiator and pump. Not to scale.

Peltier modules are a type of solid-state heat pump, which transfer heat from one side of themselves to the other when a DC current is run through them. They are arranged so the cold side is in thermal contact with the sample holder, and the hot side is in thermal contact with water cooling blocks that are themselves cooled by a separate radiator not on the microscope itself. The temperature is controlled simply by powering the Peltier modules when the sample holder is above a set temperature, and off when below another set temperature. Peltier modules have an effective ramp-up time, before which they are adding heat to both the cold and hot sides of the modules. As a result, setting a single threshold temperature would result in rapid switching of the Peltier modules and cause unwanted heating. To minimise this, the system is programmed to overcool the stage by ~0.2 °C and not to activate until ~0.2°C over the desired temperature. This is within the accuracy of the temperature sensor used but does result in a visible oscillation in the stage temperature over time. The geometry of this design, along with the enclosed structure and thermal isolation from the rest of the microscope, minimises the required heat to be removed from the system to maintain the temperature. This allows for low water flow, which combined with the physical separation from the pump and radiator fans, results in no additional vibration to the sample during measurement.

The microcontroller used was an Arduino nano, controlling the Peltier modules and temperature sensor by code I wrote for the system. Peltier module control was performed by the microcontroller using a transistor-operated relay, necessitated by the high current drawn by the Peltier modules during operation.

Characterisation

The stability and set temperature response time of the temperature control system is shown in Figure 17. The visible oscillation around the setpoint of 10 °C was within the accuracy of the temperature (0.5 °C). The system was capable of cooling below 6 °C, but at that temperature condensation build-up began to occur on the sample holder. Condensation on the sample or on the underside of the slide, where the immersion fluid was, could have affected any measurements, so in practice the set temperature was maintained above 8 °C.

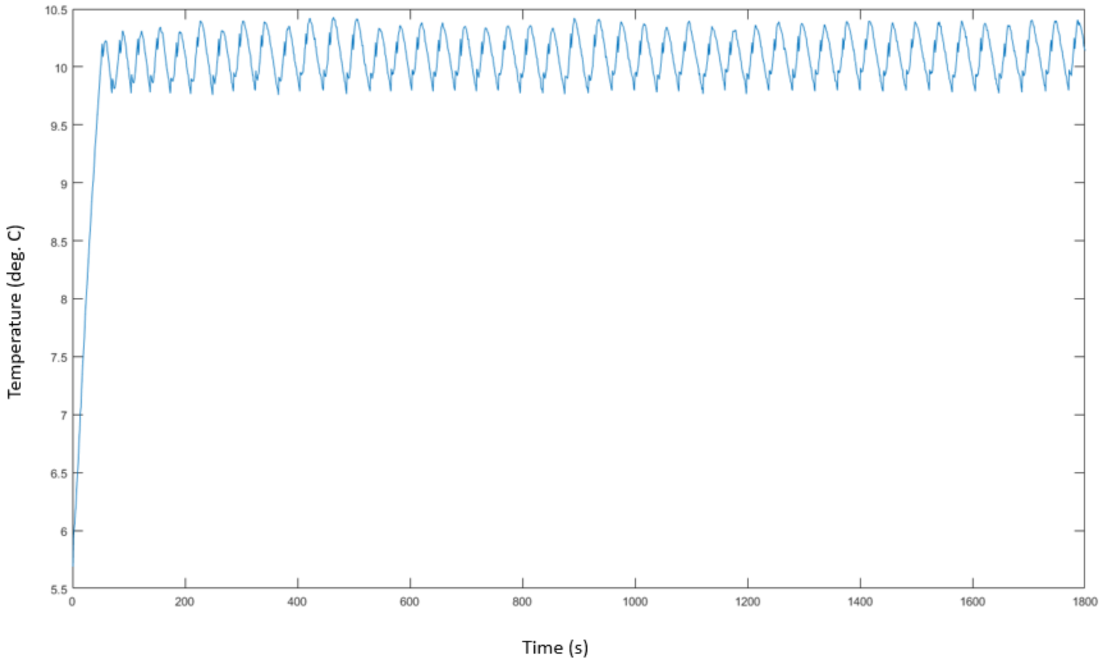

Figure 17: Temperature of sample stage over time. At t = 0 s, the temperature minimum was set to 9.8 °C, and the maximum to 10.2 °C.

The system was capable of cooling a sample to 20 °C below room temperature, with the longest test performed maintaining a sample at 8 ±0.4°C for 3 days. It could do this without any detectable vibration in the sample and without impeding the optical pathways or moving stage of the microscope. While lower temperatures were possible, risks of temperature instability and condensation were too high to consider in this sample geometry.

4.7. Data acquisition and hardware interfacing

The 785 nm laser was controlled with the included controller and keypad, and was integrated with a lab-door controlled interlock. A sample stage interlock was also implemented. When alignment had been completed, the beamline was enclosed in a metal enclosure, with exposed parts (including the back port into the microscope body) enclosed in black-painted aluminium tubing.

The 671 nm laser was controlled using a desktop computer and software supplied by the manufacturer. An identical interlock system to the 785 nm system was implemented. As the laser source and spectrometer were fibre-coupled, the free space beamline was much smaller for the 671 nm system, so it was fully enclosed in tubing.

The spectrometers, CCD detectors and motorised stages were all operated using MATLAB code I had written for the project. It enabled raster scanning, full control of acquisition settings for the CCD and for the 671 nm system spectrometer (the spectrometer in the 785 nm system was fully analogue), autofocus as described above, region-of-interest (ROI) based mapping, and repeated acquisitions. As the well depth of the CCDs was 16 bit, spectral measurements were stored as 16-bit integers in arrays along with per-point coordinates and acquisition metadata for later analysis.

The sample cooling system was operated using custom Arduino code that was given a desired temperature and maintained the set temperature automatically.

MALDI data acquisition was performed by scientists at GlaxoSmithKline using manufacturer-supplied software.

4.8. Data Analysis

Most of the spectral analysis presented in this thesis was univariate, simply defining the Raman signal of a drug using the area-under-peak value. This is the sum of the electron counts from the CCD in a wavenumber range defined by the width of the desired Raman peak, subtracting the baseline from that spectral region.

For some Raman map images shown later, principal component analysis (PCA) was performed. This is a multivariate data analysis technique whereby the data is transformed to a new coordinate system of the same dimensionality, where the direction of the first dimension is the direction in the dataset with the highest variance. The second dimension is the direction orthogonal to the first dimension with the highest variance, and so on. The magnitude of each data point in each dimension is called the ‘score’.

The practical use of PCA in this project was that the first few dimensions, or ‘loadings’, contain most of the variance in the data. This enables fast detection of spatial differences in spectra that may be difficult to discriminate on a per-wavenumber basis. Additionally, as the loadings are orthogonal, they roughly separated different spectral features into separate loadings. For example, the first loading may correspond to variance in the autofluorescent background in a tissue map, while the second may correspond to lipid concentration. Because the loadings can be visualised as a spectrum, PCA can be used to rapidly find structural features in Raman maps and attribute spectral features corresponding to them.

As a tool for rapid identification of qualitative differences, PCA has limited use in this project. This is for three main reasons. The first is that the loadings often contain negative coefficients in wavenumber space – that is, PCA can attribute negative peaks to features. This is not physically attributable to real measurements as it would require negative counts on the detector. The second is the high-dimensionality of the datasets requiring large sample numbers. The spectrometers used in this project had 1024 separate bins, resulting in 1024 measurement-long spectra. To generate a full set of components, this would require 1024 points being measured in each experiment. For basic tissue mapping with tens of thousands of pixels this is not a problem, but for the long measurements taken in the final chapter, only three points were measured, rendering PCA useless. The third issue with PCA is that it is fully unsupervised – no constraints are given to it prior to its application. As a result, PCA of different samples may give completely different loadings. This makes direct comparison of loadings and scores between samples useless.

Analysis of MALDI data was performed using custom software written by GlaxoSmithKline.

4.9. Sample preparation

All rat tissue used in this project was harvested from control animals sourced from GlaxoSmithKline. The organs had already been harvested and frozen by biologists at GlaxoSmithKline, where I then either cryosectioned and mounted them, or prepared mimetic tissue models.

Tissue sections

For initial tissue measurements, rat brain and rat liver organs were chosen. These organs were individually freeze-mounted onto chucks using 1% carboxymethylcellulose solution as a mounting medium and 12, 16 and 20 µm thick samples were cryosectioned off and mounted to fused quartz microscope slides (FQM-7521, UQG Optics).

Theses thicknesses were chosen to match the depth of focus of the instruments, while otherwise being as thin as possible to preserve inter-section tissue similarity. This is of concern for measurements requiring image registration of small features – the diameter of a cell nucleus is ~4-7 µm (randomly measured from scan in *Figure* 25). In this example, adjacent 10 µm thick sections will have completely different locations of cell nuclei, excepting nuclei that overlap the cutting plane. The diameter of the smallest feature that can be accurately registered will be approximately the thickness of the sections. Sections thinner than 10 µm were susceptible to fragmentation during the slicing process, as the pressure exerted on them by the cryosectioning blade caused them to buckle and crack before mounting was possible. Tissue sections were allowed to dry and did not have any buffer solution added. This was because the addition of phosphate buffer solution (PBS) to an one of the first sections produced caused it to loosen from the slide and float in the solution. Additionally, maintaining the water content of all of the samples at the same level would have been technically difficult to achieve, so uniform drying was chosen instead. Finally, most of the drugs used in this project were water soluble and would likely have simply been washed out from the tissue if kept in a buffer.

Mimetic tissue models

For quantitative measurements of drugs in dosed tissue with Raman spectroscopy, a calibration standard is required. This calibration standard is used to measure the instrument response of tissue containing known concentrations of drug , so that the response can be calibrated to enable quantitative measurement of drugs within dosed tissue. Mimetic tissue models are a previously designed calibration material, initially for the purpose of quantitative calibration of MSI tissue mapping[39]. They consist of an array of drug-tissue homogenates at a 'ladder' of concentrations sectioned sequentially onto the slide alongside the dosed tissue section of interest. A diagram of their structure is shown in Figure 18. They are then measured in tandem with the sample of interest to provide per-sample quantification calibration in MSI studies.

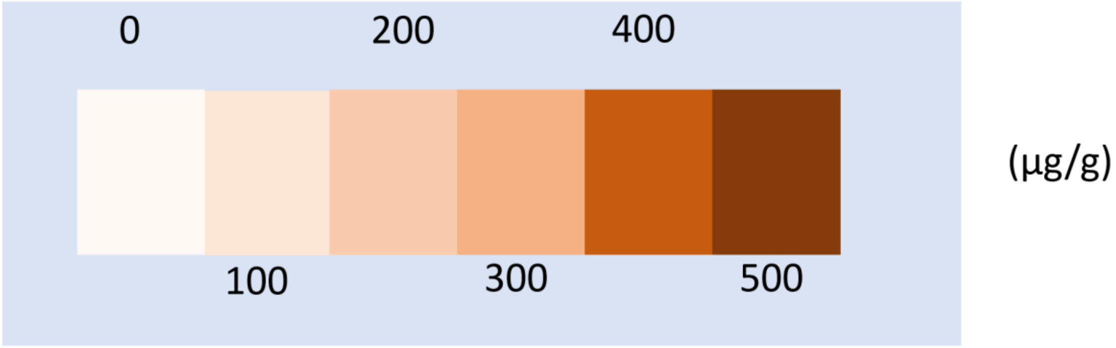

Figure 18: Schematic of 0 – 500 µg/g mimetic tissue model mounted on a slide. Each section of the model consists of homogenised control tissue re-homogenised with a solution of the drug of interest in controlled mass ratios, then added to a cylindrical mould and frozen. This is repeated sequentially until the whole model has been generated, where an axial section of the cylinder is then mounted to a slide for measurement. Each concentration region is approximately 25 mm^2. Different colours used per concentration to aid diagram, actual mimetic models have very little visual difference between different concentrations.

An example MALDI scan of a mimetic tissue model is shown in Figure 19. The greyscale area of the image is a brightfield scan of the mimetic tissue model, onto which a MALDI image of the same region has been overlaid. The different concentration regions are visibly discriminable due to slight differences in the structure made during the freezing of the mimetic tissue model. In the MALDI map, the different concentration regions are discriminable due to the different drug mass peak signal from each concentration. For full details on the MALDI imaging process, see section 7.2. This image also shows one of the strongest advantages of MALDI over Raman spectroscopy- its speed. This MALDI map was acquired with a ~2.5 Hz pixel rate, 5 times faster than even the quickest Raman spectra of tissue shown in this thesis. The drug detection speeds using Raman spectroscopy in these mimetic models are explained in full in section 7.2.

Figure 19: Mimetic tissue model of GSK4 in rat liver, at concentrations of 0, 100, 200, 300, 400, and 500µg/g. MALDI map of mimetic tissue model, with associated colour scale bar, overlaid onto brightfield scan of mimetic tissue. 250.6 Da mass fragment corresponding to the pyrrolidine, phenyl, and alkyne group, used to generate image. Scale bar represents 5 mm.

Mimetic tissue model generation

Control tissue of the organ of interest is inserted into a FastPrep tissue homogeniser, which uses stainless steel ball bearings to mechanically homogenise the tissue. This tissue homogenate is then separated into tubes and individually weighed. One is needed per concentration of the mimetic model. A known mass of the drug of interest is dissolved in methanol to produce a drug solution of known concentration. With the known masses of tissue homogenate, the necessary volume of drug solution can be calculated to generate drug/tissue homogenates of a given mass ratio. To minimise any potential differences between concentrations due to different volumes of methanol added, the drug solution is stepped down in an array of concentrations. This allows the total volume of methanol added to each concentration of the mimetic tissue model to be roughly equivalent. Although the methanol should evaporate off prior to measurement, if too much is added the homogenate will not freeze reliably which complicates later steps in the process.

The necessary volume of the appropriate drug solution is pipetted into the tissue homogenate tubes, which are then re-homogenised as before to thoroughly mix the drug and the tissue.

Once the drug-tissue homogenates are ready, a mould consisting of a syringe with removed needle-end is positioned upright in ethanol at -80 °C, with the plunger-end at the bottom and the open end above the surface of the ethanol to keep the interior dry. This provides a cylindrical mould that is maintained at cryogenic temperatures.

In order of ascending drug concentration, the homogenates are sequentially pipetted into the mould, allowing it to freeze completely solid in between each addition. This prevents any inter-homogenate drug mixing, which would reduce the accuracy of the samples. Once all the concentrations are added, the solid cylinder of tissue homogenate is left overnight at -80 °C to set.

When ready, the plunger of the syringe is used to remove the solidified mimetic model from the syringe, where it is then mounted flat to a chuck using 1% carboxymethylcellulose solution as an adhesive. As the whole sectioning process is performed at ~-18°C, both the carboxymethylcellulose solution and the mimetic model freeze and remain solid.

The mimetic model is then cut away until a sufficiently wide (>~5 mm) flat surface is produced. A section of the desired thickness is cut from this surface and mounted onto the sample slide, where it manifests as a series of rectangular regions of tissue homogenate of known drug concentration.

5. Raman spectroscopy of tissue and drug-spiked tissue

5.1. Raman spectroscopy of rat brain and liver tissue

Introduction

Prior to attempting detection of drugs in tissue, robust understanding of the instrumental response to control tissue is required. This is to assess the tissue-specific instrumental considerations listed in the Instrumentation chapter that cannot be measured using standard calibration materials. These factors are laser damage, Raman detection efficiency of tissue, spectral acquisition rate, and photobleaching. For the assessment of each these factors, identical sample preparation was used. Most of these factors were assessed by performing large-scale Raman mapping on rat brain tissue, as described in section 5.2. Photobleaching and laser damage were assessed separately later in this chapter.

Samples

Tissue Choice

For the drug delivery studies two tissue types were chosen, rat brain and rat liver. Brain, as a tissue that is high in fat and low in porphyrins, exhibits relatively low autofluorescence under visible and NIR illumination. As a very physically heterogenous organ, with many different organ substructures, it also allowed the potential for evaluation of Raman spectroscopy as a means of detecting drugs in tissues that exhibited highly varying 'baseline' spectra. In addition, analysis of drug delivery at and through the blood-brain barrier is a burgeoning field of research[99], with increased interest due to the development of novel nanoparticle-based pharmaceuticals[2]. These characteristics made it a promising tissue for theoretically low noise measurements of drugs in tissue.

Liver exhibits high autofluorescence under visible and NIR illumination[106]. As an organ of high importance in the metabolism of drugs, it was a prime choice for assessment of Raman spectroscopy for our purposes. It is a relatively more homogenous tissue, with less variation across the whole organ compared to that of the other tissue used, brain. These characteristics made liver an appropriate choice for evaluation of our instruments in highly fluorescent tissue, while also being of genuine high interest for the potential application of Raman spectroscopy.

All tissues used in this project were sourced from previously harvested organs of control animals from previous studies performed at GSK.

Laser damage

Biological samples are generally weakly scattering and susceptible to laser damage. To avoid thermal laser damage, the maximum laser power is limited, which subsequently limits the rate of Raman photon production. These two considerations limit the throughput of spectral acquisition of tissue , meaning tissue spectral acquisition is typically slow for high SNR spectra (~> 0.2 s per spectrum).

High absorption of laser light within the samples can lead to thermal damage to the sample. As the quartz-mounted samples were only to be used for Raman measurement, the threshold of what constituted laser damage was measured spectral changes to the tissue during laser illumination.

Methods

Single points of rat brain and liver sections, prepared as in section 4.9, were measured using both the 671 nm and 785 nm Raman microscopes. The points were illuminated for 15 minutes as a series of 5 s integration spectra. The laser powers tested were the lowest laser powers that had caused thermal damage in bulk tissue measurements. This was a laser power of 250 mW for 785 nm and 30 mW for 671 nm. Different laser powers were used between the wavelengths as the intention of the experiment was to evaluate the overall best wavelength for further experiments. Using the same power for both would have resulted in the throughput of the 785 nm system being unnecessarily lowered.

Once the time-series Raman spectra had been acquired, PCA was performed individually on each sample-laser combination to search for time-variation in the spectra.

Results

The results for the 671 nm instrument are shown in Figure 20. The first component, which explains > 99.5% of the variance in the time series, corresponds to the reduction in the fluorescent background due to photobleaching over the 15-minute timeframe. This spectral change can be seen in Figure 20A and C, where the background level has substantially reduced during the experiment. Subsequent principal components explain less than 0.5% of the variance and largely correspond to cosmic rays affecting readings, as shown in PC3 of Figure 20B and PCs 2 and 3 of Figure 20D. PC2 of the brain spectra aligns with the fingerprint region of the spectrum, suggesting that there was a slight change in the Raman spectra of the tissue due to laser illumination, but the change is minimal and fairly uniform over the fingerprint region.

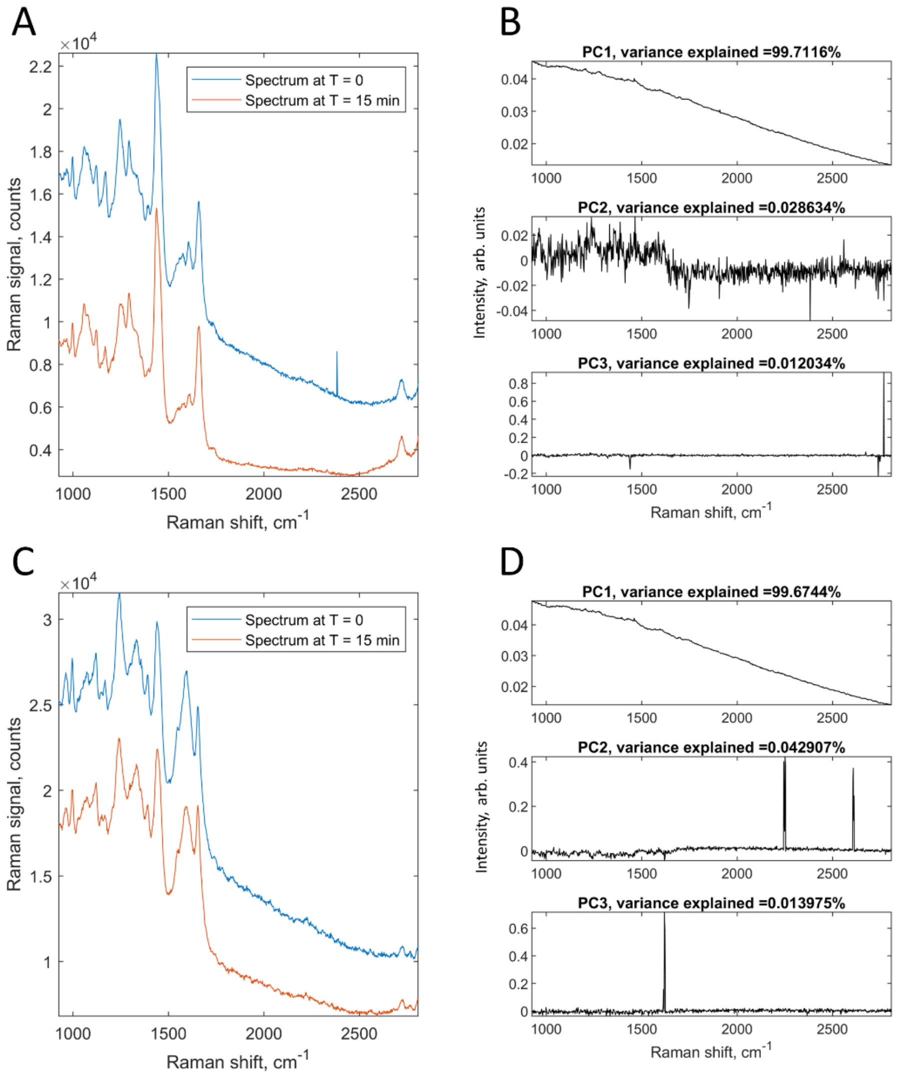

Figure 20: Results from tests for laser damage on tissue using 671 nm Raman microscope at 30 mW. A: First and last Raman spectra from rat brain time series. B: First three principal components of rat brain spectral time series. C: First and last Raman spectra from rat liver time series. D: First three principal components of rat liver spectral time series.

The results for the 785 nm instrument are shown in Figure 21. The first component, which explains > 99.9% of the variance in the time series, corresponds to the reduction in the fluorescent background due to photobleaching over the 15-minute timeframe. This spectral change can be seen in Figure 21A and C, where the background level has substantially reduced during the experiment. Subsequent principal components explain less than 0.1% of the variance and largely correspond to cosmic rays affecting readings, as shown PC3 of B. PC2 of the brain spectra aligns with the fingerprint region of the spectrum, suggesting that there was a slight change in the Raman spectra of the tissue due to laser illumination, but the change is minimal. These changes could be due to tissue dehydration physically changing the shape and therefore focus of the tissue during measurement.

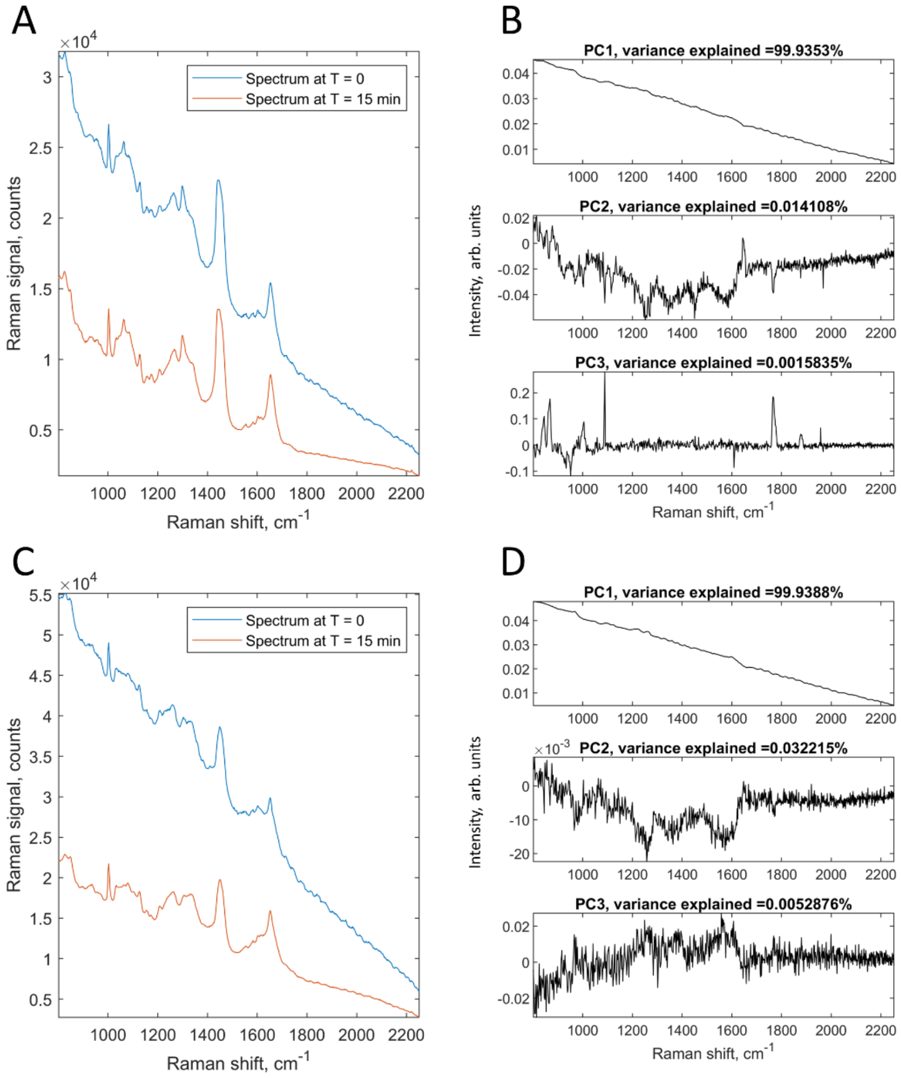

Figure 21: Results from tests for laser damage on tissue using 785 nm Raman microscope at 250 mW. A: First and last Raman spectra from rat brain time series. B: First three principal components of rat brain spectral time series. C: First and last Raman spectra from rat liver time series. D: First three principal components of rat liver spectral time series.

These insignificant changes in the measured spectra over time meant that the laser power was not increased further, to not risk damaging the limited samples we had. Depending specifically on what information is desired from the spectra, there is room to increase the laser power. For example, most of the drugs measured in this project were detected in the silent region, which has shown no spectral change during these exposures. If only the silent region is of interest, the power could feasibly be increased further.

5.2. Raman scanning of thin whole organ section of rat tissue

As biological samples generally produce weak Raman spectra, the system must be very sensitive. To validate the sensitivity to biological Raman spectra, unadulterated rat brain and liver tissue sections (16 µm thick) were measured. 200 mW 785 nm illumination was used, with the integration times labelled in Figure 22. These spectra show the detail available to be detected at relatively high speeds. It also demonstrates the differences in spectra between liver and brain. Whilst brain has low background and high signal (due to the low fluorophore presence and high fat content), liver is much noisier. This is due to the increased background signal increasing the total shot noise and as a result reducing the SNR of the Raman spectrum. The interference pattern in the silent region of the liver spectrum is caused by etaloning in the CCD[107], where reflections within the photosensitive region of the detector cause a fringe pattern. The intensity of this pattern depends on the intensity of the incident light, which is much higher in liver in the silent region as compared to brain. This is due to the stronger autofluorescence increasing the background intensity. While it does make the background appear much noisier due to its shape, the shape itself is a property of the instrument, not the sample. As a result, the shape of the interference pattern is consistent between samples. This means that it can be subtracted by the difference of two spectra and introduces little actual noise to the readings.

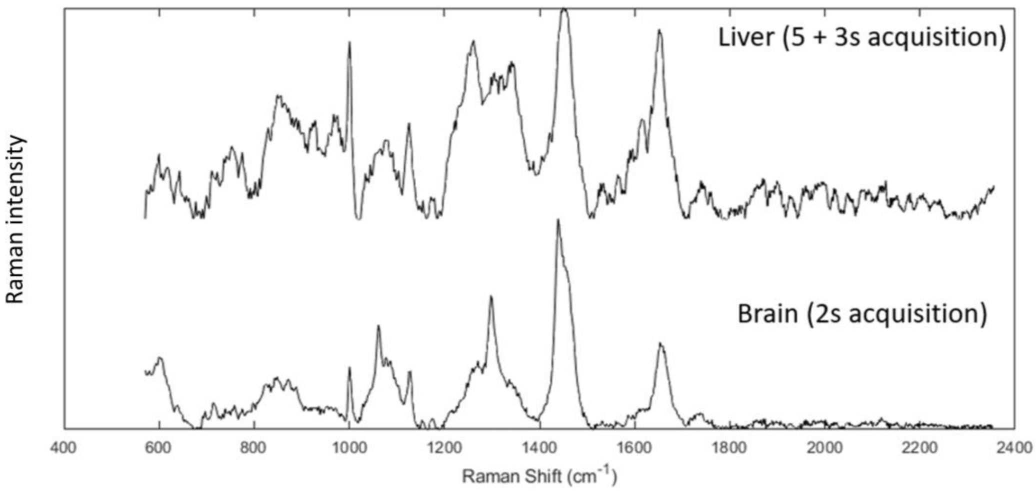

Figure 22: Raman spectra of Rat liver and Rat brain tissue sections, with labelled integration times, background subtracted using iterated polynomial background subtraction algorithm[108].The intensity of the spectra was not corrected for the sensitivity of the CCD. Here, 5 + 3 s means the acquisition area of the tissue was pre-exposed to the laser for 5 s prior to a 3 s integration of the signal to suppress the fluorescent background.

Raman spectral features of tissue

Shown in Figure 22 are typical background-subtracted Raman spectra of liver and brain tissue. They show the fingerprint regions and silent regions of these samples. Both share certain features, including the ring breathing of phenylalanine at 1002 cm^{-1}, in-plane CH bending at 1173 cm^{-1}, CH_2 scissoring at 1447 cm^{-1}, Amide I peak[109] at 1654 cm^{-1}, and the phosphate backbone stretching in the 1000-1100 cm^{-1} region[110]. Differences include the 1302 cm^{-1} peak in the brain spectrum, which is a CH_2 bending peak that is present due to the high lipid content in brain tissue, and the 1335 cm^{1} peak in liver, which can be assigned to CH_3CH_2 wagging in collagen[111]. As the spectra were not corrected for the sensitivity of the CCD, the relative peaks heights are not directly comparable. As no direct peak ratiometrics were used in this project, the relative strengths of each peak was not needed. All quantitative measurements were performed on a per-wavenumber basis.

The polynomial background subtraction used in this measurement was performed to maximise the visibility of all Raman features in the spectra. It is performed by iteratively fitting a 5th order polynomial to the spectrum and subtracting it as described in [108]. This method fits the polynomial to the broader fluorescent background, leaving the sharper Raman peaks unaffected. As it is an aggressive fitting algorithm, it performs poorly on the edges of the spectrum as shown in the liver spectrum, where the background rapidly increases towards the high wavenumber region.

These artefacts, along with the difficulty in getting repeatable results in different spectra, lead to it not being used further. As the area-under-peaks method functionally removes the background as part of the analysis, it was deemed an unnecessary source of error. For spectra in the final experiment, where the peaks were very weak, direct control tissue spectra were subtracted instead.

Region of interest mapping

To test the reliability of scanning regions at different scales over prolonged time scales, an unadulterated tissue section was used as a test sample. This enabled validation of the spatial resolution of the system, the efficacy of autofocus on expansive thin samples, and the stability of the cooling system. As a 16 µm thick sample with a width of ~1 cm has an effective X-Z 'aspect ratio' of 0.16%, this is the maximum focal loss that can be accommodated before the laser spot begins to leave the volume of the sample and the Raman sensitivity decreases as focus is lost. This is of the order of the parallelism of the slides used, so even with a perfectly level sample, active correction is required.

Methods

A 16 µm rat brain tissue section was measured, with a 2 s integration time using a laser illumination of 200 mW 785 nm wavelength into the objective. The autofocus method as described in Section 4.5 was used. An adjacent section of the sample was stained with haematoxylin and eosin (H&E) to visualise the structure of the tissue and to have a reference image to compare the Raman maps to. This stained sample was scanned using a standard brightfield scanning microscope. As the two imaging methods used different sections, the images cannot be directly registered. This is because the cryosectioning and thaw-mounting process can introduce tears and some warping to the samples. Additionally, any features smaller than the thickness of the sections, e.g., organelles or even general cell position, will not be consistent between the sections. The brightfield image does however show the scale of various structures within the brain.

The Raman maps were measured consecutively, with the largest scale map being scanned first. This map measured almost the entire section, with a 64 µm step size. As the axial resolution of the system is ~1 µm, this map was considerably under sampled. The next map was of a smaller region of the cerebrum that had no quartz artefacts (visible as parallel white streaks in *Figure* 23). This region was sampled with a 32 µm step size. Recursively smaller regions of this area were scanned at smaller step sizes, at 10, 5, 2 and 1 µm, where the spatial resolution limit of the system was effectively reached. Similar sized images of a similar region of the brain were viewed in the H&E scan to compare structures. Each Raman map was of similar pixel size, so they all took similar amounts of time to acquire. The entire sequence of maps took approximately 2 days to acquire.

PCA was performed on the maps to acquire feature information about the sample. The SNR of the spectra was calculated as the area under the phenylalanine peak (1002 cm^{-1}) divided by the standard deviation of the spectrum in the silent region. This peak was chosen as it is of similar size to several peaks in the spectrum, making its SNR value representative of them. The area under the peak was used instead of simple peak amplitude because each individual CCD bin constituted a separate measurement. By adding together the relevant bins, the total amount of signal measured is increased.

Results

The total regions scanned are shown in *Figure* 23. This figure shows the scale and approximate region of the smaller maps acquired.

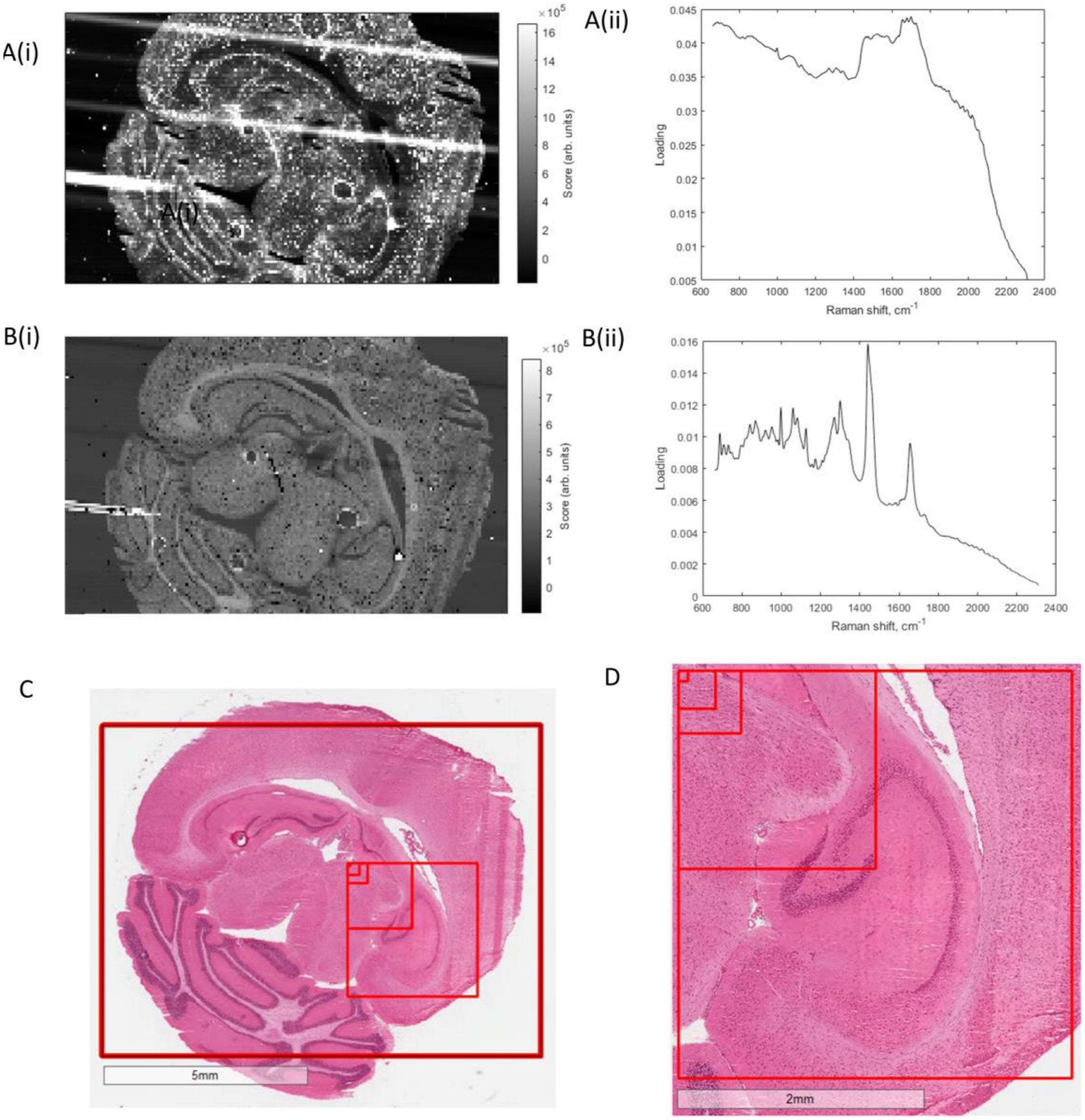

Figure 23: Large-FOV scan results of rat brain Raman mapping. A(i): Principal component score map of PC1. A(ii): PC1 loading. B(i): Principal component score map of PC3. B(ii): PC3 loading. C: Brightfield scan of H&E-stained adjacent rat brain tissue section. Red

rectangles show the regions being scanned in the Raman maps (greyscale). D: Brightfield scan of same H&E-stained adjacent rat brain tissue section, zoomed into inner scanning region. Red rectangles denote the approximate scanning regions of each Raman map.

The PC images of the Raman maps are shown in *Figure* 24 and *Figure* 25. The first PC is shown in each, which corresponds to the average Raman spectrum of the entire tissue. For the largest map, the third PC is used. This is due to regions of quartz defects present in the map, which exhibit extremely strong background and overwhelm the relatively weaker Raman spectra from the tissue in those regions. Artefacts of this are shown in the Raman maps in *Figure* 23, where parallel ‘streaks’ are present primarily in the PC1 map in A(i), and to a lesser extent in B(i). The loading in A(i) shows that the spectral fingerprint of these regions is similar to that of glass, indicating defects in the slides used. Subsequent scans were performed in an area free of these defects to avoid these artefacts. Various ring-shaped objects are also visible. The larger rings are water droplets that have settled on the samples, likely during thawing. In *Figure* 23B(i) and C, the superstructures of the brain are visible, including the cerebellum in the lower left, and the cerebrum above. The individual lobes, separated by the regions of high nuclear density in the H&E image (deep purple) are also visible in the Raman map[112].

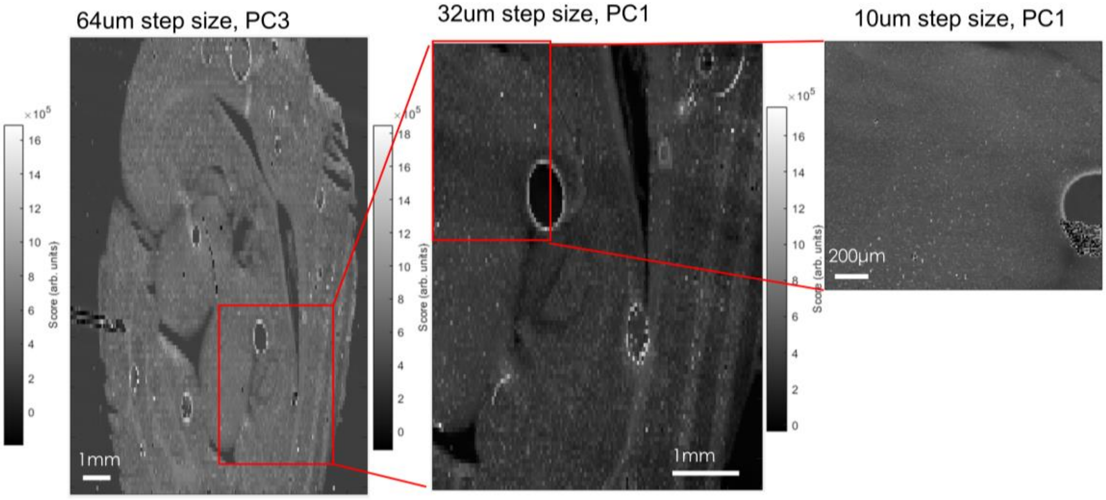

Figure 24: Principal component maps of consecutive smaller scale Raman scans of rat brain tissue section. Red rectangles denote the approximate FOV of the subsequent map.

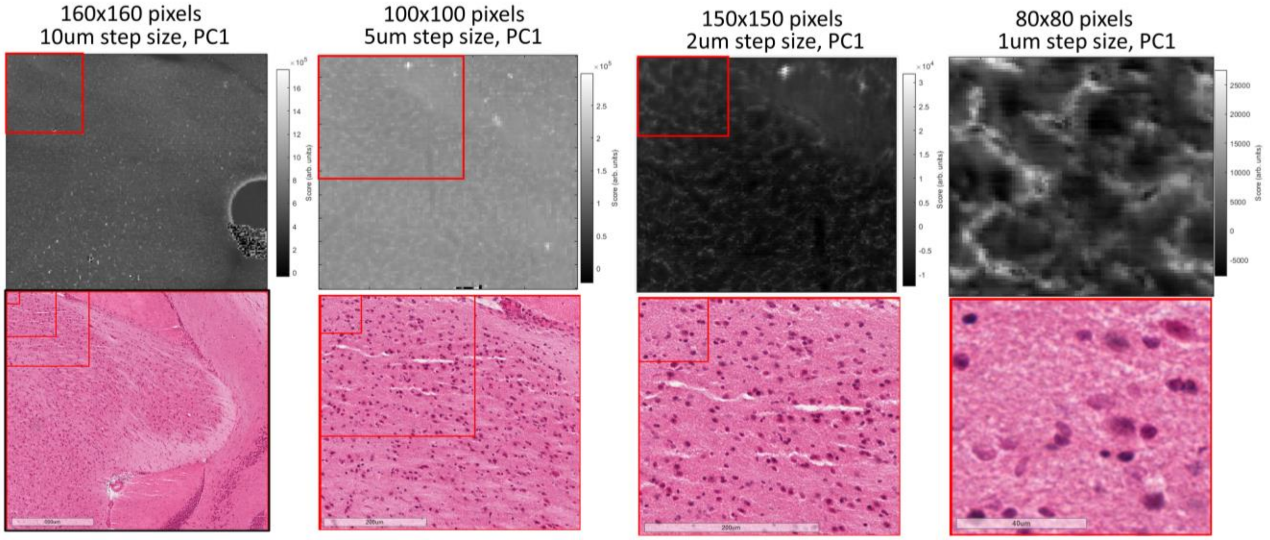

Figure 25: Principal component maps of Raman scan, and representative brightfield image of same scale of tissue of the same type. Red rectangles denote the approximate FOV of the subsequent map.

Representative spectra from the first and last scans performed are shown in Figure 26. The background intensity and spectral features are more varied in the large-scale map, explained by the inherent variability in the tissue at cm scales. From the smaller map, the spectra are less varied, with more consistent fluorescent background. The SNR for the spectra in Figure 26A were ~210, and in Figure 26B were ~220.

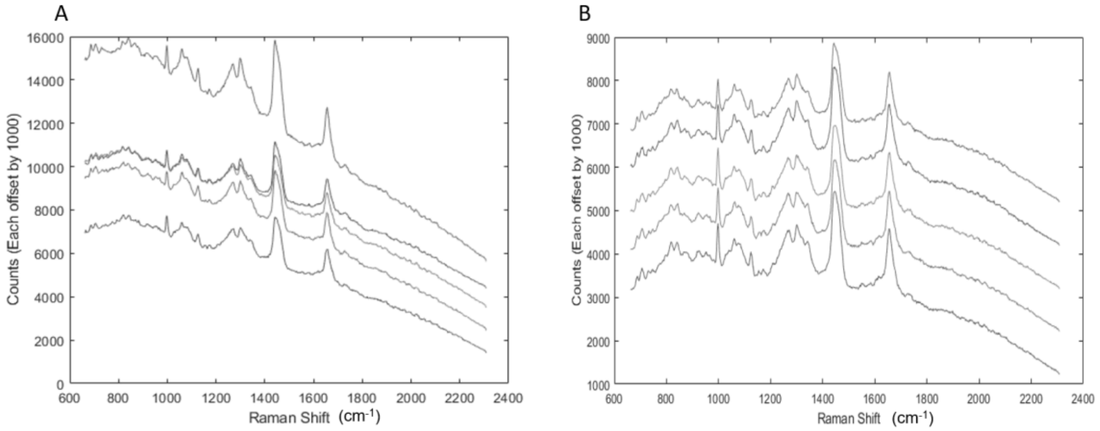

Figure 26: Raman spectra from large-scale Raman scan. A: 5 randomly selected Raman spectra from points in the 64 µm step size scan, each offset sequentially by 1000 counts

for visibility. B: 5 randomly selected Raman spectra from points in the 1 µm step size scan, each offset sequentially by 1000 counts for visibility.

Discussion

The scans in Figure 22 show features of a similar size to features in the adjacent H&E image, whilst also showing agreement between each other for regions scanned multiple times. In Figure 25, the upper left corner of all of the Raman scans correspond to the same coordinate in the sample. The result of this is that the series of images can be compared as the entire region in the smallest area scan is fully scanned in each of the larger scans. This region can then be compared between the images to show the same features are visible in varying clarity. As they all agree, the scanning protocol is very repeatable and reliable. It also demonstrates the spatial resolution of the system. If a scan has a step size below the spatial resolution of the system, no extra information or smaller features can be distinguished. However, each subsequent scan in the series shows further clarity and as such the spatial resolution can be assumed to be smaller than the step size of the second smallest scan, which in this case is 2 µm. This agrees with the polystyrene bead tests described in section 0.

The spectral features present in brain are clearly visible in Figure 26, with strong Raman peaks and generally smooth silent region. The ring deformation in cholesterol at 700 cm^{-1}, phenylalanine ring breathing at 1001 cm^{-1}, Lipid CH_2 deformation at 1300-1500 cm^{-1} and C=C vibrations at 1657 cm^{-1} [113]. The silent region exhibits weak etaloning fringes, that are consistent in shape between measurements as they are an artefact of the detection pathway.

There are no significant spectral differences between the earlier scans and the later ones, demonstrating that any chemical changes to the sample over a 48-hour scan were minimal and can be ignored, assuming that the sample is kept as it was here at 8 °C. Additionally, the SNR difference between the two is minimal, with what change there is explained by the visible reduction in background between the two scans.

Conclusions

This experiment has shown that the 785 nm instrument is capable of wide-area scanning of thin tissue samples, acquiring Raman spectra with SNR greater than 200 in reasonable times (0.5 Hz pixel acquisition rate, corresponding to a 30-minute scan time for a 30x30 map), using laser powers below the tissue damage threshold. This experiment, and all other tissue mapping experiments, were not performed using the 671 nm system because the system had not been built by the time these experiments were performed. The first tissue-based experiments performed on the 671 nm system were the drug detection comparisons shown in Chapter 7.

5.3. Detection of drug spiked onto tissue using Raman spectroscopy

As a first test of the efficacy of the system to detect drugs in tissue samples, dosed tissue analogues were produced. These consisted of tissue cryosections 16 µm thick and approximately 1 cm in diameter, mounted on quartz microscope slides. Two tissues were tested: rat brain and rat liver, sourced from control animals from previous studies. Six deuterated drugs produced by GSK were pipetted directly onto the tissue sections with a pipette at three different concentrations: 500 µg/mL, 100 µg/mL and 1 µg/mL. The high concentration was used to determine which drugs produced Raman bands that could be detected through tissue, as such a high concentration is not representative of any drug taken in practise. The two lower concentrations are within the range of actual pharmacological concentrations of administered drugs and acted as benchmarks for detection in a potential animal study. See Figure 27 for a visual description of the samples.

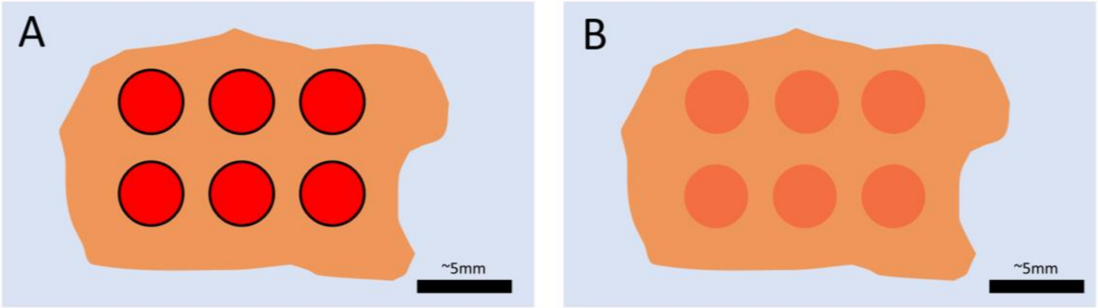

Figure 27: Approximately to-scale arrangement of drugs pipetted onto thin liver tissue sections. Multiple spots were applied to each tissue section. A) Drug 'droplets' (red) immediately after being deposited on to the section. B) The same regions after the drug solvent has evaporated away. Most of the drug is either absorbed into the tissue or dried on top of the tissue. Tissue sections approx. 1.5 cm in length.

The samples then consist of tissue sections with circular regions containing drug. The rest of the tissue area is not dosed and can be used to determine the background signal from the tissue.

In the experiment, the samples were scanned using the 785 nm Raman system, being maintained at ~8°C to minimise any tissue degradation. Scans were performed using a 785 nm laser producing 200 mW at the microscope objective. The details of the scan depended on the tissue type being scanned and the drug.

Materials and methods

Drugs

The drugs used were all proprietary compounds produced by GSK. Their molecular structures are shown in *Figure 28*. They all contain ^{2}H-substitutions, while GSK4 also has an alkyne bond. The deuterium substitutions change the vibrational modes of the relevant bonds and as a result, change the Raman spectra. In some cases, new peaks are present in the otherwise 'silent' region of the spectrum, at around 1800-2800 cm^{-1}. These new peaks have no overlaps with the peaks from the biological sample and in theory would be therefore easier to discriminate. As the expected range of spectral features included the fingerprint region and the Raman silent region, the spectrometer was adjusted to keep these in the FOV.

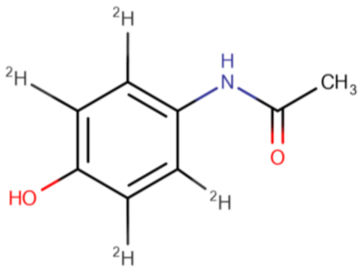
GSK1

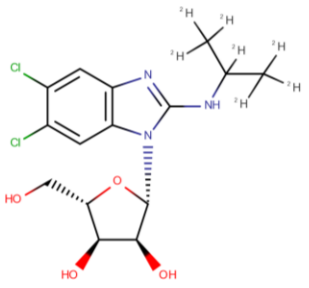
GSK2

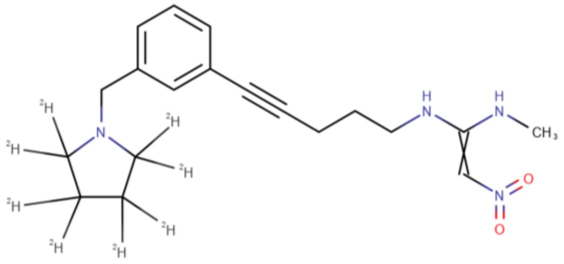
GSK4

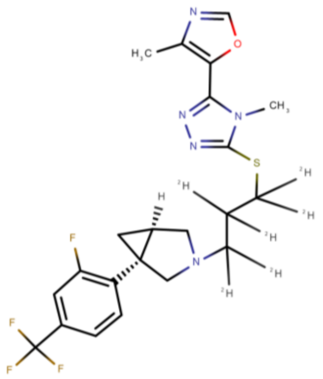
GSK10

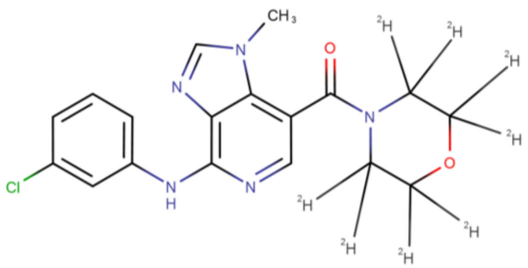
GSK11

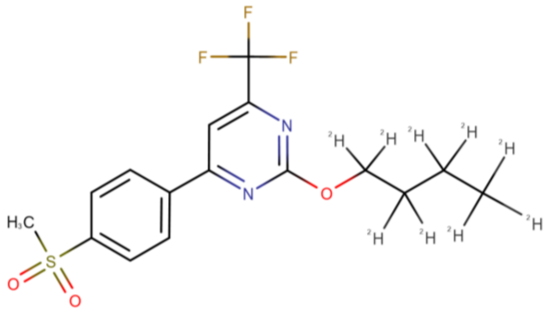
GSK13

Figure 28: The deuterated compounds tested in this study. These drugs are referred to by their 'GSKx' nomenclature as labelled in the figure.

Drugs spiked onto brain tissue sections

The scanning parameters varied based on the drug and tissue type: some drugs produced weaker Raman signals and spectrum integration times were then raised to up to 5 s, while stronger drugs were scanned with 1 s integration times.

In all, six drugs at three concentrations produced 18 spiked areas to be measured. The entire tissue sections were scanned at a step size varying by sample, to generate maps of size between 100 and 200 pixels on each side. This was done to maximise the tissue variation within the scans, and to make sure that both spiked and non-spiked regions were mapped. The drugs were spiked onto the tissue dissolved in water, which evaporated after application. The solution drying out on the tissue left ring shaped outer regions higher in drug concentration than the centre of the spot. The rings were approximately 100 µm wide.

Data Analysis

To discriminate the spiked regions from the bare tissue regions, the Raman spectra were analysed. Principal component analysis (PCA) was then used to separate the drug spectra from the tissue spectra. PCA reduces the dimensionality of high-dimensional data like Raman spectra by finding the loadings that have the maximum variance. As the large scans have many more spectra than dimensions (a 200 x 200-pixel map is made up of 40000 spectra, but each spectrum has 1024 dimensions), PCA can reliably be used for dimensional reduction. The loadings calculated show the spectral features that have the most inter-pixel variance, and the scores of each pixel show the dot product of the spectrum in that pixel with the loading specified.

Results

GSK1

The results of the GSK1 spiked on brain tissue sections are presented in *Figure* 29. Here the first 6 PC loadings and score maps are shown, to display the information that can be extracted from the spectra. For the rest of the results, only the relevant loadings are shown. The first component corresponds to the background fluorescence of the tissue, which is present everywhere in the tissue to varying degrees, but not in empty regions of the map. The second component shows parallel stripes that smear over the map and exhibit a strong broad feature in the 1500-2000 cm^{-1} region of the spectrum. These are artefacts from the quartz slides the samples are mounted on. Unlike the rest of the slide, which has a low, flat spectrum above ~ 1600 cm^{-1}, these regions have a broad 'bump' in the aforementioned region similar to the spectrum of regular microscope slide glass. These features were only present on certain batches of the quartz slide. After this investigation, all slides were scanned and checked prior to sample mounting to prevent avoidable mismeasurements and sample waste. PC3 corresponds well with the average tissue Raman spectrum of brain, with the white matter of the cerebellum in the lower right and the cerebrum in the upper left clearly visible. White matter is high in fat and therefore exhibits strong Raman peaks attributed to fat, such as the 1447 cm^{-1} and 1653 cm^{-1} peaks. PC4 has a lower SNR, but shows the grey matter of the cerebellum, with corresponding increase in the 1000-1100 cm^{-1} region of the Raman spectrum. PCs 5 and 6 show the location of the spiked GSK1 in the map, with both the high concentration spot in the centre and the low concentration spot ring centre-left shown in PC5 (circled in *Figure* 29). These loadings both show a silent region peak from the GSK1.

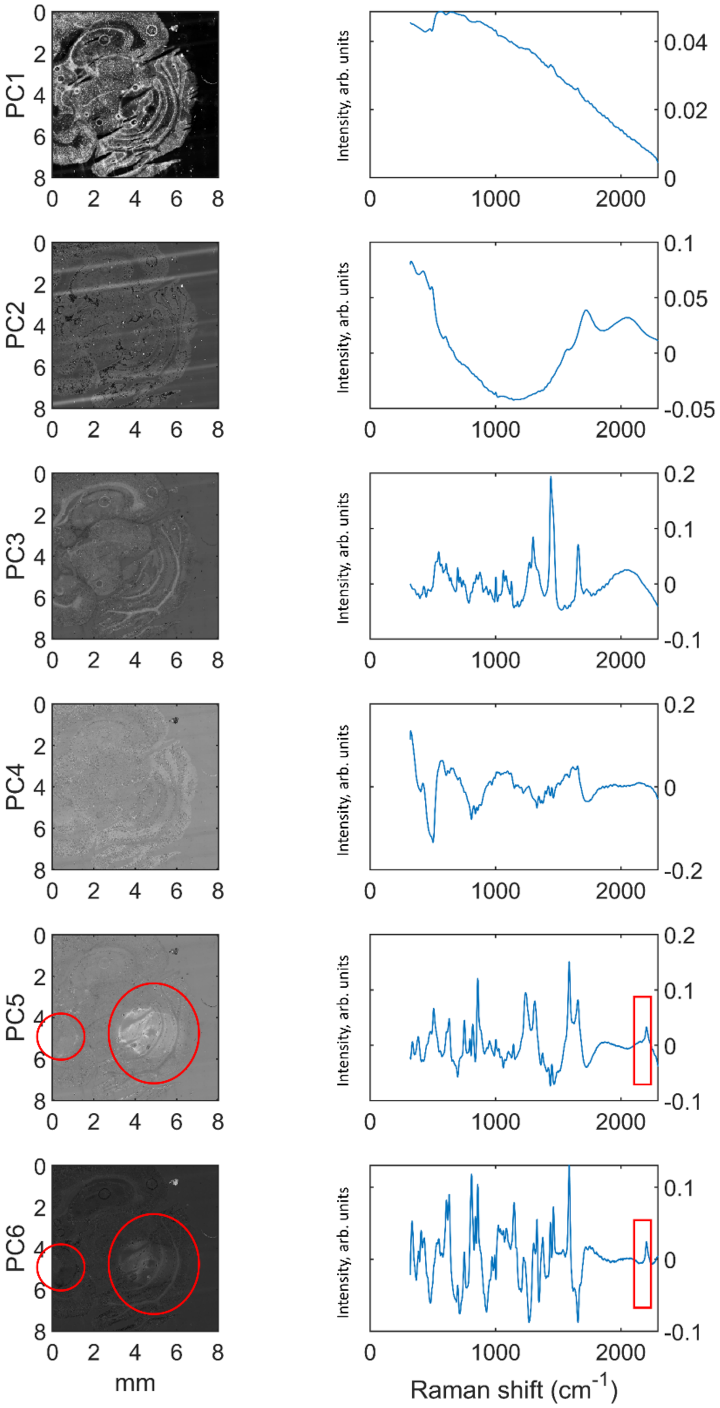

Figure 29: First 6 Principal component score maps generated from Raman map of GSK1 spike onto 16 µm brain section. Each image (left) is generated from the value of the individual pixel in the loading to its right. Spiked regions in PC5 and 6 circled in red. Axis labels indicate distance along edge. Silent region 2276 cm-1 peak of D-C bonds in GSK1 highlighted with red rectangle in loadings where visible.

GSK4

The results of the GSK4 spiked on brain sections are presented Figure 30. The bright region in the lower centre is from the 500 µg/mL concentration drop. Apparent cracks in the spot are tears in the tissue section reducing the mass of drug absorbed and retained. The spectra in Figure 30 B show that primary differences between the tissue alone and the combination of the tissue and drug. Primary differences include the 1000 cm^{-1} from the phenyl group and the broader 1250 cm^{-1} peak from the deuterated pyrrolidine ring. Also present is the 2220 cm^{-1} peak in the silent region. The features of the 'drug' principal component correspond well to the spectral differences shown in *Figure 30*. The 100 µg/mL spot present on the same section, directly above the 500 µg/mL spot, is only barely distinguishable in the drug PC map, where a circular arc corresponding to the lower edge of the spot is visible. Gaps in the spot correspond to cracks in the tissue section. In *Figure* 30 *A and B*, the drug spiked region can be seen with only the 1001 cm^{-1} peak.

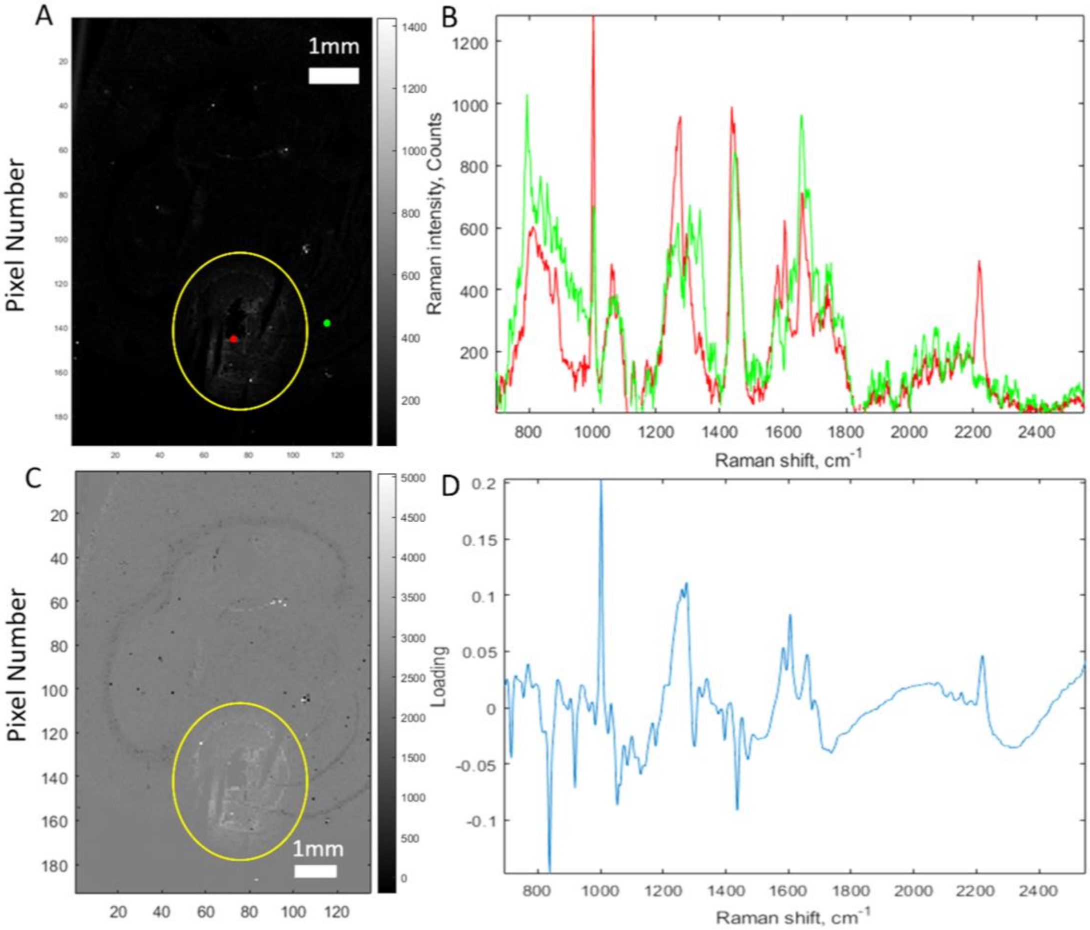

Figure 30: Raman maps identifying GSK4 spiked onto unfixed rat brain tissue. A) Map generated by the height of the 1000 cm-1 peak in each spectrum. The bright region (circled in yellow) in the centre is from the 500 µg/mL concentration drop. B) Individual spectra taken from map at locations represented by coloured dots in A. Green spectrum taken from non-spiked region, red spectrum taken from spiked region. C) PC map from the PC in D). D) The principal component showing an assumption of the Raman spectrum of the drug.

GSK10

The results of measuring GSK10 on rat brain are shown in Figure 31.

This drug was difficult to detect in/on brain tissue, with only the 500 µg/mL concentration visible on Raman maps using PCA. The tissue map in Figure 31A shows the PC map generated from the PC1 of the Raman map. This image has a gradient, suggesting that the autofocus did not operate properly. As the darkest region also corresponds to the region with the drug spike, shown in Figure 31C, the system was likely out of focus in that region, resulting in reduced Raman sensitivity in the region of the spike. Nevertheless, the 500 µg/mL spot is visible on the image as circled, along with a few weak silent region peaks at 1910 and 2000-2100 cm^{-1}. These peaks are present due to the deuteration of GSK10.

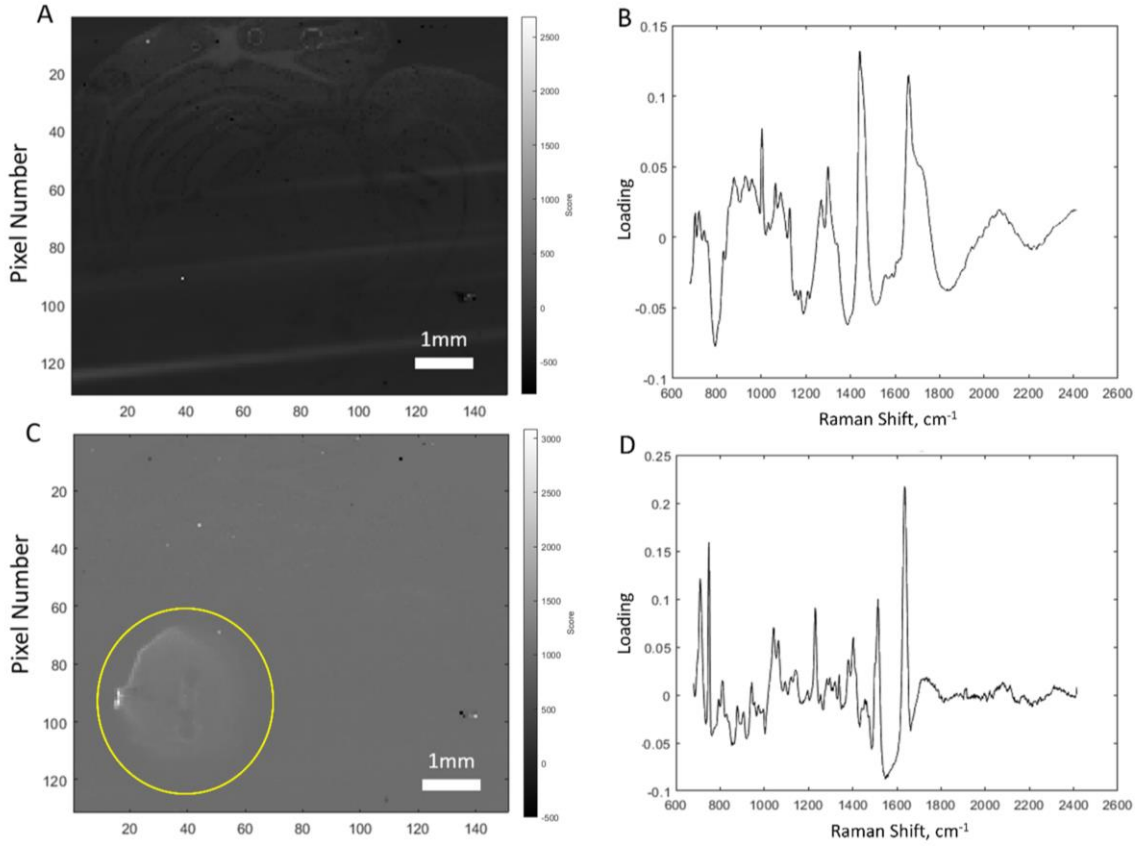

Figure 31: Raman PC maps of GSK10 spiked brain tissue section. A) PC map from PC1. B) Loading of PC1. C) PC map from the PC3, shown in D). This loading was chosen to show as it showed the location of the spiked spot with the highest contrast. Axis labels on A) and C) indicate pixel number.

Other samples

The drug/tissue combinations not shown here had no detectable drug spikes at any of the concentrations used. They are indistinguishable from non-spike tissue and have not been included. These were the drugs GSK2, GSK11 and GSK13 at all concentrations prepared (1, 100, and 500 µg/mL), as well as the 1 µg/mL spots of GSK1, GSK4 and GSK10.

Drugs spiked onto liver tissue sections

Illuminated by a 785 nm source, liver autofluoresces strongly. This autofluorescence is much stronger than the Raman scattering and overwhelms it at the detector. As the signal-to-noise ratio (SNR) of the detector is proportional to the square root of the detected signal, the large added background signal from the autofluorescence increases the noise floor. For liver samples, this is often much stronger than the Raman signal. This raises the noise floor of the spectrum above the size of the spectral features, making the Raman signal undetectable.

To reduce the background autofluorescence from liver, two actions were taken. The first is to prepare the sample to be as thin as possible to reduce background from out-of-focus tissue. The second was pre-measurement photobleaching. Photobleaching is a non-reversible chemical process in which the fluorophores in the tissue are permanently made unable to fluoresce by illuminating them with high-power light (in this case, the pump laser). By photobleaching the sample prior to measurement, the autofluorescence at the time of measurement is significantly reduced. For liver, using 200 mW@785 nm, this time was 5 - 8 s and since it was being done by the laser, it had to be performed at each point. A time-series demonstrating the effects of photobleaching is shown in Figure 32. The spectra here are from a single point being continuously illuminated and measured over time, with the first measurement at the top and the last at the bottom. As the exposure time increases, the background is suppressed without reducing the Raman signal. This improves the SNR of the Raman spectrum acquired and reduces the likelihood of CCD saturation (shown here in the regions of the spectra where the signal tops out at 2^{16} counts, the well depth for the CCD used.). As the bleaching time increases, the Raman signal remains constant in strength, but the autofluorescent background decreases. This reduces the noise contribution in the spectrum from the background.

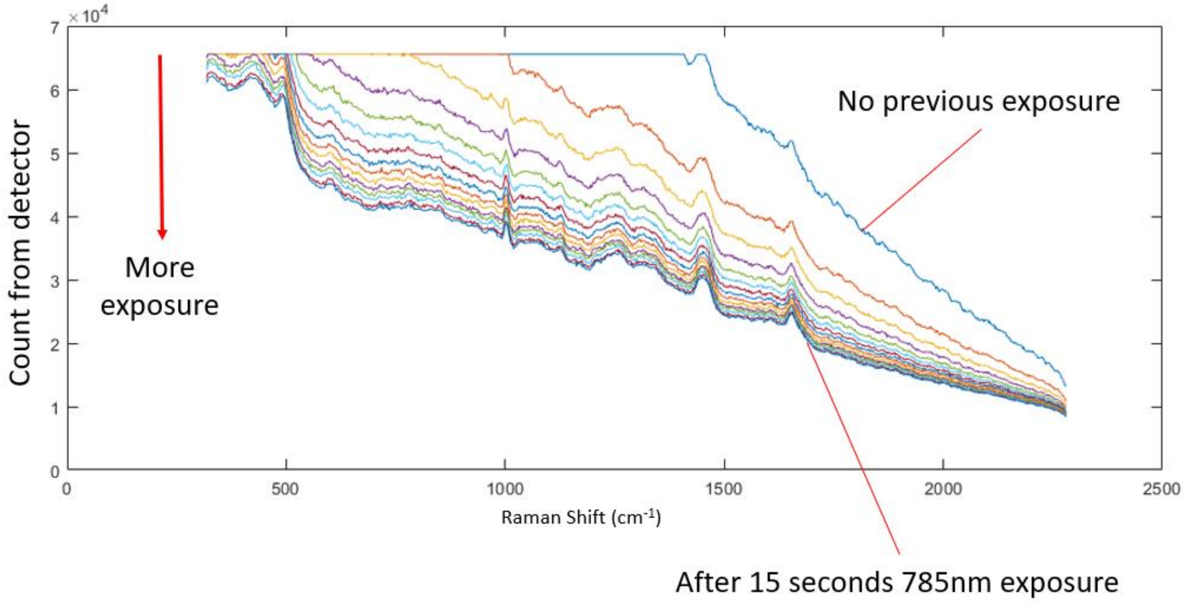

Figure 32: Time-series of Raman spectra of single point within liver section, 1 s integration of 200 mW@785 nm for each spectrum, starting from 0 exposure to 15 s of laser exposure.

Results

Whilst the background signal from liver tissue is much stronger than that of brain, reducing the SNR of the Raman signal, the tissue itself has much less variation. In spiked tissue maps, liver appears as a homogenous shape that contains no apparent sub-organ structures. This factor can make finding the changes in the spectra due to the presence of drug much easier than finding the drug in brain. As the liver is effectively homogenous (ignoring subcellular structures), the acquired signal can be characterised as a sum of the background signal, the liver signal and the drug signal.

GSK4

GSK4, like all of the drugs tested, contains a phenyl group. This group exhibits a sharp 1001 cm^{-1} peak in the Raman spectrum. In this case, it is not sufficiently strong to be detectable at low concentrations, as Figure 33 shows. It is only visible at the high 500 µg/mL level in/on liver. While the locations of all the spiked regions are distinguishable in Figure 33A as 'craters', these shapes do not contain any spectral features indicating significant drug detection. The 'crater' shapes may be due to tissue displacement or deformation during the drug spiking process.

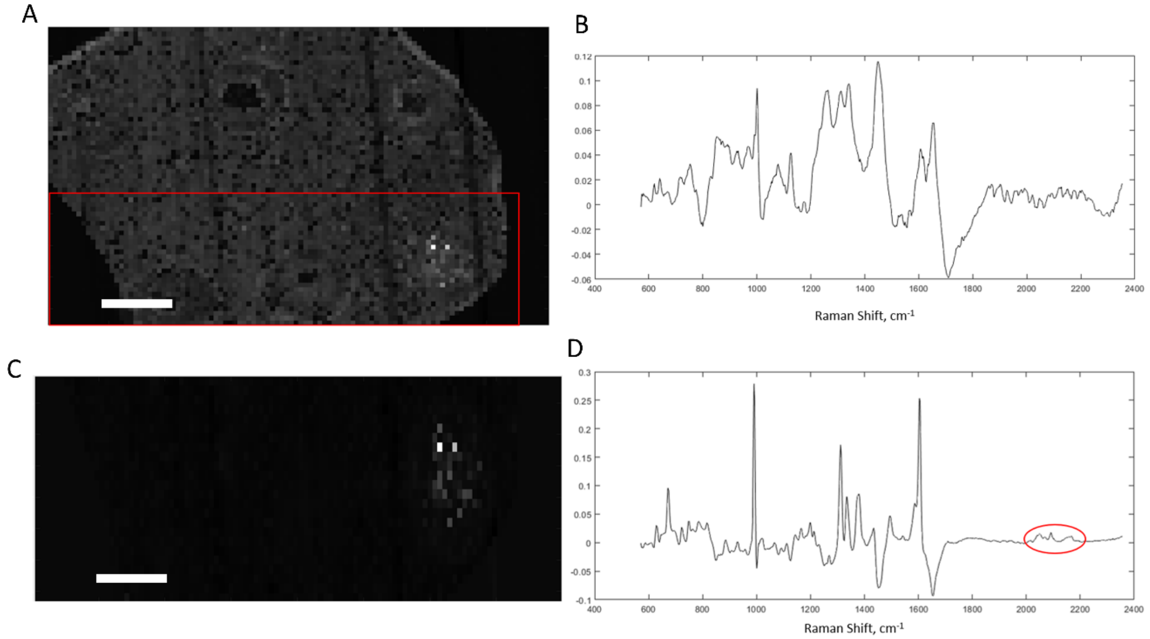

Figure 33: Raman spectral images of GSK4 spiked on liver tissue section. Area in red rectangle is the area imaged in C. A) Raman image of PC1 of Raman spectral data. B) PC1, used to generate A. This component shows the regions in the map where liver is present, to show the overall shape of the section. C) Raman image of principal component that shows spiked regions on the map. The bright region on the right is the 500 µg/mL concentration region. D) Principal component used to generate C. The circled feature is a Raman peak from the drug that is present in the silent region, present due to the deuteration of the drug. Scale bars represent 2 mm.

The alkyne peak at 2220 cm^{-1} visible in the GSK4/ brain sample (*Figure 30*) is not visible here, while the silent region peaks from the GSK4 are.

GSK10

Figure 34 shows the spiked regions visible, in addition to the liver region in the scan. The liver section imaged has two separate drugs spiked in different places, the other drug contaminating the first principal component. GSK10 exhibits a strong spectrum, easily detectable through liver tissue. The brightest region on the right in Figure 34*C* is the location where the 500 µg/mL concentration drug was spiked onto the section. The less bright region in the centre corresponds to a 100 µg/mL concentration and the least visible region farthest to the left was spiked with a 1 µg/mL concentration of the drug. This region is hard to see at this image scale, as the colour scale is dominated by the higher concentrations.

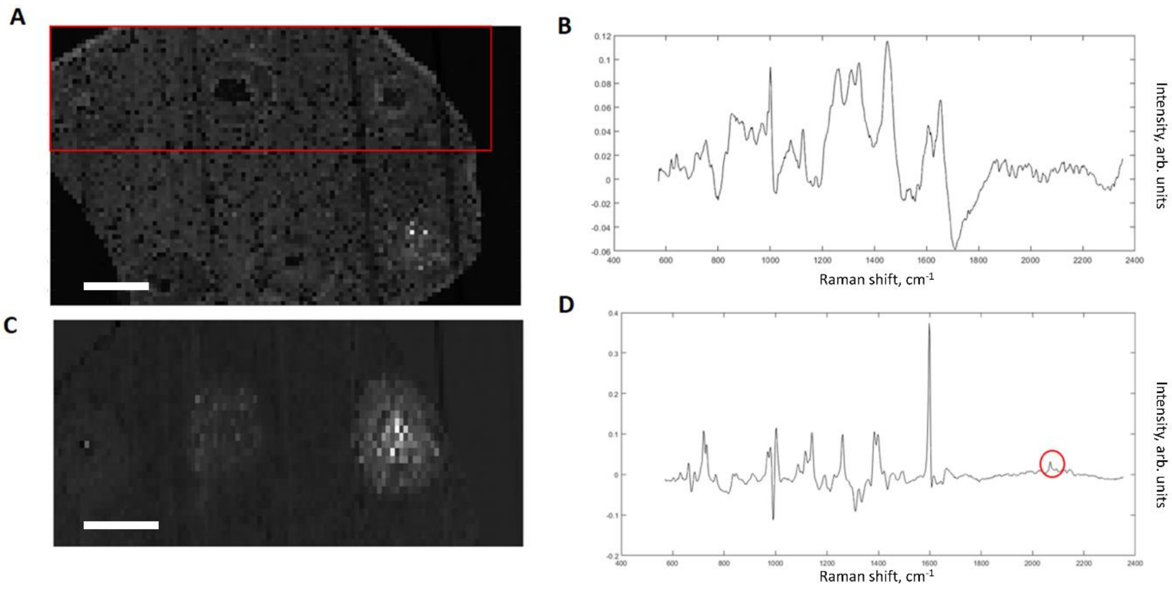

Figure 34: Raman spectral images of GSK10 spiked on liver tissue section. Area in red rectangle is the area imaged in C. A) Raman image of PC1 of Raman spectral data. B) PC1, used to generate A. This component shows the regions in the map where liver is present, to show the overall shape of the section. C) Raman image of principal component that shows spiked regions on the map. The bright region on the right is the 500 µg/mL concentration region. Bright region in centre is the 100 µg/mL spiked region, and the dim spot furthest to the left is the 100 µg/mL region. D) Principal component used to generate C. The circled feature is a Raman peak from the drug that is present in the silent region, present due to the deuteration of the drug. Scale bars represent 2 mm.

Other samples

The drug/tissue combinations not shown here had no detectable drug spikes at any of the concentrations used. They are indistinguishable from non-spike tissue and have not been included. These were the drugs GSK1, GSK2, GSK11 and GSK13 at all concentrations prepared (1, 100, and 500 µg/mL), as well as the 1 µg/mL and 100 µg/mL spots of GSK4.

5.3.1.1. Discussion

Liver presents around 2-10 x stronger autofluorescent background for the same illumination time and power relative to brain, depending on amount of photobleaching, which in turn increases the shot noise present even in processed spectra by a factor of ~1.4 - 3. The increased background also increases the etaloning fringes in the spectra by a factor of ~2-10, making the discrimination of the Raman bands of the drugs more difficult. Despite this, the spectral homogeneity of liver makes the background less variable between different locations within liver. These factors result in the non-drug contributions to the Raman spectrum generally being less structurally variable, but higher in actual detector noise. With careful tissue spectrum subtraction, the effects of the tissue on drug detection could be ameliorated.

Conclusions

While the concentration of the drugs added is known, the distribution of the drugs on the tissue samples is unknown. The drug does not settle homogenously on the tissue during drying, but generally accumulates heterogeneously. It is uncertain how much of the drug solution is absorbed into the tissue, and how much simply dries on top of the tissue. Additionally, a large volume of the solution was added, relative to the volume of the tissue sections. As a result, these samples do not accurately represent drug distributed in dosed tissue and cannot be used to determine detection limits of the drug in a specific tissue using Raman spectroscopy.

This study does, however, show that the drug can be detected, at concentrations likely higher than in the solutions applied, through both rat brain and rat liver, which shows promise that the drugs used could be measured in more representative studies.

6. Model for predicting the detection limit of concentration of drug in tissue using Raman spectroscopy

6.1. Introduction

The drug concentration within tissue can be calculated using the strength of the Raman spectrum of the drug. In an ideal system, the height of any Raman feature is linearly correlated with the number of drug molecules in the volume being measured. In practice, this signal is combined with the Raman spectrum of the tissue and various background signals before being measured in the spectrometer.

Each of these sources of light increase the detection noise in the spectrometer and affect the signal-to-noise ratio (SNR) of the drug spectrum measured. By making assumptions about how different experiment parameters affect the strength of these individual signal sources, the SNR of the resultant drug spectrum can be modelled. By allocating a threshold SNR to assign a drug spectrum being ‘detectable’, the minimum drug concentration detection limit can be approximated.

Raman spectra and background signal

For most of the drugs tested, there are Raman spectral features in both the fingerprint region and the silent region, due to their deuteration. The fingerprint region is where both the tissue spectral features and the tissue background are strongest, so the noise is also strongest there. The ‘best’ features of the drug spectra depend on the SNR at each wavenumber. Picking the features with the best SNR requires balancing these factors. A representative Raman spectrum of a control liver mimetic tissue model is shown in Figure 35. It shows the strong intrinsic peaks of the fingerprint region and the flat background of the silent region. Additionally, the silent region also exhibits less background autofluorescence.

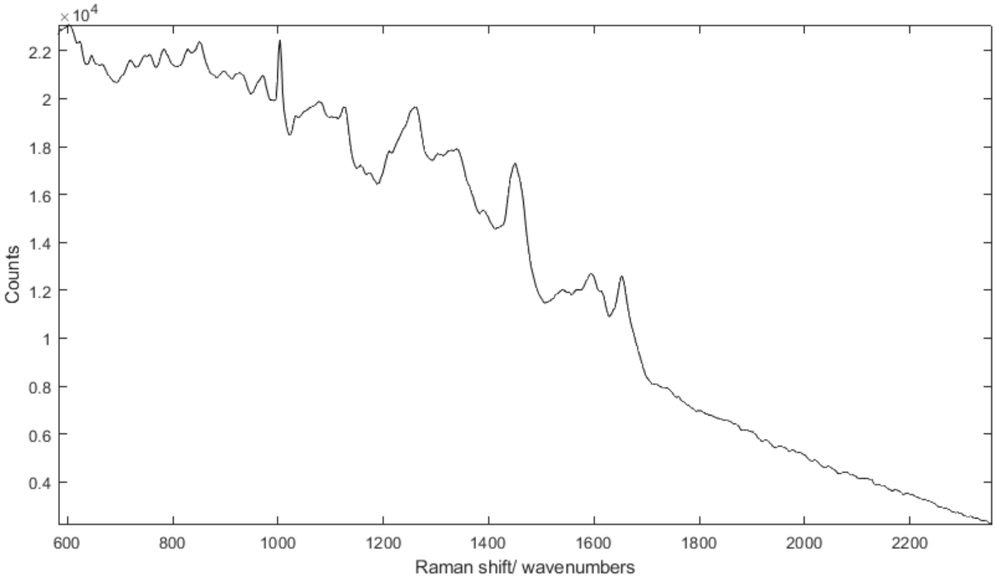

Figure 35: Mean Raman spectrum of rat liver homogenate. Visible are the Raman peaks in the fingerprint region (Shift < 1700 cm^{-1} *and the lack thereof in the silent region above.*

Assumptions of the model

1) The individual sources of light in the sample are independent.
   - This means that laser light that scatters in the sample is never absorbed by the sample to produce autofluorescence, or vice-versa.
2) The primary source of noise is shot noise, due to quantisation of light.
   - There is also an additional source of 'noise' from variance in the spectra from the tissue, as the tissue is not fully homogenous (especially at the length scales used here). This source is not considered in this model.
3) The background and Raman signal from a sample are linearly correlated to the total illumination laser light during the CCD integration.
4) The autofluorescent background and Raman signal from a sample are linearly correlated to the total number of relevant molecules in the sampling volume.

5) The drug concentration is sufficiently low that changing it has a negligible effect on the change in tissue signal due to displacement.

6) The ‘drug signal’ is some linear combination of relevant spectral features from the drug, within the total spectrum acquired. This could be isolated peaks, or shoulder on larger tissue peaks.

7) The ‘dark signal’, a spectrally flat background signal that comes from the CCD, is constant and unaffected by the rest of the light being collected, and unaffected by the integration time of the experiment. The dark signal was measured to be ~1 count/s with a 1 s integration giving ~900 counts of background and a 10 s integration otherwise the same giving ~910 counts. Compared to the signal from all other sources, this can be considered constant.

8) Any background that can be photobleached using the illumination laser has been fully photobleached prior to measurement. This removes the time dependence on the background.

9) Beyond photobleaching, the laser has no chemical effect on the sample.

Sources of noise in the Raman spectrometer

A CCD is a solid-state photodetector, which operates by converting energy from incident photons into electron charges in a pixel. The photon conversion rate is determined by the quantum efficiency of the system, whereas the electron to counts (value recorded) rate depends on the detector readout circuit.

Shot Noise

Raman spectra are acquired in a Raman spectrometer by measuring the light scattered from a sample illuminated by a monochromatic light source. The Raman spectrum is acquired by counting the photons at each energy, or Raman, shift from a bulk sample. As each photon’s scattering is independent of others, and quantised, the spectrum as measured features quantisation, or shot, noise. This noise for a measurement of an average of *N* photons can be characterised as

$$Shot\ Noise = \sqrt{N}. \tag{8}$$

For a system like ours, where the total number of photons counted at each wavelength is of order 10^5, the shot noise will therefore be of order $10^{2.5}$ per readout.

Readout Noise

The amplifier in the CCD detector output introduces noise on every readout. The readout noise depends on the readout rate and the specific detector. For our detectors, the readout noise is of order 5 e^-s per pixel. The sensitivity of the CCD (electron-count conversion rate) is of the same order, so the readout noise is approximately 1 count per pixel.

Dark/ Thermal Noise

Thermal agitation of the charges in the detector causes thermal noise. This type of noise increases exponentially with the temperature of the detector, and linearly with the integration time of the detector. For our CCDs (cooled to -70°C), the dark current is ~1 $e^- s^{-1}$, or approximately 1 count per 5 seconds. As the number of photons being counted is of order $10^5 s^{-1}$, this form of noise is severely limited by the saturation rate of the CCD which occurs within ~10^1 seconds, before the dark current can become important.

Summing spectra together to increase effective well depth

A limiting factor on integration time is the well depth of the CCD, which is the maximum number of electrons that can be held in a well before being measured. It is analogous to the saturation level of the CCD, where any further photons are not measured. For the detectors used, the well depth is of order $10^6 e^-$. To minimise the effects of shot noise, the total number of Raman photons measured must be maximised. If a higher SNR than sqrt(well depth) is required, multiple spectra must be acquired of the same sample, and then summed together. This introduces increased dark current due to the increased integration time, increased readout noise due to the multiple readouts, and increased shot noise.

For a detector with dark current rate *D*, readout noise *R* and with integration time t_{int}, the total noise of *m* summed spectra can be calculated by

$$\boldsymbol{Noise = \sqrt{\sum_i^m (\sqrt{N} + Dt_{int} + R)^2} = \sqrt{m}\sqrt{N + Dt_{int} + R}.} \tag{9}$$

The SNR can then be calculated by

$$\boldsymbol{SNR = \frac{mN}{\sqrt{m}\sqrt{N + Dt_{int} + R}}} \tag{10}$$

This equation is evaluated for our system in Figure 36, where the system is near its saturation limit and the integration times are low.

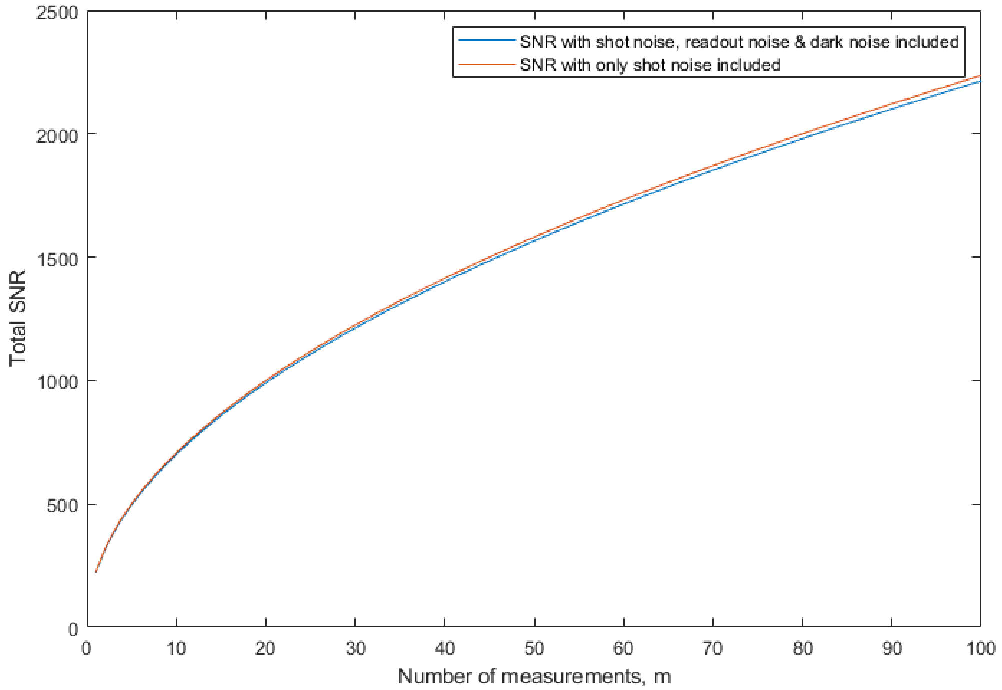

Figure 36: SNR of acquired spectrum as a function of the number of measurements summed together. Assuming each measurement has counts of 50 000, which is approximately 75% of the total well depth of the CCDs being used, and dark noise and readout noise values typical of the systems being used.

For a sample that can saturate the sensor in reasonable times (<~100 s), the dark current and readout noise have a negligible (~1%) change in the total SNR. This means that the SNR of summed spectra matches the theoretical single spectrum measured with the same total integration time in a system with infinite well depth. When a spectral acquisition is not dark-noise limited, summing multiple spectra is therefore a valid method for surpassing the saturation limit.

6.2. Derivation of the prediction model

The minimum detection limit, L_D, of a drug in tissue using Raman spectroscopy can be defined by

$$L_D = w_{min} \tag{11}$$

where w_{min} is the drug concentration at which the *SNR* is higher than 1.65 [114]. The factor of 1.65 is based on the statistical likelihood of overlapping errors during measurements for lower SNR ratios.

$$SNR = \frac{S_{Drug}}{Noise} \tag{12}$$

where S_{Drug} is the signal measured from the drug in the sample, defined fully in the *Signal* section, and *Noise* is the variation in the measured spectrum due to factors other than the drug concentration and the acquisition parameters like laser power or integration time, defined fully in the later *Noise* section 0.

L_D can therefore be calculated using

$$1.65 = \frac{S_{Drug}(L_D)}{Noise}. \tag{13}$$

To predict the SNR of the system for a given drug, drug concentration, and tissue sample, we need to first define the signal, S_{Drug} and the *Noise* of the system.

Drug Signal, S_{Drug}

The drug signal here is defined as some linear sum of *N* distinct spectral features in the Raman spectrum of the drug

$$S_{Drug} = \sum_{i}^{N} R_{Drug}(\nu) \tag{14}$$

where $R_{Drug}(\nu)$ is the Raman spectrum of the drug, which varies with wavenumber ν. R_{Drug} will vary linearly with the laser power P_{Laser}, integration time t_{int}, and drug concentration w, such that

$$R_{Drug}(\nu) \propto P_{Laser} t_{int} w \tag{15}$$

If a reference spectrum, $R_{Drug\_ref}(\nu)$, of the drug is acquired, with known P_{laser_ref}, t_{int_ref}, and w_{ref}, we can use Equations 10 and 11 to predict S_{Drug} for any combination of these parameters:

$$S_{Drug}(w) = \frac{P_{laser} t_{int} w}{P_{laser\_ref} t_{int\_ref} w_{ref}} \sum_{i}^{N} R_{Drug\_ref}(\nu) \tag{16}$$

While ideally P_{laser} and t_{int} would remain constant throughout all experiments, in practice this may result in detector saturation or underutilisation of the dynamic range of the detector, resulting in a higher shot noise contribution. For example, if the reference spectrum was a measurement of pure drug compound (i.e., $w=1$), using standard acquisition parameters for tissue (30 mW@671 nm laser, 10 second integration time) would likely saturate the sensor due to the strong Raman signal from the pure compound. This of course depends on the drug of interest.

S_{Drug} can be calculated using whatever method is preferred, as long as it remains a linear sum. It may be the intensity of the Raman spectrum at a single wavenumber, it may be the area under a specific Raman peak of interest, or the sum of several of these. They can even be weighted separately, depending on the analysis method, in which case the weights $a(\nu)$ would be included in the sum in equation 10. Many multidimensional analysis techniques will weight different areas of the spectrum based on the inputted spectra (in, for example, PCA and PLS), so it is important to include for more complex analysis.

Noise

Here, noise is defined as the standard deviation in the measured spectrum from the sample due to anything other than variation of laser power, acquisition time and drug concentration.

$$Noise(\nu) = \sigma(B_{Tissue}(\nu)) \tag{17}$$

where $B_{\text{Tissue}}(\nu)$ is a set of reference spectra taken from undosed tissue using the same experimental parameters as in the dosed tissue. The noise is calculated separately for each wavenumber, as the contributions to noise from tissue inhomogeneity and from detector noise vary with wavenumber.

The two primary sources of noise are spectral variation due to the inhomogeneity of the tissue and shot noise from the detection pathway of the spectrometer. While the shot noise component can be modelled analytically, the tissue inhomogeneity component cannot. Since neither are significantly affected by the drug signal (See section 0), they can be computed using data from reference tissue spectra measured on the same spectrometer. Assuming that these reference spectra are acquired using the same acquisition parameters (integration time, CCD settings, laser power), the variation in the reference spectra should be representative of the variation (noise) in the spectra from a sample that has been dosed with the drug of interest.

Shot Noise

The shot noise component of the noise is a function of the sum of all of the components of measured light in the spectrum $P_{Total}(\nu)$, described as

$$P_{Total}(\nu) = R_{Drug}(\nu) + B_{Tissue}(\nu) + D(\nu) \tag{18}$$

where $D(\nu)$ is the dark current measured in the system. Shot noise is proportional to the square root of the total signal measured,

$$Shot(\nu) \propto \sqrt{R_{Drug}(\nu) + B_{Tissue}(\nu) + D(\nu)} \tag{19}$$

At around the detection limit drug concentration, $R_{Drug}(\nu)$ will by definition be similar in size to the total noise of the system. As such, it will be much lower than $B_{Tissue}(\nu)$. Similarly, in experiments to measure the detection limit of Raman spectroscopy, the full dynamic range of the detector should be used. The Dark current is very low compared to the saturation limit of the detectors used, and as such is very low compared to B_{Tissue}. These factors result in the shot noise being overwhelmingly dominated by light from B_{Tissue}. As such, the contributions to shot noise from the drug signal and the dark current are ignored in this prediction model.

Detection Limit

With our definitions of Signal as a function of drug concentration, and Noise from the tissue, we can combine Equations 12 and 13 to acquire a more analytical formulation for SNR:

$$SNR(\nu) = \frac{P_{laser} t_{int} w}{P_{laser\_ref} t_{int\_ref} w_{ref}} \frac{R_{Drug\_ref}(\nu)}{\sigma(B_{Tissue}(\nu))} \tag{20}$$

This equation is for evaluating the SNR for a drug at concentration w in tissue at wavenumber ν. The signal from the drug at multiple wavenumbers can be combined, with the errors added in quadrature, such that

$$SNR = \frac{P_{laser} t_{int} w}{P_{laser\_ref} t_{int\_ref} w_{ref}} \frac{\sum_i^N R_{Drug\_ref}(\nu)}{\sqrt{\sum_i^N (\sigma(B_{Tissue}(\nu))^2)}} \tag{21}$$

This equation can be used to predict the SNR at a given w. To instead predict L_D, we can set SNR to 1.65, w for L_D, and rearrange to solve for L_D:

$$L_D = \frac{1.65 P_{laser\_ref} t_{int\_ref} w_{ref}}{P_{laser} t_{int}} \frac{\sqrt{\sum_i^N (\sigma(B_{Tissue}(\nu))^2)}}{\sum_i^N R_{Drug\_ref}(\nu)} \tag{22}$$

At large concentrations (B_{Tissue} not >> R_{Drug}), the SNR as calculated in Equation 17 will also become less accurate, as noise contributions from the signal from the drug become more important.

6.3. Worked Example

In this section, the limits of detection for drugs in brain and liver tissue mimetic models used in this study were determined using equation (22). For the deuterated compound GSK1 mixed in homogenised liver tissue (homogenate cryosectioned to 16 µm thick) the Raman spectrum was acquired with the 785 nm laser Raman spectrometer. $R_{Drug}(v)$ was acquired by measuring the Raman spectrum of a small crystal of GSK1 ($w_{ref}=1$) with a 785 nm laser at $P_{laser\_ref} = 100\ mW$ and $t_{int\_ref} = 1\ s$. 200 spectra of the undosed liver were measured to acquire $B_{Tissue}(v)$, using $P_{laser} = 150\ mW$ and $t_{int} = 10\ s$. Each point in the liver was bleached for 10 s prior to spectral acquisition, to minimise the fluorescent background in the acquired spectrum.

As the acquisition parameters between R_{Drug} and B_{Tissue} are different, the scaling parameters in Equation 12 must be used. The scaling is shown in Figure 37.

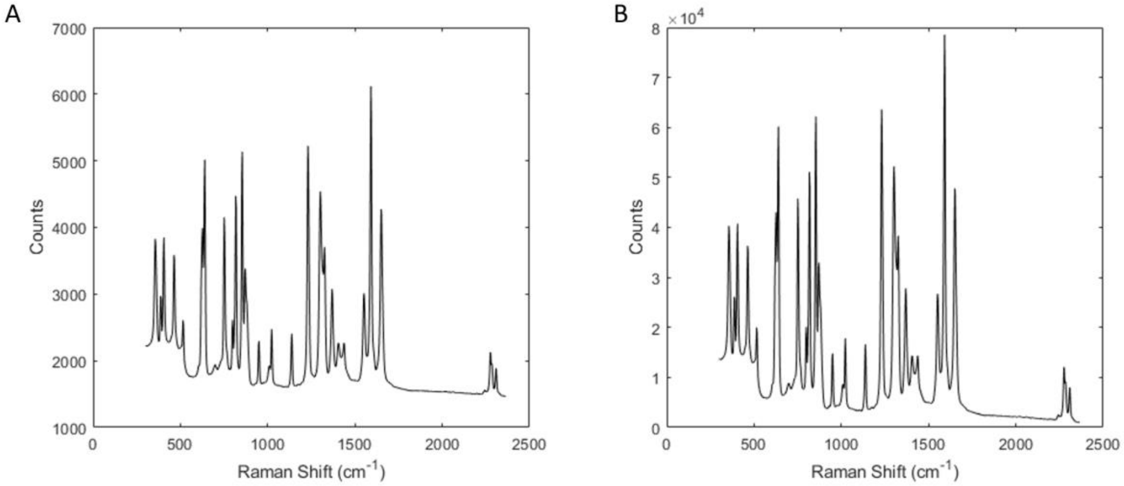

Figure 37: Raman spectrum of GSK1. A) Raman spectrum as measured. B) Raman Spectrum after being scaled to the acquisition parameters of the reference liver spectra, using the scaling from Equation 12. The only change is in the counts (y axis), the shape of the spectrum is unchanged. The saturation limit of the spectrometer used is 65535 counts, so using the same acquisition parameters would have resulted in detector saturation.

With R_{Drug} scaled by its concentration, the noise, as defined in Equation 13, is required. Its evaluation is shown in Figure 38.

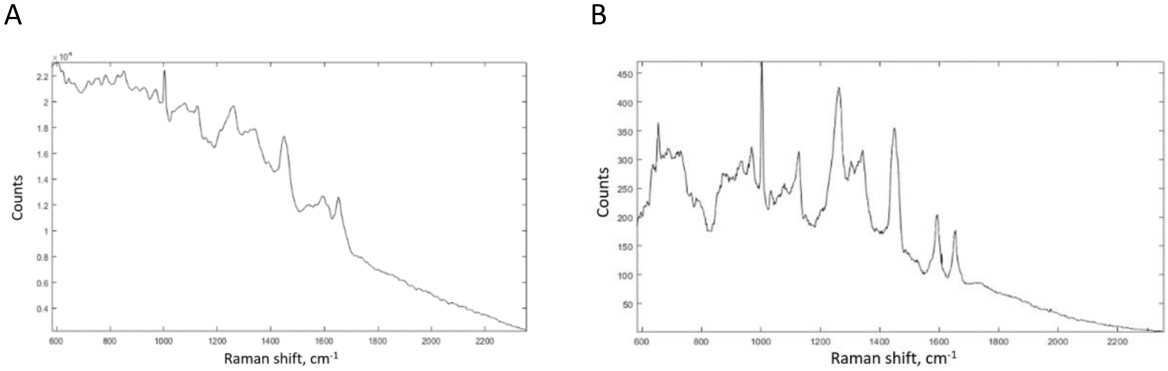

Figure 38: Calculation of the predicted noise of the system. A) Mean spectrum acquired from undosed liver dataset, N=200. B) Standard deviation of the full liver dataset, calculated individually for each wavenumber as in Equation 13.

Calculating the minimum detection concentration L_D for single-wavenumber calculations is then simply a case of multiplying the element –by element division of the noise spectrum by the scaled drug spectrum by 1.65, or

$$L_D(\nu) = 1.65 \frac{Noise(\nu)}{R_{Drug\_scaled}(\nu)} \tag{23}$$

This is shown in Figure 39, where the L_D spectrum is essentially the division of Figure 38B by Figure 37B. We can see that, despite not being the strongest peaks, the silent region features of the drug spectrum exhibit the highest SNR and thus lowest detection limit. In addition, regions where the drug spectrum have no features still have minimum detectable concentrations. This is due to the nonzero background from GSK1 being considered signal. In practice, discrimination of background from drugs and background from the tissue would be essentially impossible.

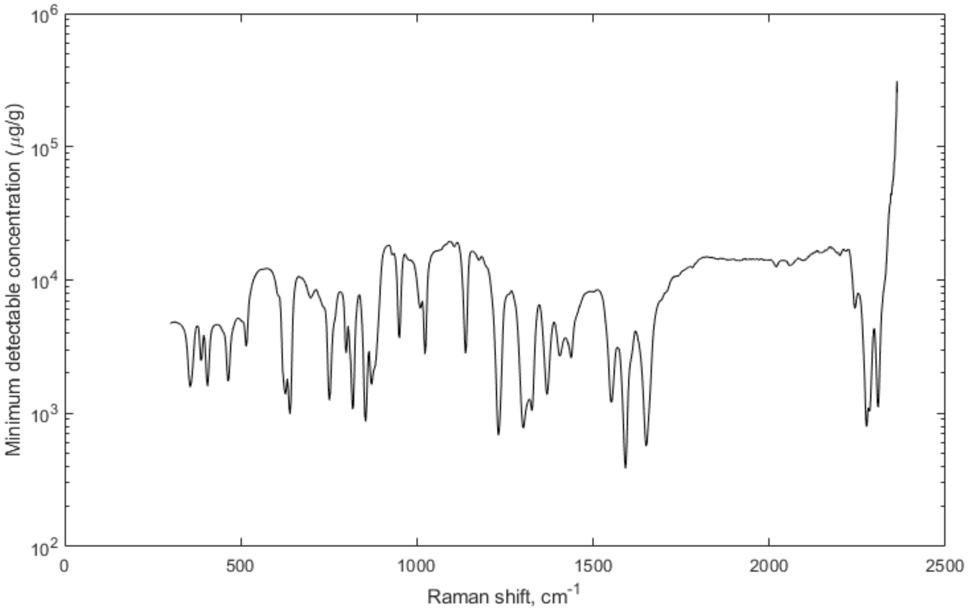

Figure 39: Predicted detection limit of drug peaks at each wavenumber.

The resultant detection limit spectrum is only applicable to the specific drug/tissue combination used, along with the specific instrument used. It can, however, be easily generated for any drug/tissue/instrument combo using only a reference drug spectrum and tissue spectrum set from the instrument of interest. The spectrum shows that the single-wavenumber detection limit is 386 µg/g, using the 1591 cm^{-1} part of the spectrum. To calculate the detection limit for multi-wavenumber combination, Equation 18 can be used.

6.4. Predictions for all drugs investigated

For the mimetic model study, we measured the Raman spectra of 8 drugs, and the Raman spectra of 2 tissues: Brain and liver. These were repeated using 671 nm and 785 nm illumination wavelengths to calculate the detection limit concentrations of these drugs in different tissues and spectrometers. The results are tabulated in the tables below.

Table 1: Detection limits of deuterated drugs in brain – 785 nm illumination

Drug Name	Single Wavenumber Detection limit (µg/g)	Wavenumber (cm^{-1})	Multi-wavenumber detection limit (µg/g)
GSK1	386	1591	133
GSK2	4547	2154	501
GSK4	282	2220	108
GSK10	2190	1630	613
GSK13	2643	1619	728
GSK48	304	1564	34
GSK48 (Background removed first)	482	1564	116
GSK49	4223	2100	716
GSK50	803	1540	227

Table 2: Detection limits of deuterated drugs in liver – 785 nm illumination

Drug Name	Single Wavenumber Detection limit (µg/g)	Wavenumber (cm^{-1})	Multi-wavenumber detection limit (µg/g)
GSK1	546	1591	242
GSK2	6773	2151	1382
GSK4	445	2220	169
GSK10	1566	1631	905
GSK13	1800	1618	839
GSK48	169	1564	37.8
GSK48 (Background removed first)	271	1564	221
GSK49	5157	730	1457
GSK50	492	1541	259

Table 3: Detection limits of deuterated drugs in liver – 671 nm illumination

Drug Name	Single Wavenumber Detection limit (µg/g)	Wavenumber (cm^{-1})	Multi-wavenumber Detection limit (10 minutes bleaching) (µg/g)
GSK1	9941	1591	3692
GSK2	55192	1247	26841
GSK4	39883	2220	17365
GSK10	31773	1638	8745
GSK13	10860	1323	3387
GSK48	5220	1570	2973
GSK48 (Background removed first)	52501	1647	35213
GSK49	76005	3069	25420
GSK50	29926	1546	21302

Table 4: Detection limits of deuterated drugs in brain – 671 nm illumination.

Drug Name	Single Wavenumber Detection limit (10 s bleaching) (µg/g)	Wavenumber (cm^{-1})	Multi-wavenumber Detection limit (µg/g)	Single Wavenumber Detection limit (10 minutes bleaching) (µg/g)*
GSK1	3021	1591	1124	943
GSK2	15069	1247	6845	4566
GSK4	11894	2220	5440	3555
GSK10	8779	1638	3026	2690
GSK13	3127	1323	1698	908
GSK48	1499	1647	875	469
GSK48 (Background removed first)	2082	1647	1123	683
GSK49	24144	3069	8574	8414
GSK50	8788	1546	5169	2600

* The background reduction in brain tissue using the 671 nm Raman spectrometer was found to continue for ~10x longer than in the 785 nm spectrometer, possibly due to the increased number of fluorophores excitable by 671 as compared to 785 nm[54]. To take this into consideration, the predictions were also performed using tissue spectra from tissue that had been photobleached for 10 minutes.

6.5. Discussion

The predictions with the lowest detection limits were those of GSK1, GSK4 and GSK48. GSK4 was the only drug of these three that predicted a silent-region peak to be easiest to detect. This was likely due to the alkyne peak being stronger by a factor of ~4 than the deuterated peaks. Additionally, the peaks from GSK1 and GSK48 that were predicted as easiest to detect were in the upper end of the fingerprint region, where the fluorescent background is suppressed but the detection isn't reliant on deuterated bonds. These all had predicted detection limits below 200 µg/g, which is in the range of pharmacological relevance in average dosage for some drugs[97]. The overall dose given depends highly on the specific drug, as low as 1 ng/g to upwards of 1 mg/g. Using this range, any predicted detection limit over 1 mg/g (1000 µg/g) is unlikely to be of great use.

When comparing the Raman instruments, there are three main differences between the acquisition of spectra using 671 nm and 785 nm illumination in these experiments:

The first is the sensitivity of the spectrometers to different wavelengths. The Raman spectrum is offset from the illumination wavelength, so a shorter illumination wavelength results in a Raman spectrum composed of shorter wavelengths. The CCD arrays used in these experiments are less sensitive to NIR photons than red photons, so the higher wavenumber peaks of the Raman spectra are detected less strongly at 785 nm illumination. As a result, the detection limits of higher wavenumbers are relatively improved for 785 nm illumination wavelength For example, an alkyne peak at 2220 cm^{-1} would be detected with a quantum efficiency of approximately 55%, whereas the same peak measured with a 671 nm illumination wavelength has a quantum efficiency of approximately 95%.

The second is the behaviour of the tissue background to different illumination wavelengths. 671 nm illumination causes more autofluorescence than 785 nm. This also changes the relative strengths of different wavenumbers for drug detection, as the autofluorescence spectrum is not uniform across the spectrum. It also heavily affects the total noise level, explaining the much higher detection limit concentrations using 671 nm compared to 785 nm.

The third is the variation in Raman scattering coefficient with illumination wavelength. The Raman spectrum from all sources should increase as the illumination wavelength decreases. In practice, as the spectrometers have different detection pathways, the actual relative performance of the two wavelengths in the above experiments is less simple to predict. For this, the reference spectra are used instead.

These are all important considerations to consider when choosing a drug/tissue/laser combination for detection limit experiments. In the samples measured, however, the 785 nm laser performs better across the board, with detection limits much lower than the corresponding limits from 671 nm.

There is potential for the drugs in brain to be measurable at useful concentrations with 671 nm by first using prolonged photobleaching. It will likely still be less sensitive than the 785 nm system, but considering it requires no extra samples, is simple to test. For drugs that exhibit features in the long wavenumber region, where 785 nm is severely hindered by the quantum efficiency of detectors in the >1000 nm range, 671 nm could have a better detection limit. Further comparisons of SNR between 671 nm and 785 nm are made in section 7.3.

7. Quantification of drugs in brain and liver mimetic tissue models using Raman spectroscopy

7.1. Introduction

Mimetic tissue models, as described in Chapter 4.9, are drug-tissue models produced by homogenising a known mass of control tissue with a known mass of drug to produce a tissue model with known drug concentration and no tissue heterogeneity. This chapter describes the experiments and results performed with the mimetic models that were jointly produced by myself, Jan Majer, and Peter Marshall, both at GlaxoSmithKline.

The acquisition of new tissue models after the construction and characterisation of the 671 nm system, which was completed in parallel with the prediction model due to temporary laser failure of the 785 nm system, allowed for direct comparison of the two systems for drug detection in tissue.

The goal of these experiments were to evaluate the quantifiability of drug detection in tissue models using Raman spectroscopy, and to verify the results by calculating quantification curves for the same models with MALDI-TOF MSI performed at GlaxoSmithKline.

7.2. Materials and Methods

The 671 nm Raman microscope was set to illuminate the sample with 30 mW, the highest power that could reliably be used without thermal damage to the samples in the silent region.

The 785 nm Raman microscope was set to illuminate the sample with 200 mW for the same reason.

Samples

Drugs

Four drugs were chosen for this study and integrated into mimetic tissue models (chemical formulae presented in Figure 40). Ponatinib is a tyrosine-kinase inhibitor used in the treatment of leukaemia. GSK4X is a small molecule originally designed to inhibit activity of H1 receptors. Both molecules were chosen due to their alkyne bonds, expected to produce a strong band in the Raman silent region. GSK4 is a deuterated form of GSK4X. This molecule has been chosen due to it containing two different molecular bonds exhibiting Raman-silent region peaks: the alkyne bond and the C-D bonds present due to its deuteration. These two drugs when compared can show the potential benefits of deuteration on the limit of detection of Raman spectroscopy. Acetaminophen is a commonly available analgesic. We investigated deuterated acetaminophen to evaluate the efficacy of Raman spectroscopy in detecting molecules with C-D bonds in tissue, in the absence of an alkyne bond. While the conclusions of the previous chapter pointed towards the use of GSK48, there were supply issues of the deuterated drugs prior to generation of the mimetic models, so ponatinib was substituted due to its alkyne bond and detectability in MALDI experiments previously performed by GlaxoSmithKline.

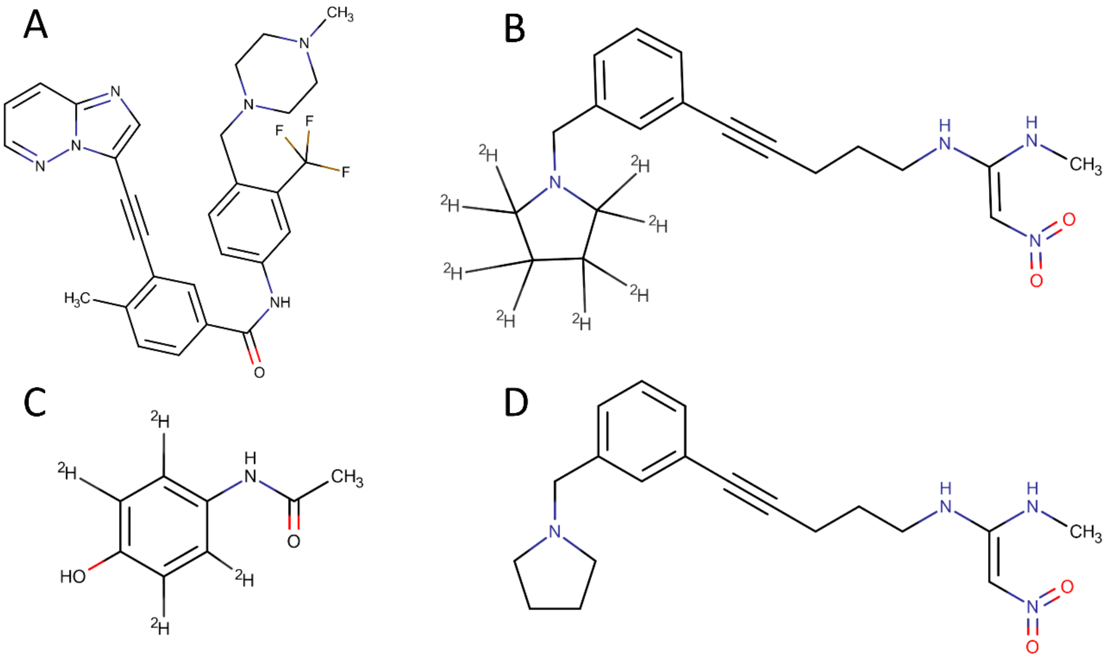

Figure 40: Molecular structures of drugs used in mimetic tissue models. A) ponatinib; B) GSK4; C) acetaminophen; D) GSK4x

Mimetic tissue model preparation

For this study, mimetic tissue models were produced at 0, 0.5, 1, 5, 10, 20, 35, 50, 100, 200, 300, 400, and 500 µg/g drug/tissue mass ratio. These were made for all four of the drugs investigated, using rat brain and rat liver tissues. The models were frozen, cryosectioned at a thickness of 16 µm and thaw-mounted onto fused quartz microscope slides (UGQ, UK) for Raman measurements and ITO-doped slides for MALDI MSI measurements (Alpha Industries, USA).

Matrix-assisted laser desorption/ ionization (MALDI) spectrometry

Matrix solution was prepared by dissolution by sonification of α-Cyano-4-hydroxycinnamic acid(αCHCA, Bruker Daltonics, Germany) in 0.1% solution of trifluoric acid (TFA) in 70% EtOH to a final concentration of 7mg/mL.

αCHCA matrix was deposited onto the sample by the automated TM-Sprayer (HTX Technologies, USA). The automated sprayer was set to spray at 70 °C, and at matrix flow rate of 0.12 mL/min. Spraying nozzle was traversing at speed of 900 mm/min 40 mm above the sample with gas flow under pressure of 10 PSI. Spacing was set to 3mm and the total number of passes was set to 8.

MALDI MSI of mimetic tissue models was performed using Ultraflextreme II (Bruker Daltonics, Germany). The instrument was operated with flexControl software v3.4 (Bruker Daltonics, Germany). Samples were ionised using 355 nm smartbeam-II Nd-YAG laser. 400 laser shots were fired at 1 kHz frequency per raster spot (raster size = 200×200 μm). Analyser was set to positive-charged reflectron mode. Fragmentation (MS/MS) analysis was performed in LIFT mode with precursor ion selector (PCIS) range set to ± 2 Da. Sampling rate was set to 0.63 GS/s. Reflector voltage was set to 2.85 kV, ion source 1 and 2 voltages were set to 7.5 kV and 6.65 kV, respectively. Lens voltage was 3.9 kV, reflector 1 and 2 were set to 29.5 kV and 14 kV, respectively. LIFT 1 and 2 were set to 19 kV and 4.2 kV voltages, respectively. Peak detection algorithm was selected to Centroid with TopHat baseline subtraction method. Imaging experiments were created and visualized in flexImaging software (Bruker Daltonics, Germany).

Raman spectroscopy measurements

Raman spectra of the pure drugs were measured by depositing small crystals of the drug onto fused quartz slides. To produce one Raman spectrum of each drug, several spectra acquired from approximately equally sized crystals of each drug were measured. The integration time of 0.1 s/spectrum was chosen to avoid saturation of the detector. These measurements were taken on both the 671 nm and the 785 nm Raman microscopes.

Raman spectra of the mimetic tissue samples were collected with a 10 s laser dwell time per point prior to measurement for photobleaching most of the fluorescent background. After photobleaching, Raman spectra were acquired with 10 s integration for brain samples and 5 s integration for liver samples. These times were chosen to reliably maximize the signal in individual spectra without saturation of the detector. The higher autofluorescence of liver necessitated a lower integration time for this reason. For longer overall acquisition times, repeat measurements of Raman spectra at the same positions in the sample were recorded and then averaged. Due to the high well depth and low readout noise of the CCDs operating in Single-Track mode, the noise added into the measurements by summing sequential spectra was negligible relative to the shot noise from the background autofluorescence when the integration times are set to maximize use of the dynamic range of the CCDs. To record the fingerprint region of the tissue and the silent region peaks of the drugs, the spectral range chosen was 900-2400 cm^{-1} (avoiding quartz Raman bands below 900 cm^{-1}). The spectral resolution of the systems in this range was 3 cm^{-1}. To minimize potential tissue degradation during measurement, the 785 nm instrument was fitted with a cooled stage maintained at 8°C during the long limit of detection measurements. This was found to be the lowest temperature that the samples could be kept at without risking water condensation build-up around the optics.

Detection limit measurements

For measuring the limit of detection of drugs in tissue, three randomly sampled locations in each concentration of each mimetic tissue model were measured to assess the detection limit of each mimetic tissue model and the variability in the samples. The total acquisition time for each location depended on the concentration of drug in the mimetic tissue model. At 100, 200, 300, 400, 500 µg/g, the measurement times were 60 minutes, 30 minutes, 15 minutes, 10 minutes, and 5 minutes, respectively. At all concentrations below 100 µg/g, the acquisition time used was 120 minutes.

Detection limit predictions

Using the same model as was described in Chapter 6, and the measurement parameters and data analysis used here, the predictions for the detection limits were calculated and are shown in Table 5 and Table 6. These numbers vary from the values for the same samples in the previous chapter due to the changes in acquisition time and a slight variation in the noise level due to different reference tissue samples being measured. Additionally, they use the area-under-peak summation of signal, so the number of samples being measured is greater than one (the bands being measured in this study typically had widths of around 6-10 pixels on the CCD).

Drug name	Detected wavenumber (cm^{-1})	Detection limit with 785 nm laser (μg/g)	Detection limit with 671 nm laser (μg/g)
Ponatinib	2220	49	530
GSK1/ acetaminophen	2276	154	1463
GSK4	2236	216	2247
GSK4x	2236	80	917

Table 5: Predicted detection limits and the optimal wavenumbers for detection for the measured drugs in brain mimetic tissue models.

Drug name	Detected wavenumber (cm^{-1})	Detection limit with 785 nm laser (μg/g)	Detection limit with 671 nm laser (μg/g)
Ponatinib	2220	75	1591
GSK1/ acetaminophen	2276	239	6930
GSK4	2236	311	8422
GSK4x	2236	123	3468

Table 6: Predicted detection limits and the optimal wavenumbers for detection for the measured drugs in liver mimetic tissue models.

Spectral analysis

Spectral subtraction and normalization

To account for variance in the thickness of the tissue samples, spectra were normalized by scaling the silent region 1800 cm^{-1} to 2150 cm^{-1} of the drugged samples to that of a reference 0 µg/g measurement. This region is invariant between samples other than absolute magnitude, so acts as a reference point to scale Raman signal with. The 0 µg/g spectrum was then subtracted from the spectra, removing the autofluorescent background and most of the reproducible interference pattern from the silent region. This interference pattern, being an artefact of the CCD, was almost identical in each measurement and as such can generally be eliminated through background subtraction.

Limit of Detection

The limit of detection is the lowest drug concentration that can be quantitatively measured. The signal measured from a region of tissue with a lower drug concentration is not statistically discriminable from the signal measured from a region of tissue with 0 drug concentration and is therefore indistinguishable from undosed tissue.

The limit of detection of the system is dependent on the drug of interest, the tissue of interest, and the integration time used. This is because the limit of detection[28] is reached when the standard deviation in the measured signal from a non-drugged (blank) mimetic tissue model, σ_{blank}, and the standard deviation in the measured signal from a drugged mimetic tissue model, σ_{lim}, reach an overlap described by

$$\boldsymbol{\mu_{blank} + 1.645\sigma_{blank} = \mu_{lim} - 1.645\sigma_{lim},} \tag{24}$$

where μ_{lim} and μ_{blank} are the average signals measured from the detection-limited mimetic tissue model and the non-drugged mimetic tissue model respectively. The limit of detection can be approximated for a certain integration time using the mimetic tissue models described here by finding the lowest concentration in the mimetic tissue model where this relation ((24)) holds true. As the signal measured is proportional to the concentration of the drug, this limit can be interpolated between the lowest concentration measured and the highest concentration not measured to approximate the actual detection limit.

7.3. Results and Discussion

Mitigation of tissue autofluorescence background and laser wavelength selection

Tissue background fluorescence was minimized by sectioning the tissue at approximately the same thickness as the depth of focus of the microscopes (~16 µm). This enabled the system to have the maximum Raman spectral sensitivity while minimizing the presence of out-of-focus tissue that contributes high autofluorescence when attempting bulk tissue measurements. Due to the long measurement times and high laser powers used in this study, photobleaching occurred naturally by the illumination laser.

Near-infrared lasers (e.g., 785 nm wavelength) are commonly used in Raman spectroscopy for biological materials to reduce fluorescent background. However, the quantum efficiency of CCD detectors falls off rapidly above around 900 nm, which corresponds to around 1620 cm^{-1} Raman shift for 785 nm excitation. As a result, the Raman signal intensity in the silent region (1800-2800 cm^{-1}) is reduced relative to the fingerprint region (800-1800 cm^{-1}). With a 785 nm system the quantum efficiency at 2220 cm^{-1}, the location of one of the drug peaks detected in this study, is around 60%, relative to >80% for the fingerprint region. Using a 671 nm laser for excitation solves this issue by shifting all the measured wavelengths lower, into the spectral range where the CCD is most efficient. The resultant quantum efficiency of the system at 2220 cm^{-1} is > 90%, a ~ 50% relative improvement in signal sensitivity over a 785 nm system. This combined with the higher scattering cross section of 671 nm results in a theoretical 2.8-fold increase in detected Raman photons relative to 785 nm, for a Raman band at 2200 cm^{-1}. Thus, to improve the detection limit of drugs in tissue, the increased autofluorescent background must not be higher by the same factor, or the signal-to-noise ratio of the system will be inferior. To compare the two wavelengths, the ponatinib mimetic tissue models of both brain and liver at 0, 100 and 500 µg/g were measured using both the 671 nm and 785 nm Raman instruments. Ponatinib drug was chosen due to it having the strongest measured signal of the mimetic tissue models produced. The acquisition times were the same for both instruments (5 minutes for each point, but the laser powers were different (listed in the instrumentation section) due to limitations of possible laser damage to the samples.

Figure 41 compares Raman spectra measured using 671 nm and 785 nm excitation wavelengths of ponatinib in brain and liver tissue. The range of the spectrum below 1800 cm^{-1} is the fingerprint region of the Raman spectrum. The peaks in this range can be attributed to the pyrimidine group, the phenyl rings and the trifluoromethyl group in the molecule, along with an alkyne peak at ~ 1600 cm^{-1}. While the 2220 cm^{-1} peak of ponatinib is more intense than the bands in the fingerprint region using the 671 nm laser (Figure 41Ai) compared to those using the 785 nm laser (Figure 41Aii), the 671 nm also induces a higher autofluorescence. This auto-fluorescence background increases the noise of the measurements in the mimetic tissue models on top of the noise from the tissue itself. For tissue (Figure 41B), the visible bands in these spectra include the phenylalanine peak at 1001 cm^{-1}, amide III bands in the 1200 – 1300 cm^{-1} range, the CH_2 bend in proteins and lipids at 1450 cm^{-1}, and the amide I peak at 1660 cm^{-1}. Different concentrations of these biomolecules cause the difference in the strength of these peaks between brain and liver. These Raman peaks present in the tissue overlap with the peaks in the drug spectra, making discrimination difficult.

The inset plots of background-subtracted spectra in Figure 41B and C are magnified to show the strength of the 2220 cm^{-1} Raman peaks relative to the noise in the spectra. The noise, which is primarily shot noise from the autofluorescent background of the tissue, is proportional to the square root of the total signal measured. As a result, a higher background level increases the noise in the measured spectra. Figure 41 shows that tissue background in the silent region from brain is slightly higher using 671 nm compared to 785 nm, but much higher, by a factor of ~4, for liver.

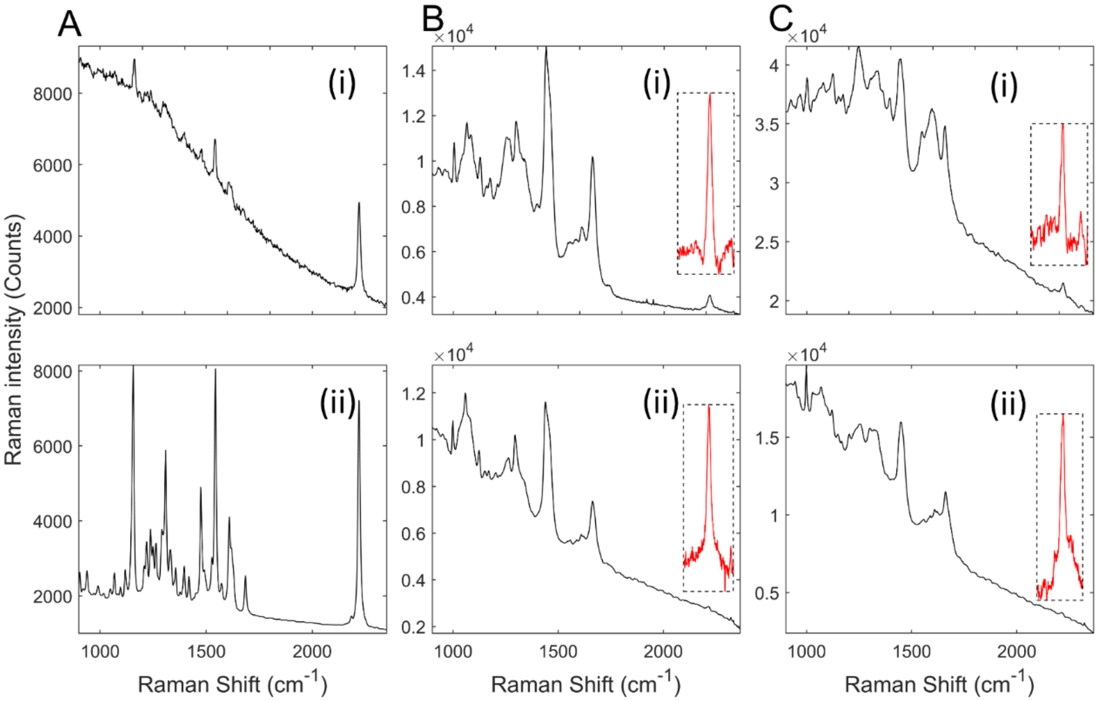

Figure 41: Comparison of Raman spectra of ponatinib and mimetic tissue models (brain and liver) measured using 671 nm and 785 nm excitation wavelengths. A: Raman spectra of crystalline ponatinib: 671 nm (i) and 785 nm (ii) (integration time: 0.1 s). B: Raman spectrum of 500 µg/g ponatinib/brain mimetic tissue model measured using 671 nm (i) 785 nm (ii) (integration time: averages of 30 spectra each, 10 s/spectrum). Inset in box, 2220 cm^{-1} peak after subtraction of Raman spectrum of pure tissue, magnified to show noise levels. C: Raman spectrum of 500 µg/g ponatinib/liver mimetic tissue model measured using 671 nm (i) and 785 nm (ii) (integration time: average 60 spectra at 5 s/spectrum). Inset in box, 2220 cm^{-1} peak after pure tissue subtraction, magnified to show noise levels.

Signal-to-noise ratio (SNR) was calculated here as the area under the 2220 cm^{-1} peak (signal) divided by the standard deviation of the background-subtracted spectrum in a flat part of the silent region (noise). When the background was subtracted, this region is flat and mostly constant across a given tissue type. For the ponatinib/ rat brain mimetic tissue model at 500 µg/g, the SNR was ~650 for the 671 nm system and 1100 for the 785 nm system. Therefore, 785 nm could produce ~1.7-fold higher SNR and a had a detection limit ~0.6-fold smaller than that of 671 nm. For the ponatinib/ rat liver mimetic tissue model at 500 µg/g, the SNR was ~260 for the 671 nm system and ~950 for the 785 nm system. Therefore, 785 nm could produce ~3.7x the SNR and a detection limit ~0.27x that of 671 nm. These results show that, especially for highly fluorescent tissues like liver, 785 nm was more effective in detecting the drug based on Raman bands in the silent region, despite the fact that the quantum efficiency of the detector in this spectral region was lower. The same was true for less fluorescent tissues like brain, but the difference was less extreme and other factors may be considered before choosing which wavelength to use. As a result of these tests, full scale measurements on the mimetic tissue models were only performed on using the 785 nm system.

Raman spectra of pure drugs

The spectra of the pure drugs are shown in Figure 42:. Ponatinib exhibited a strong Raman peak in the silent region, at 2220 cm^{-1} assigned to the alkyne bond present in the molecule. This peak also had a weak shoulder on the lower wavenumber side at around 2180 cm^{-1}, also a result of the alkyne bond, which is visible in Figure 42a(ii). GSK4 exhibited several Raman peaks in the silent region, at 2031 cm^{-1}, 2118 cm^{-1}, 2159 cm^{-1}, and 2236 cm^{-1}, as shown in Figure 42b(ii). The 2236 cm^{-1} peak is a feature from the alkyne bond in the molecule, while the others are a feature of the C-D bonds in the molecule. GSK4x exhibited a single Raman peak in the silent region, at 2236 cm^{-1}, as shown in Figure 42c(ii). This peak, as in GSK4, was attributed to the alkyne bond in the molecule. Deuterated acetaminophen exhibited 2 weak Raman peaks int the silent region, at 2276cm^{-1} and 2309cm^{-1}. These were both attributed to the C-D bonds present in the molecule.

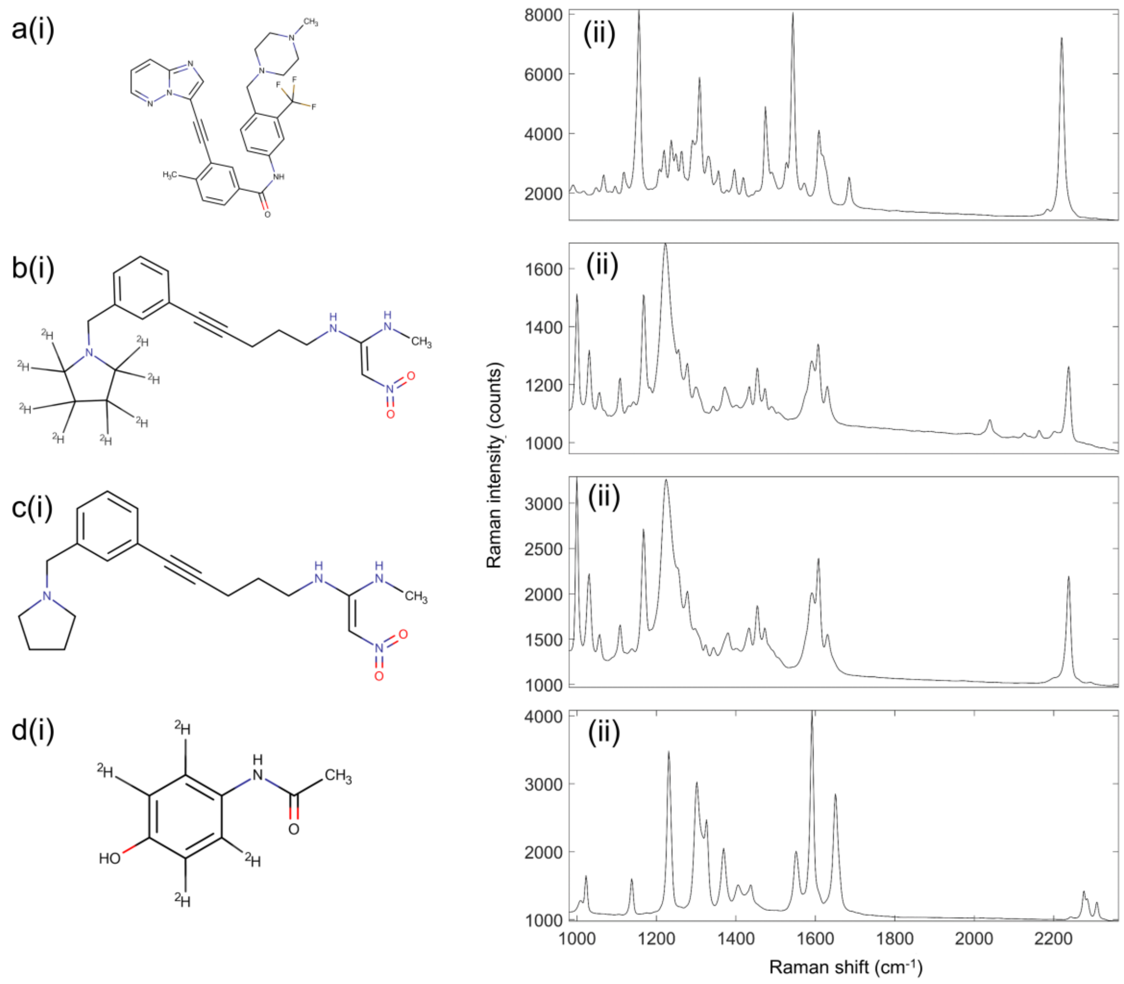

Figure 42: Molecular structures and 785 nm excitation Raman spectra of drugs used in this study. (a): (i) structure and (ii) Raman spectrum of ponatinib. (b): (i) structure and (ii) Raman spectrum of GSK4. (c): (i) structure and (ii) Raman spectrum of GSK4x. (d): (i) structure and (ii) Raman spectrum of acetaminophen.

Ponatinib in brain mimetic tissue model

The Raman spectra for the ponatinib in brain mimetic model are shown in Figure 43. The 2220 cm-1 peak, after tissue spectrum subtraction, was visible in the spectra of drugged mimetic tissue models at higher concentrations Figure 43(b). Because the spectra were normalized to total integration time and to the pure reference tissue mimetic model spectrum of each sample, the strength of the peaks can be compared directly for developing quantitative models. The lowest concentration with a visible Raman peak at

2220 cm-1 measured was 35 µg/g, and the lowest concentration with a significant measured signal (area under peak), as defined in Equation 1, was 20 µg/g. The quantification curve had a gradient of 7.68 counts/(µg/g), with r=0.95. The limit of detection was 18±5 µg/g.

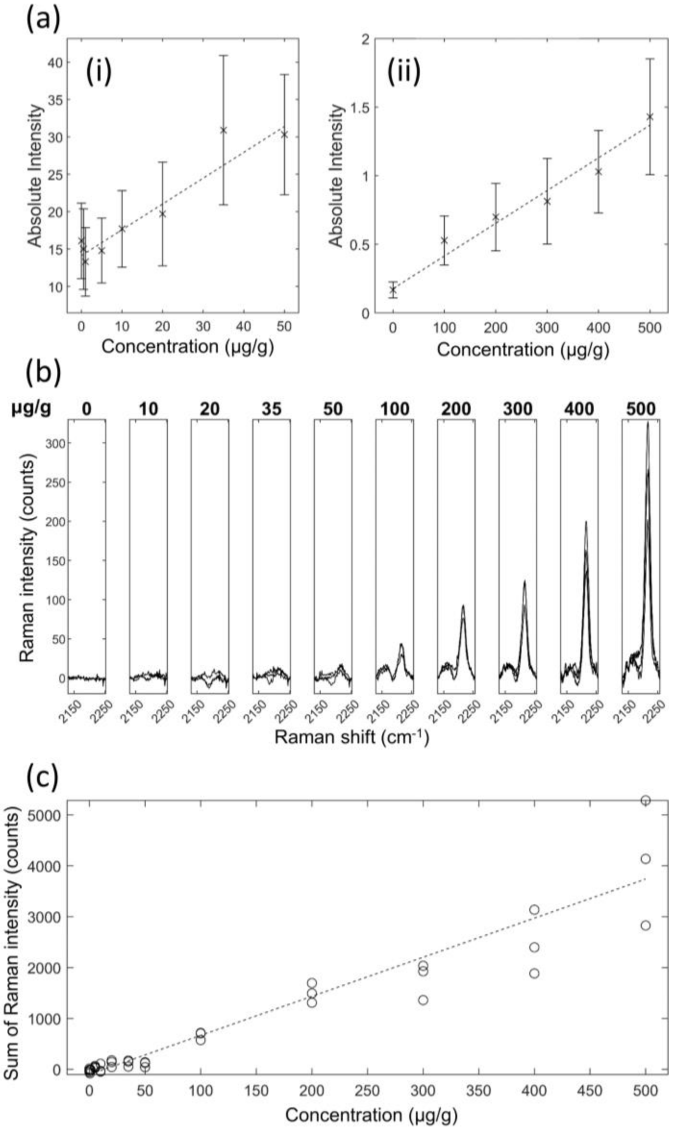

Figure 43: Ponatinib in rat brain mimetic tissue model. a(i): Weighted regression fit of MALDI-intensity of 183.56 Da mass peak for 0 – 50 µg/g mimetic tissue model (dotted line), mean measured signal at given concentration and standard deviation (crosses and bars). a(ii): Weighted regression fit of MALDI-intensity of 183.56 Da mass peak for 0 –

500 µg/g mimetic tissue model. (b): Integration time-normalized 2220 cm^{-1} peak in mimetic tissue models. Three randomly sampled locations of each mimetic tissue model were measured for each concentration. (c): Linear regression fit of sum of signal under 2220 cm-1 peak at given concentration (dotted line), measured signal under peak at given concentration for each sample (circles).

Ponatinib in liver mimetic tissue model

The results for ponatinib in liver are shown in Figure 44. The 2220 cm^{-1} peak and 2180 cm^{-1} shoulder were visible after baseline subtraction in the spectra of drugged mimetic tissue models at higher concentrations (Figure 44B). They were sufficiently strong at 500 µg/g concentration to be visible above in the non-baseline subtracted spectrum, as is shown in the inset box in Figure 44A(ii). Because the spectra were normalized to total integration time and to the pure reference tissue mimetic model spectrum of each sample, the strength of the peaks can be compared directly to make quantitative predictions. The minimum concentration with a visible Raman peak at 2220 cm^{-1} measured was 50 µg/g, and the minimum concentration with a significant measured signal was 35 µg/g at the integration time used. The quantification curve had a gradient of 6.48 counts/(µg/g), with r=0.95. The limit of detection was 34±6 µg/g.

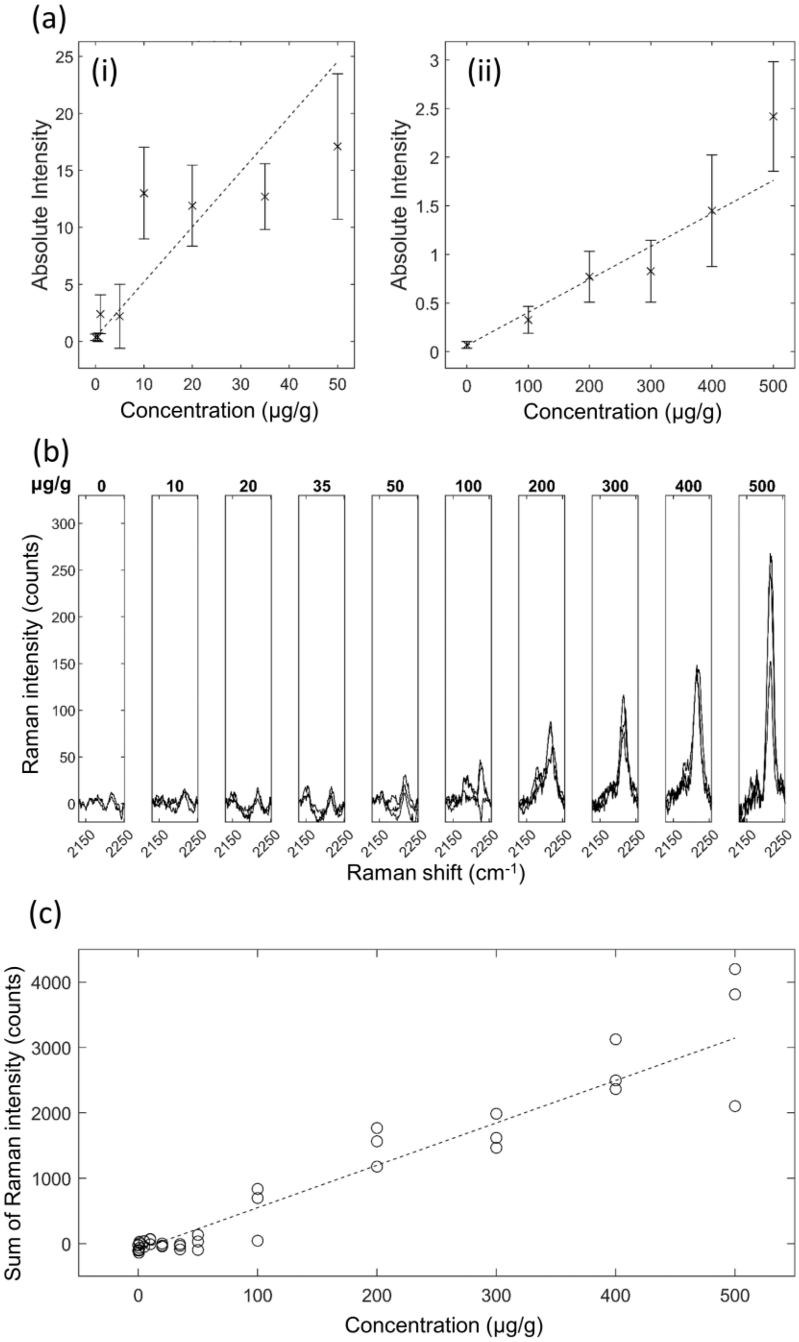

Figure 44: Ponatinib in rat liver mimetic tissue model. a(i): Weighted regression fit of MALDI-intensity of 183.56 Da mass peak for 0 – 50 μg/g mimetic tissue model (dotted line), mean measured signal at given concentration and standard deviation (crosses and bars). a(ii): Weighted regression fit of MALDI-intensity of 183.56 Da mass peak for 0 – 500 μg/g mimetic tissue model. (b): Integration time-normalized 2220 cm^{-1} peak in mimetic tissue models. Three randomly sampled locations of each mimetic tissue model were measured for each concentration. (c): Linear regression fit of sum of signal under

2220 cm^{-1} peak at given concentration (dotted line), measured signal under peak at given concentration for each sample (circles).

GSK4 in brain mimetic tissue model

The results for GSK4 in brain are shown in Figure 6. After baseline subtraction, the 2236 cm-1 peak was visible as shown in Figure 6(b). The lowest concentration with a visible Raman peak at 2236 cm-1 measured was 100 µg/g, and the lowest concentration with a significant measured signal (area under peak) was 100 µg/g. The quantification curve had a gradient of 1.14 counts/(µg/g), with r=0.82. The limit of detection was 80±14 µg/g. The other silent region peaks corresponding to C-D bonds were not detected at the concentrations and measurement times used in this study.

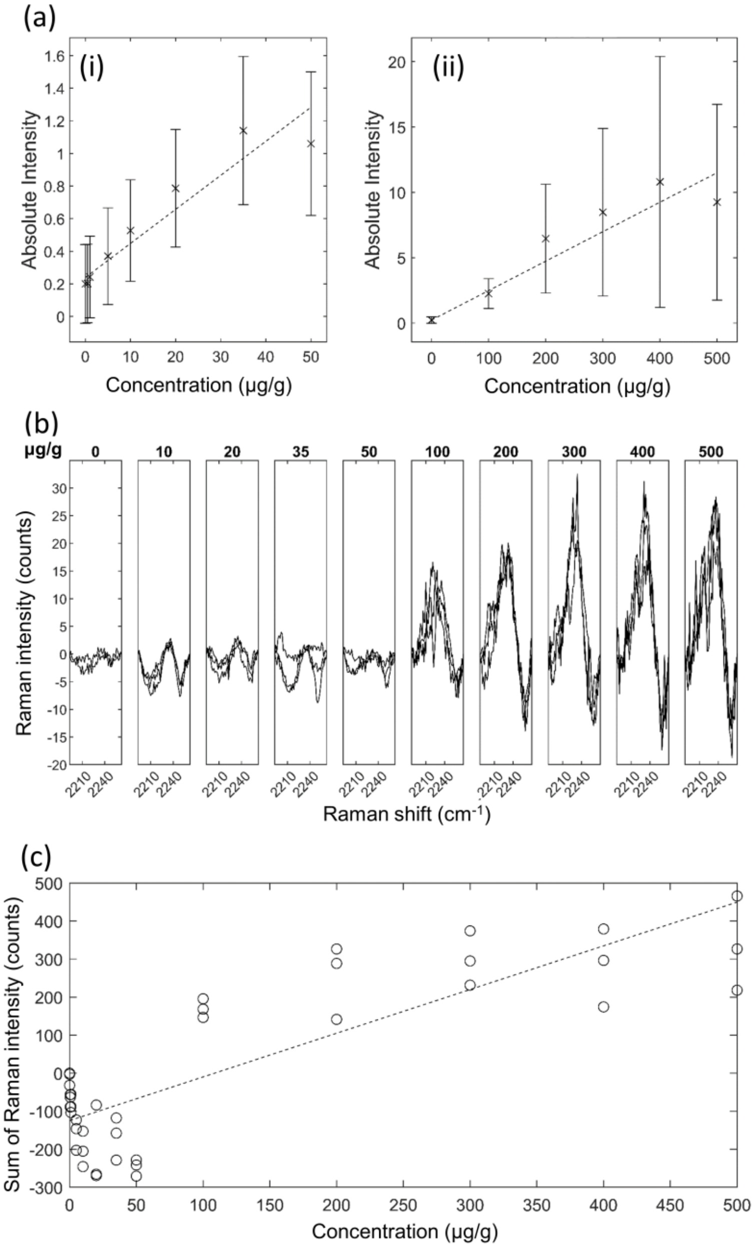

Figure 45: GSK4 in rat brain mimetic tissue model. a(i): Weighted regression fit of MALDI-intensity of 250.6 Da mass peak for 0 – 50 µg/g mimetic tissue model (dotted line), mean measured signal at given concentration and standard deviation (crosses and bars). a(ii): Weighted regression fit of MALDI-intensity of 250.6 Da mass peak for 0 – 500 µg/g mimetic tissue model. (b): Integration time-normalized 2236 cm^{-1} peak in mimetic tissue models. Three randomly sampled locations of each mimetic tissue model were measured for each concentration. (C): Linear regression fit of sum of signal under 2236 cm^{-1} peak at given concentration (dotted line), measured signal under peak at given concentration for each sample (circles).

GSK4 in liver mimetic tissue model

The results for GSK4 in liver are shown in Figure 46. The 2236 cm-1 peak, after tissue spectrum subtraction, was visible in the spectra of drugged mimetic tissue models at higher concentrations as in Figure 46(b). High levels of background variation were visible in these spectra, along with high signal variation in the 500 µg/g measurements. The other bands assigned to C-D in the silent region were not detected. Time-normalization of the spectra enables direct peak strength comparison between the measurements of different drug concentrations. The lowest concentration with a visible Raman peak at 2236 cm-1 measured was 100 µg/g, and the lowest concentration with a significant measured signal was 100 µg/g. The quantification curve had a gradient of 0.8 counts/(µg/g), with r=0.5. The limit of detection was 170±20 µg/g.

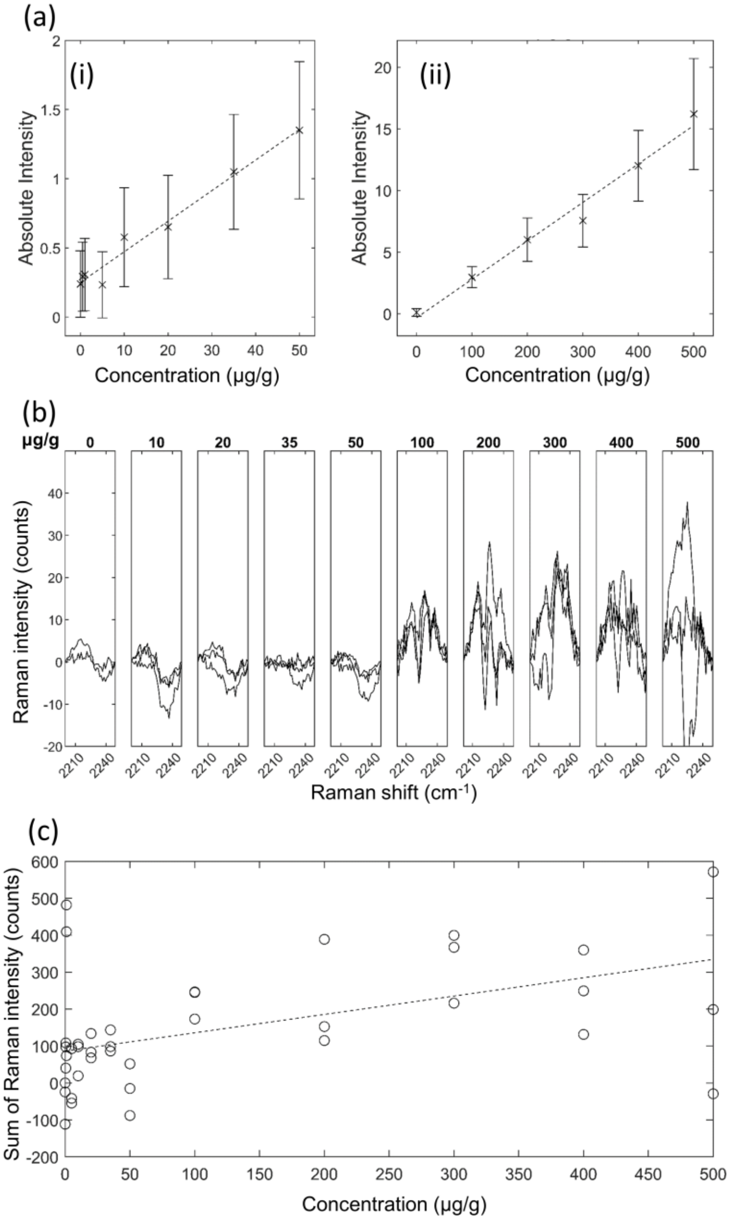

Figure 46: GSK4 in rat liver mimetic tissue model. a(i): Weighted regression fit of MALDI-intensity of 250.6 Da mass peak for 0 – 50 µg/g mimetic tissue model (dotted line), mean measured signal at given concentration and standard deviation (crosses and bars). a(ii): Weighted regression fit of MALDI-intensity of 250.6 Da mass peak for 0 – 500 µg/g mimetic tissue model. (b): Integration time-normalized 2236 cm^{-1} peak in mimetic tissue models. Three randomly sampled locations of each mimetic tissue model were measured for each concentration. (c): Linear regression fit of sum of signal under 2236 cm^{-1} peak at given concentration (dotted line), measured signal under peak at given concentration for each sample (circles).

GSK4x in brain mimetic tissue model

The results for GSK4x in brain are shown in Figure 47. The 2236 cm^{-1} peak, after tissue spectrum subtraction, was visible in the spectra of drugged mimetic tissue models at higher concentrations as in Figure 47 (b). High background variation was visible in these spectra, especially in the 35 µg/g measurements. The lowest concentration with a visible Raman peak at 2236 cm^{-1} measured was 100 µg/g, and the lowest concentration with a significant measured signal (area under peak) was 300 µg/g. The quantification curve had a gradient of 1.58 Counts/(µg/g), with r=0.76. The limit of detection was 270±30 µg/g.

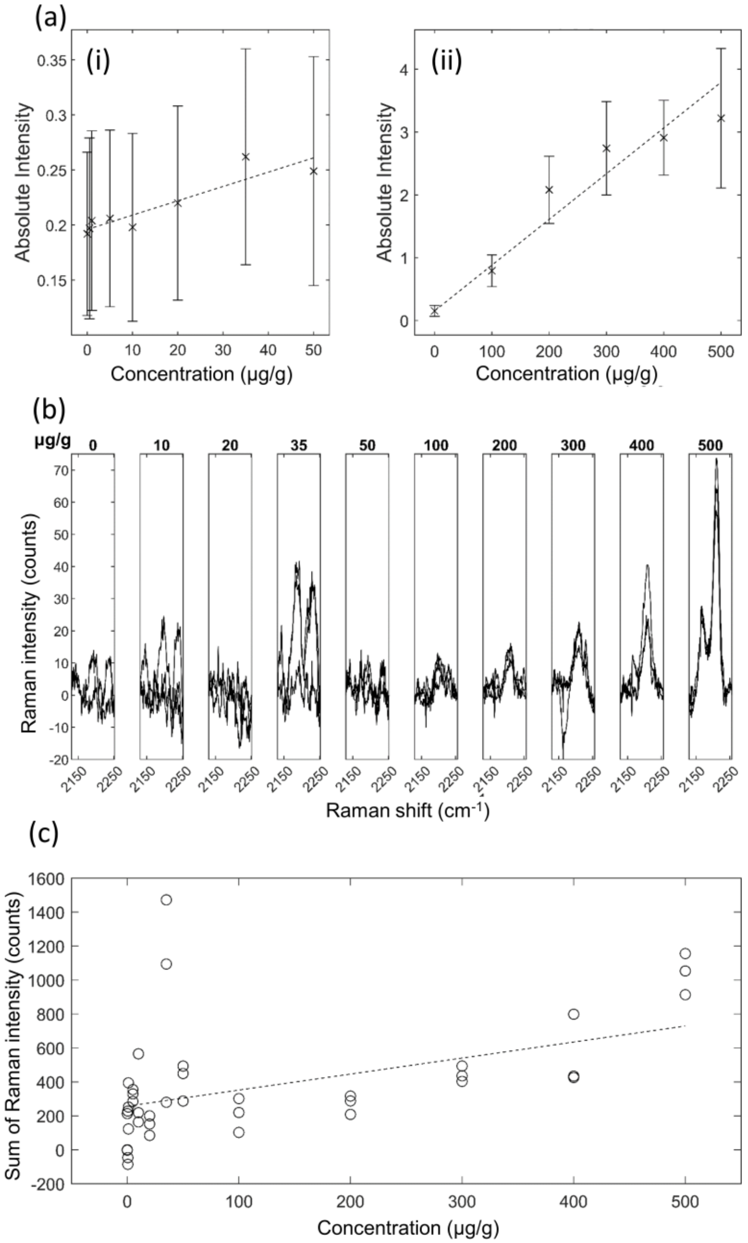

Figure 47: GSK4x in rat brain mimetic tissue model. a(i): Weighted regression fit of MALDI-intensity of 242.7 Da mass peak for 0 – 50 μg/g mimetic tissue model (dotted line), mean measured signal at given concentration and standard deviation (crosses and bars). a(ii): Weighted regression fit of MALDI-intensity of 242.7 Da mass peak for 0 – 500 μg/g mimetic tissue model. (b): Integration time-normalized 2236 cm^{-1} peak in mimetic tissue models. Three randomly sampled locations of each mimetic tissue model were measured for each concentration. (c): Linear regression fit of sum of signal under 2220 cm^{-1} peak at given concentration (dotted line), measured signal under peak at given concentration for each sample (circles).

GSK4x in liver mimetic tissue model

The results for GSK4x in tissue are shown in Figure 48. GSK4x exhibited a single Raman peak in the silent region, at 2236 cm^{-1}. The 2236 cm^{-1} peak, after tissue spectrum subtraction, was visible in the spectra of drugged mimetic tissue models at higher concentrations as in Figure 48(b). Because the spectra have been normalized to total integration time and to the pure reference tissue mimetic model spectrum of each sample, the strength of the peaks can be compared directly to make quantitative predictions. The lowest concentration with a visible Raman peak at 2236 cm^{-1} measured was 200 µg/g, and the lowest concentration with a significant measured signal (area under peak) was 300 µg/g. The quantification curve had a gradient of 0.42 Counts/(µg/g), with r=0.7. The limit of detection was 2900±300 µg/g. This limit of detection is much higher than that of the GSK4x brain mimetic model despite the peak being visible in the same range. The interference fringes in the spectra were sufficiently strong in these measurements to cause significant overlap with the peak such that, while the 2236 cm^{-1} peak could be seen at 400 µg/g, it was difficult to discriminate from the background fringes without looking at the adjacent concentration spectra. This resulted in a 0 signal measured at this concentration that impaired the quantification curve fitting. These interference fringes also resulted in a high noise floor that could not be reliably subtracted.

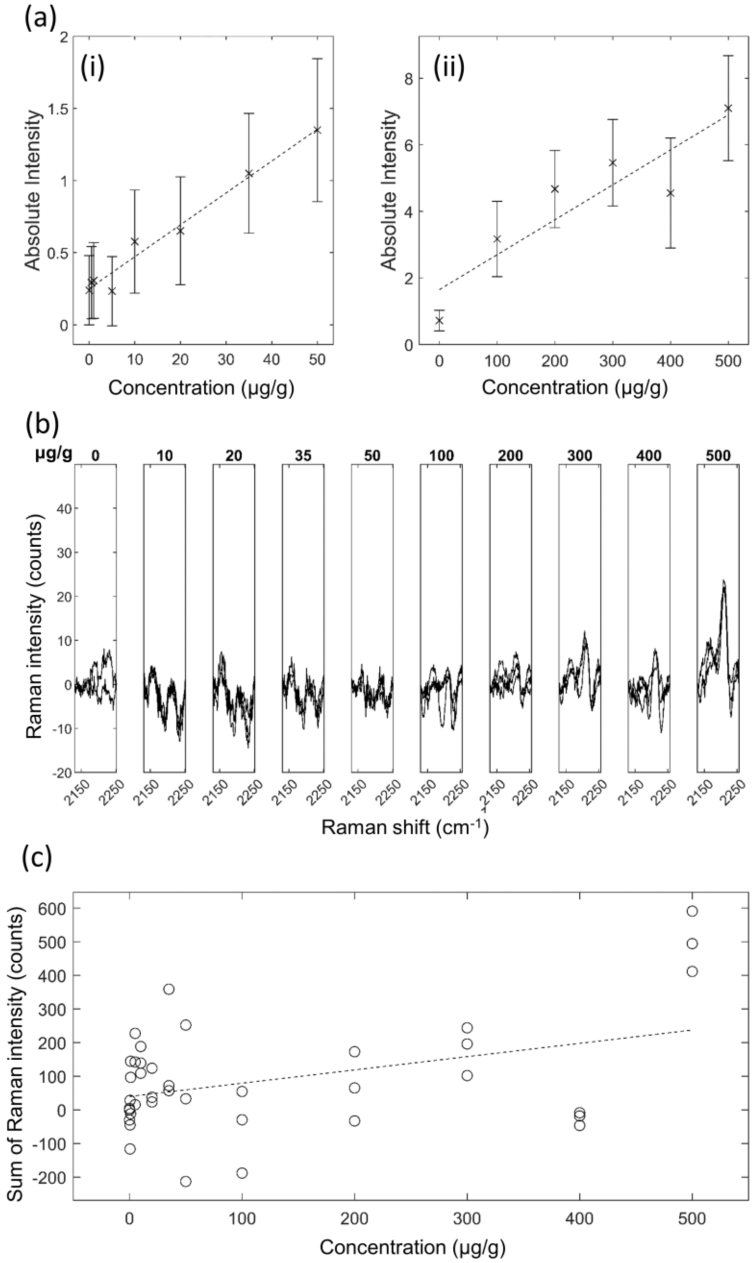

Figure 48: GSK4x in rat liver mimetic tissue model. a(i): Weighted regression fit of MALDI-intensity of 242.7 Da mass peak for 0 – 50 µg/g mimetic tissue model (dotted line), mean measured signal at given concentration and standard deviation (crosses and bars). a(ii): Weighted regression fit of MALDI-intensity of 242.7 Da mass peak for 0 – 500 µg/g mimetic tissue model. (b): Integration time-normalized 2236 cm^{-1} peak in mimetic tissue models. Three randomly sampled locations of each mimetic tissue model were measured for each concentration. (c): Linear regression fit of sum of signal under 2220 cm^{-1} peak at given concentration (dotted line), measured signal under peak at given concentration for each sample (circles).

Drug spectral features were found in all mimetic tissue models except for the models measuring deuterated acetaminophen. The Raman spectra of deuterated acetaminophen is presented in Figure 49 for the high concentration brain model. However, the deuterated acetaminophen models could not be verified with MALDI imaging (considered standard of reference), which also could not detect the drug.

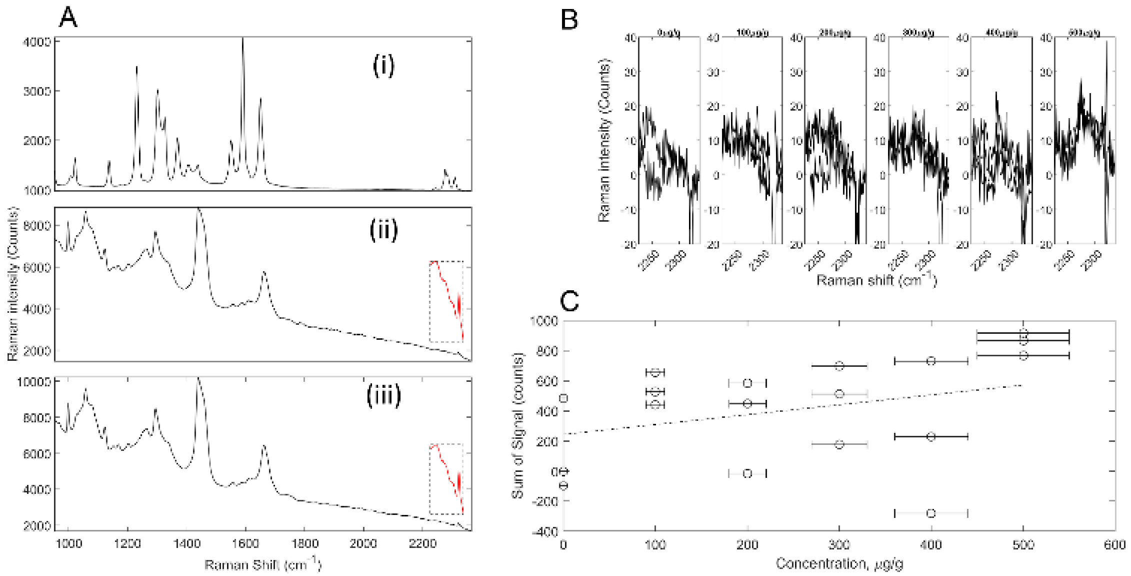

Figure 49: Results from 785nm tests of deuterated acetaminophen in rat brain mimetic tissue model. A(i): Raman spectrum of drug. A(ii): Raman spectrum of 500ug/g mimetic tissue model. Inset in dotted box is the location of the 2276cm-1 and 2309cm-1 peaks, magnified by factor of 10. A(iii): Raman spectrum of pure rat brain mimetic tissue model. Inset in dotted box is the location of the 2276cm-1 and 2309cm-1 peaks, magnified by factor of 10. B: Integration time-normalized 2276cm-1 and 2309cm-1 peaks in mimetic tissue models. Three randomly sampled locations of each mimetic tissue model were measured for each concentration. C: Linear regression fit of sum of signal under silent region peak locations at given concentration (dotted line), Measured signal under peak at given concentration for each sample (circles). R-coefficient of regression line = 0.32, Limit of detection undetermined, being greater than 500µg/g.

7.4. Discussion

With the combined use of thin tissue sections and high laser power, the autofluorescence emission of tissue was mitigated, enabling acquisition of Raman spectra of both brain and liver tissue and allow detection of drugs in the range 18-300 µg/g. The sample geometry also lends itself to high spatial resolution measurements as the significant out-of-focus tissue was removed. As measurements are non-destructive, it is also potentially useful for multivariate imaging, where consecutive sections of tissue can be measured with different imaging modalities[22].

Using 785 nm laser for excitation in Raman spectroscopy led to a higher SNR and therefore lower detection limit for detecting drug in the tissues compared to 671 nm laser. This was due to the reduced autofluorescent background and higher potential laser illumination power. The difference, however, was less extreme than expected: less than one order of magnitude. This result means that many factors in future experiments could affect which wavelength to use, including the specific tissue and drugs being measured. Tissues with very low fluorescence emission, or drugs with relevant Raman peaks in the high wavenumber region (> 2800 cm^{-1}), or high in the silent region may demonstrate better results with 671 nm. Instruments with detectors that have been designed to reduce the oscillating background caused by interference could also make the lower laser wavelengths the better choice. Conversely, for tissues exhibiting very high autofluorescence or drugs with discriminable peaks at lower wavenumbers, higher laser wavelengths than 785 nm may improve the detection limits of spontaneous Raman spectroscopy.

Ponatinib in brain was the drug/tissue mimetic model combination measured with the lowest limit of detection, due to ponatinib having the strongest silent region peak and brain having the lowest noise contribution, of the drugs and tissues measured in this study. The higher limit of detection in the ponatinib/liver mimetic tissue model relative to that of the brain mimetic tissue model was due to the increased background noise from the liver, as well as the increased background causing the interference pattern in the CCD to become relatively stronger. This pattern, visible in the inset in Figure 3A(iii), overlapped with the peak of interest and reduced certainty in what was or was not drug signal at lower concentrations.

For the GSK4/brain mimetic tissue model, the limit of detection relative to that of the ponatinib mimetic tissue model was higher, which was likely primarily due to the significantly reduced drug signal in the mimetic tissue models, about a 10x decrease in signal relative to background for a given concentration. The only measurable peak in the silent region was that from the alkyne group, with the deuteration peaks not visible in the mimetic tissue model spectra. In the GSK4/liver mimetic tissue model, the quantification curve had little correlation to actual concentration, which was exacerbated by high relative noise levels in the high concentration models. The poor correlation could be due to metabolism of the drug in the tissue, as the tissues have not been fixed prior to measurement. Quantitative measurement of this drug/tissue combination would require longer measurement times at these concentrations to generate a reproducible quantification curve.

For the GSK4X mimetic tissue models, the limits of detection were much higher than that of the GSK4 mimetic tissue model despite the peak being visible in the same range. The noise levels in these models were less consistent, leading to great increases in background as can be seen in Figure 6B, where one of the spectra at 20 µg/g were much higher than the drug signal should have been.

The comparison of GSK4 and GSK4X shows that deuteration is a much weaker label for spontaneous Raman spectroscopy measurements than alkyne groups. Combined with the results from deuterated acetaminophen, none of the Raman peaks assignable to C-D bonds were detected in this study. The alkyne group band at ~ 2220 cm^{-1} was reliably measurable from all mimetic tissue models that contained an alkyne group.

The variance in the drug concentration of the mimetic tissue models at 200 μm scale is shown by the MALDI imaging results. The samples were not investigated by other techniques at a scale below this resolution. Thus, the variance in measurements at each concentration described here could be a result of mimetic tissue model inhomogeneity. This, however, carries over into dosed tissue, where the drug distribution within a single

MALDI point could be very heterogeneous. For example, if a certain drug accumulates within a cell organelle, the MALDI result would show only the average drug concentration of the cell. With a diffraction-limited system, such as Raman microscopy used here (spatial resolution ~1 µm) the drug concentration of the organelle would be much higher within the organelle and reduced elsewhere. This means the limit of detection could still garner useful results even though they are lower than that of less spatially resolved imaging techniques.

The long acquisition times of our instruments generally excludes the application of spontaneous Raman spectroscopy to quantitative imaging or *in vivo* measurements, as the sample measured must be temporally stable. The high laser powers needed also precludes the use of the technique from live animal studies. However, as the quantification described here was all done using univariate spectral analysis away from the fingerprint region, there is potential for reducing total acquisition time in imaging using wide-field Raman imaging. This is a technique where, instead of a single location being measured across a wide spectral range at a time, a single narrow spectral range is binned and measured in an imaging format. This could essentially allow a whole map to be quantitatively measured in the same time as a single point is using our instruments[115]. Alternatively, the point-like Raman spectroscopy could be combined with other imaging modalities that can identify different tissue structures and cellular component, such that the Raman spectroscopy could be used for quantification of drug concentration in these different parts of tissue. Similar multimodal spectral imaging where selective-sampling Raman spectroscopy was combined with autofluorescence imaging or real-time computation of sampling points was previously demonstrated for 10-100-fold decrease in tissue analysis with applications in cancer surgery[71,73,116,117]. The use of software controllable multi-foci Raman spectroscopy in power-sharing mode has also been reported as a technique that can be used to measure simultaneous Raman spectra from several locations in tissue[69,82].

The predictive model gave detection limit predictions to within an order of magnitude of the empirically measured detection limits for three of the measured drugs. For acetaminophen, which was not detected at any concentration in either of the mimetic models, the predictive model was entirely insufficient. The predictive model relies on quantitative measurements of the drug of interest, which could not be produced due to the drug crystals being much larger than the spatial resolution of the systems. Additionally, the inconsistent conformation of the crystals to the slide surface meant that positioning the drug samples for measurement was difficult. Additionally, it works on the assumption that the drug does not interact at all with the tissue, which is both antithetical to its purpose means of drug detection modelling, and ignores the possibility of any chemical interactions that could happen to the drug making the Raman features used to detect the drug disappear. This is likely the reason for acetaminophen becoming undetectable in the mimetic tissue models.

7.5. Conclusions

Current techniques available for quantifying drugs in tissue (HPLC, mass spectroscopy) are destructive and have poor spatial resolution, limiting cellular and sub-cellular quantitative analysis of tissue. This study shows that spontaneous Raman spectroscopy is a promising technique for quantitative analysis of drug concentration in even highly fluorescent tissues. The linear response of the technique allows simple quantification of measurements, at the cost of longer acquisition times than previously mentioned alternatives. The results show that certain drugs can be measured at pharmacologically relevant concentrations using a diffraction-limited spatially resolved (~1 μm lateral resolution, ~10 μm axial resolution), non-destructive technique that requires no sample preparation. This means that Raman spectroscopic measurements can be quantified with only per-instrument calibration, as opposed to per-sample calibration of methods that require sample spraying. A Raman microscope can be calibrated for a given drug/tissue combination using a mimetic tissue model and then used repeatably on multiple dosed tissue samples without additional calibration controls. The thin samples used also enables cross correlation of measurements taken from different analysis modalities, by measuring consecutive sections with different instruments[83].

While this study demonstrated the potential, further studies are required using intact tissue from animals exposed to medically relevant levels of drugs to evaluate the system on real world dosed tissue. The metabolism of the drugs in dosed animals may sufficiently change the structure of the drugs to the extent that the Raman signature of the drugs is no longer represented by mimetic tissue models.

8. Conclusions and future prospects

The instruments and sample preparation techniques presented in this thesis quantitatively detect alkyne-tagged molecules in rat brain and rat liver mimetic tissue models at drug concentrations as low as 18 µg/g and 34 µg/g respectively, with 2-hour measurements. They are also capable of large FOV (> 1 cm) mapping of thin (~ 16 µm) tissue samples at 1 µm lateral and 13 µm axial resolution using Raman micro-spectroscopy. These capabilities combined offer potential for high-resolution mapping and quantification of alkyne-tagged drugs within tissue.

Raman spectroscopy of highly autofluorescent tissue, like liver, can be performed using both 671 nm and 785 nm excitation lasers, with sufficient photobleaching that can be accomplished without other detectable laser damage to the tissue. The ability to use shorter excitation wavelengths improves the quantum efficiency of CCDs, and the Raman scattering coefficient. These combined lead to increased Raman throughput, normally completely negated by the increased autofluorescence. While the SNR for 671 nm excitation was found to be ~ 1.7 – 3.7x lower for 671 nm compared to 785 nm (see section 7.3), this was for a specific application of detecting drugs in the centre of the silent region (~ 2220 cm^{-1}). For studies involving detection of materials at higher wavenumbers or in less fluorescent tissues, these ratios may invert. Additionally, as the laser powers used in these studies were not equal between wavelengths due to concerns of laser damage to the samples, further laser damage mitigation to the tissues through pre-measurement fluorophore destruction may enable higher laser powers using 671 nm, leading to increased SNR for a given measurement time. Furthermore, shorter wavelengths generally exhibit increased Raman activity in the form of resonance Raman scattering. This process can be selectively increased by careful choice of laser, but would require further fluorescence suppression.

While the measurement speed for spontaneous Raman spectroscopy for drug detection in tissue at similar concentrations was much lower than that of mass spectrometry (~2 hours for RS versus ~0.4 s for MALDI), the detection limit of mass spectrometry is fundamentally limited by its spatial resolution and its destructive nature; the detection limit cannot be improved by simply increasing the measurement time. Further acquisition increases can be made by simultaneous measurement of multiple points within the sample, be it through line-scanning Raman microscopy or multi-point confocal Raman microscopy[69]. Additionally, since the drug detection performed in this thesis only utilised a single Raman peak in the silent region, wide-field Raman microscopy has potential for rapidly increasing the imaging rate of a given FOV by simultaneously measuring a specific wavenumber of all points in the FOV. This method reduces the instantaneous laser power density at any given point in the sample, while enabling the use of the full power of the excitation laser. This would also forego the need for a spectrograph, increasing the efficiency of the detection pathway of the microscope while increasing the acquisition rate in a way limited primarily by the power output of most lasers instead of the damage threshold of the sample.

Alternatively, the exclusive use of single-wavenumber detection substantially impedes the detection limit of Raman spectroscopy for certain drugs. While alkyne-tagged drugs exhibit few features in the silent region, deuterated drugs can exhibit several. The combined sum of all of these peaks would decrease the detection limit even if they were not individually discriminable from the noise floor.

9. References

(1) Li, C.; Wang, J.; Wang, Y.; Gao, H.; Wei, G.; Huang, Y.; Yu, H.; Gan, Y.; Wang, Y.; Mei, L.; Chen, H.; Hu, H.; Zhang, Z.; Jin, Y. Recent Progress in Drug Delivery. *Acta Pharm. Sin. B* **2019**, *9* (6), 1145–1162. https://doi.org/10.1016/j.apsb.2019.08.003.

(2) Ceña, V.; Játiva, P. Nanoparticle Crossing of Blood-Brain Barrier: A Road to New Therapeutic Approaches to Central Nervous System Diseases. *Nanomedicine* **2018**, *13* (13), 1513–1516. https://doi.org/10.2217/nnm-2018-0139.

(3) Vijayakameswara Rao, N.; Ko, H.; Lee, J.; Park, J. H. Recent Progress and Advances in Stimuli-Responsive Polymers for Cancer Therapy. *Front. Bioeng. Biotechnol.* **2018**, *6* (AUG). https://doi.org/10.3389/fbioe.2018.00110.

(4) Kong, F. Y.; Zhang, J. W.; Li, R. F.; Wang, Z. X.; Wang, W. J.; Wang, W. Unique Roles of Gold Nanoparticles in Drug Delivery, Targeting and Imaging Applications. *Molecules* **2017**, *22* (9). https://doi.org/10.3390/molecules22091445.

(5) Minati, L.; Maniglio, D.; Benetti, F.; Chiappini, A.; Speranza, G. Multimodal Gold Nanostars as SERS Tags for Optically-Driven Doxorubicin Release Study in Cancer Cells. *Materials (Basel).* **2021**, *14* (23). https://doi.org/10.3390/ma14237272.

(6) Li, Y.; Wei, Q.; Ma, F.; Li, X.; Liu, F.; Zhou, M. Surface-Enhanced Raman Nanoparticles for Tumor Theranostics Applications. *Acta Pharm. Sin. B* **2018**, *8* (3), 349–359. https://doi.org/10.1016/j.apsb.2018.03.007.

(7) El-Mashtoly, S. F.; Petersen, D.; Yosef, H. K.; Mosig, A.; Reinacher-Schick, A.; Kötting, C.; Gerwert, K. Label-Free Imaging of Drug Distribution and Metabolism in Colon Cancer Cells by Raman Microscopy. *Analyst* **2014**, *139* (5), 1155–1161. https://doi.org/10.1039/c3an01993d.

(8) Waters, J. C. Accuracy and Precision in Quantitative Fluorescence Microscopy. *J. Cell Biol.* **2009**, *185* (7), 1135–1148. https://doi.org/10.1083/jcb.200903097.

(9) Winterhalder, M. J.; Zumbusch, A. Beyond the Borders - Biomedical Applications of Non-Linear Raman Microscopy. *Advanced Drug Delivery Reviews*. Elsevier July 15, 2015, pp 135–144. https://doi.org/10.1016/j.addr.2015.04.024.

(10) Zhao, Z.; Shen, Y.; Hu, F.; Min, W. Applications of Vibrational Tags in Biological Imaging by Raman Microscopy. *Analyst* **2017**, *142* (21), 4018–4029. https://doi.org/10.1039/c7an01001j.

(11) Vanden-Hehir, S.; Tipping, W. J.; Lee, M.; Brunton, V. G.; Williams, A.; Hulme, A. N. Raman Imaging of Nanocarriers for Drug Delivery. *Nanomaterials*. MDPI AG March 1, 2019. https://doi.org/10.3390/nano9030341.

(12) Patel, M.; Bueters, T. Can Quantitative Pharmacology Improve Productivity in Pharmaceutical Research and Development? *Expert Opin. Drug Discov.* **2020**, *15* (10), 1111–1114. https://doi.org/10.1080/17460441.2020.1776257.

(13) Koller, D.; Vaitsekhovich, V.; Mba, C.; Steegmann, J. L.; Zubiaur, P.; Abad-Santos, F.; Wojnicz, A. Effective Quantification of 11 Tyrosine Kinase Inhibitors and Caffeine in Human Plasma by Validated LC-MS/MS Method with Potent Phospholipids Clean-up Procedure. Application to Therapeutic Drug Monitoring. *Talanta* **2020**, *208*, 120450. https://doi.org/https://doi.org/10.1016/j.talanta.2019.120450.

(14) Aikawa, H.; Hayashi, M.; Ryu, S.; Yamashita, M.; Ohtsuka, N.; Nishidate, M.; Fujiwara, Y.; Hamada, A. Visualizing Spatial Distribution of Alectinib in Murine Brain Using Quantitative Mass Spectrometry Imaging. *Sci. Rep.* **2016**, *6* (March), 1–9. https://doi.org/10.1038/srep23749.

(15) Araújo, L. M. G. de; Serigiolle, L. C.; Gomes, H. M. P.; Rodrigues, D. A. B.; Lopes, C. M.; Leme, P. L. S. Volume Calculation of Rats' Organs and Its Application in the Validation of the Volume Relation between the Abdominal Cavity and the Hernial Sac in Incisional Hernias with "Loss of Abdominal Domain". *Arq. Bras. Cir. Dig. ABCD = Brazilian Arch. Dig. Surg.* **2014**, *27* (3), 177–181. https://doi.org/10.1590/s0102-67202014000300004.

(16) Tanguay, J.; Benard, F.; Celler, A.; Ruth, T.; Schaffer, P. Spatial Resolution Properties of Digital Autoradiography Systems for Pre-Clinical Alpha Particle Imaging (Conference

Presentation). In *Society of Photo-Optical Instrumentation Engineers (SPIE) Conference Series*; Society of Photo-Optical Instrumentation Engineers (SPIE) Conference Series; 2017; Vol. 10137, p 1013716. https://doi.org/10.1117/12.2252282.

(17) Solon, E. G. Use of Radioactive Compounds and Autoradiography to Determine Drug Tissue Distribution. *Chem. Res. Toxicol.* **2012**, *25* (3), 543–555. https://doi.org/10.1021/tx200509f.

(18) Solon, E. G.; Schweitzer, A.; Stoeckli, M.; Prideaux, B. Autoradiography, MALDI-MS, and SIMS-MS Imaging in Pharmaceutical Discovery and Development. *Am. Assoc. Pharm. Sci.* **2009**, *12* (1), 11–26. https://doi.org/10.1208/s12248-009-9158-4.

(19) Hesk, D.; McNamara, P. Synthesis of Isotopically Labelled Compounds at Schering-Plough, an Historical Perspective. *J. Label. Compd. Radiopharm.* **2007**, *50*, 875–887. https://doi.org/10.1002/jlcr.1424.

(20) Crossman, L.; McHugh, N. A.; Hsieh, Y.; Korfmacher, W. A.; Chen, J. Investigation of the Profiling Depth in Matrix-Assisted Laser Desorption/Ionization Imaging Mass Spectrometry. *Rapid Commun. Mass Spectrom.* **2006**, *20* (2), 284–290. https://doi.org/10.1002/rcm.2259.

(21) Feenstra, A. D.; Dueñas, M. E.; Lee, Y. J. Five Micron High Resolution MALDI Mass Spectrometry Imaging with Simple, Interchangeable, Multi-Resolution Optical System. *J. Am. Soc. Mass Spectrom.* **2017**, *28* (3), 434–442. https://doi.org/10.1007/s13361-016-1577-8.

(22) Prentice, B. M.; Caprioli, R. M. The Need for Speed in Matrix-Assisted Laser Desorption/Ionization Imaging Mass Spectrometry. *Postdoc J.* **2016**, *4* (3), 3–13. https://doi.org/10.14304/surya.jpr.v4n3.1.

(23) Nishidate, M.; Hayashi, M.; Aikawa, H.; Tanaka, K.; Nakada, N.; Miura, S. ichi; Ryu, S.; Higashi, T.; Ikarashi, Y.; Fujiwara, Y.; Hamada, A. Applications of MALDI Mass Spectrometry Imaging for Pharmacokinetic Studies during Drug Development. *Drug Metabolism and Pharmacokinetics*. 2019. https://doi.org/10.1016/j.dmpk.2019.04.006.

(24) Garate, J.; Fernández, R.; Lage, S.; Bestard-Escalas, J.; Lopez, D. H.; Reigada, R.; Khorrami,

S.; Ginard, D.; Reyes, J.; Amengual, I.; Barceló-Coblijn, G.; Fernández, J. A. Imaging Mass Spectrometry Increased Resolution Using 2-Mercaptobenzothiazole and 2,5-Diaminonaphtalene Matrices: Application to Lipid Distribution in Human Colon. *Anal. Bioanal. Chem.* **2015**, *407* (16), 4697–4708. https://doi.org/10.1007/s00216-015-8673-7.

(25) Bowman, A. P.; Bogie, J. F. J.; Hendriks, J. J. A.; Haidar, M.; Belov, M.; Heeren, R. M. A.; Ellis, S. R. Evaluation of Lipid Coverage and High Spatial Resolution MALDI-Imaging Capabilities of Oversampling Combined with Laser Post-Ionisation. *Anal. Bioanal. Chem.* **2020**, *412* (10), 2277–2289. https://doi.org/10.1007/s00216-019-02290-3.

(26) Zavalin, A.; Yang, J.; Haase, A.; Holle, A.; Caprioli, R. Implementation of a Gaussian Beam Laser and Aspheric Optics for High Spatial Resolution MALDI Imaging MS. *J. Am. Soc. Mass Spectrom.* **2014**, *25*, 1079–1082. https://doi.org/10.1007/s13361-014-0872-5.

(27) Spivey, E. C.; McMillen, J. C.; Ryan, D. J.; Spraggins, J. M.; Caprioli, R. M. Combining MALDI-2 and Transmission Geometry Laser Optics to Achieve High Sensitivity for Ultra-High Spatial Resolution Surface Analysis. *J. Mass Spectrom.* **2019**, *54* (4), 366–370. https://doi.org/https://doi.org/10.1002/jms.4335.

(28) Barry, J. A.; Groseclose, M. R.; Castellino, S. Quantification and Assessment of Detection Capability in Imaging Mass Spectrometry Using a Revised Mimetic Tissue Model. *Bioanalysis* **2019**, *11* (11), 1099–1116. https://doi.org/10.4155/bio-2019-0035.

(29) Gu, H.; Ma, K.; Zhao, W.; Qiu, L.; Xu, W. A General Purpose MALDI Matrix for the Analyses of Small Organic, Peptide and Protein Molecules. *Analyst* **2021**, *146* (12), 4080–4086. https://doi.org/10.1039/d1an00474c.

(30) Monroe, E. B.; Annangudi, S. P.; Hatcher, N. G.; Gutstein, H. B.; Rubakhin, S. S.; Sweedler, J. V. SIMS and MALDI MS Imaging of the Spinal Cord. *Proteomics* **2008**, *8* (18), 3746–3754. https://doi.org/10.1002/pmic.200800127.

(31) Bednařík, A.; Machálková, M.; Moskovets, E.; Coufalíková, K.; Krásenský, P.; Houška, P.; Kroupa, J.; Navrátilová, J.; Šmarda, J.; Preisler, J. MALDI MS Imaging at Acquisition Rates Exceeding 100 Pixels per Second. *J. Am. Soc. Mass Spectrom.* **2019**, *30* (2), 289–298. https://doi.org/10.1007/s13361-018-2078-8.

(32) Parrot, D.; Papazian, S.; Foil, D.; Tasdemir, D. Imaging the Unimaginable: Desorption Electrospray Ionization - Imaging Mass Spectrometry (DESI-IMS) in Natural Product Research. *Planta Med.* **2018**, *84* (9–10), 584–593. https://doi.org/10.1055/s-0044-100188.

(33) Barre, F. P. Y.; Heeren, R. M. A.; Potocnik, N. O. Mass Spectrometry Imaging in Nanomedicine: Unraveling the Potential of MSI for the Detection of Nanoparticles in Neuroscience. *Curr. Pharm. Des.* **2017**, *23* (13), 1974–1984. https://doi.org/10.2174/1381612823666170111112550.

(34) Lamont, L.; Hadavi, D.; Viehmann, B.; Flinders, B.; Heeren, R. M. A.; Vreeken, R. J.; Porta Siegel, T. Quantitative Mass Spectrometry Imaging of Drugs and Metabolites: A Multiplatform Comparison. *Anal. Bioanal. Chem.* **2021**, *413* (10), 2779–2791. https://doi.org/10.1007/s00216-021-03210-0.

(35) Agüi-Gonzalez, P.; Jähne, S.; Phan, N. T. N. SIMS Imaging in Neurobiology and Cell Biology. *J. Anal. At. Spectrom.* **2019**, *34* (7), 1355–1368. https://doi.org/10.1039/c9ja00118b.

(36) Frisz, J. F.; Lou, K.; Klitzing, H. A.; Hanafin, W. P.; Lizunov, V.; Wilson, R. L.; Carpenter, K. J.; Kim, R.; Hutcheon, I. D.; Zimmerberg, J.; Weber, P. K.; Kraft, M. L. Direct Chemical Evidence for Sphingolipid Domains in the Plasma Membranes of Fibroblasts. *Proc. Natl. Acad. Sci. U. S. A.* **2013**, *110* (8). https://doi.org/10.1073/pnas.1216585110.

(37) Braun, R. M.; Beyder, A.; Xu, J.; Wood, M. C.; Ewing, A. G.; Winograd, N. Spatially Resolved Detection of Attomole Quantities of Organic Molecules Localized in Picoliter Vials Using Time-of-Flight Secondary Ion Mass Spectrometry. *Anal. Chem.* **1999**, *71* (16), 3318–3324. https://doi.org/10.1021/ac9902042.

(38) Passarelli, M. K.; Winograd, N. Lipid Imaging with Time-of-Flight Secondary Ion Mass Spectrometry (ToF-SIMS). *Biochim. Biophys. Acta* **2011**, *1811* (11), 976–990. https://doi.org/10.1016/j.bbalip.2011.05.007.

(39) Groseclose, M. R.; Castellino, S. A Mimetic Tissue Model for the Quantification of Drug Distributions by MALDI Imaging Mass Spectrometry. *Anal. Chem.* **2013**, *85* (21), 10099–

10106. https://doi.org/10.1021/ac400892z.

(40) Schulz, S.; Becker, M.; Groseclose, M. R.; Schadt, S.; Hopf, C. Advanced MALDI Mass Spectrometry Imaging in Pharmaceutical Research and Drug Development. *Current Opinion in Biotechnology*. 2019. https://doi.org/10.1016/j.copbio.2018.08.003.

(41) Van Der Zwaag, D.; Vanparijs, N.; Wijnands, S.; De Rycke, R.; De Geest, B. G.; Albertazzi, L. Super Resolution Imaging of Nanoparticles Cellular Uptake and Trafficking. *ACS Appl. Mater. Interfaces* **2016**, *8* (10), 6391–6399. https://doi.org/10.1021/acsami.6b00811.

(42) Wegel, E.; Göhler, A.; Lagerholm, B. C.; Wainman, A.; Uphoff, S.; Kaufmann, R.; Dobbie, I. M. Imaging Cellular Structures in Super-Resolution with SIM, STED and Localisation Microscopy: A Practical Comparison. *Sci. Rep.* **2016**, *6* (1), 27290. https://doi.org/10.1038/srep27290.

(43) Plajnšek, K. T.; Pajk, S.; Govedarica, B.; Pečar, S.; Srčič, S.; Kristl, J. A Novel Fluorescent Probe for More Effective Monitoring of Nanosized Drug Delivery Systems within the Cells. *Int. J. Pharm.* **2011**, *416* (1), 384–393. https://doi.org/10.1016/j.ijpharm.2011.06.046.

(44) Toseland, C. P. Fluorescent Labeling and Modification of Proteins. *J. Chem. Biol.* **2013**, *6* (3), 85–95. https://doi.org/10.1007/s12154-013-0094-5.

(45) Macdonald, A. M.; Wyeth, P. On the Use of Photobleaching to Reduce Fluorescence Background in Raman Spectroscopy to Improve the Reliability of Pigment Identification on Painted Textiles. *J. Raman Spectrosc. An Int. J. Orig. Work all Asp. Raman Spectrosc. Incl. High. Order Process. also Brillouin Rayleigh Scatt.* **2006**, *37* (8), 830–835.

(46) Zi\keba-Palus, J.; Michalska, A. Photobleaching as a Useful Technique in Reducing of Fluorescence in Raman Spectra of Blue Automobile Paint Samples. *Vib. Spectrosc.* **2014**, *74*, 6–12.

(47) Qin, Y. T.; Peng, H.; He, X. W.; Li, W. Y.; Zhang, Y. K. Highly Effective Drug Delivery and Cell Imaging Using Fluorescent Double-Imprinted Nanoparticles by Targeting Recognition of the Epitope of Membrane Protein. *Anal. Chem.* **2019**, *91* (20), 12696–12703. https://doi.org/10.1021/acs.analchem.9b02123.

(48) Raman, C. V.; Krishnan, K. S. A New Type of Secondary Radiation. *Nature* **1928**, *121* (3048), 501–502. https://doi.org/10.1038/121501c0.

(49) Ornstein, L. S.; Rekveld, J.; Utrecht. Intensity Measurements in the Raman Effect and the Distribution Law of Maxwell-Boltzmann. *Phys. Rev.* **1929**, *34* (5), 720–725. https://doi.org/10.1103/PhysRev.34.720.

(50) Yamakoshi, H.; Dodo, K.; Palonpon, A.; Ando, J.; Fujita, K.; Kawata, S.; Sodeoka, M. Alkyne-Tag Raman Imaging for Visualization of Mobile Small Molecules in Live Cells. *J. Am. Chem. Soc.* **2012**, *134* (51), 20681–20689. https://doi.org/10.1021/ja308529n.

(51) Born, M.; Wolf, E. *Principles of Optics: Electromagnetic Theory of Propagation, Interference and Diffraction of Light*, 7th ed.; Cambridge University Press: Cambridge, 1999. https://doi.org/DOI: 10.1017/CBO9781139644181.

(52) Griffiths, P. Handbook of Vibrational Spectroscopy; 2006; Vol. 1. https://doi.org/10.1002/0470027320.s0102.

(53) Reble, C.; Gersonde, I.; Lieber, C. A.; Helfmann, J. Influence of Tissue Absorption and Scattering on the Depth Dependent Sensitivity of Raman Fiber Probes Investigated by Monte Carlo Simulations. *Biomed. Opt. Express* **2011**, *2* (3), 520–533. https://doi.org/10.1364/BOE.2.000520.

(54) Marcu, L.; French, P. M. W. Tissue Fluorophores and Their Spectroscopic Characteristics. In *Fluorescence lifetime spectroscopy and imaging: principles and applications in biomedical diagnostics*; 2014; pp 48–84.

(55) Dou, X.; Yamaguchi, Y.; Yamamoto, H.; Uenoyama, H.; Ozaki, Y. Biological Applications of Anti-Stokes Raman Spectroscopy: Quantitative Analysis of Glucose in Plasma and Serum by a Highly Sensitive Multichannel Raman Spectrometer. *Appl. Spectrosc.* **1996**, *50* (10), 1301–1306.

(56) Dou, X.; Yamaguchi, Y.; Yamamoto, H.; Doi, S.; Ozaki, Y. Quantitative Analysis of Metabolites in Urine by Anti-Stokes Raman Spectroscopy. *Biospectroscopy* **1997**, *3* (2), 113–120. https://doi.org/https://doi.org/10.1002/(SICI)1520-6343(1997)3:2<113::AID-BSPY4>3.0.CO;2-8.

(57) Corden, C. J.; Shipp, D. W.; Matousek, P.; Notingher, I. Fast Raman Spectral Mapping of Highly Fluorescing Samples by Time-Gated Spectral Multiplexed Detection. *Opt. Lett.* **2018**, *43* (23), 5733–5736. https://doi.org/10.1364/OL.43.005733.

(58) Kostamovaara, J.; Tenhunen, J.; Kögler, M.; Nissinen, I.; Nissinen, J.; Keränen, P. Fluorescence Suppression in Raman Spectroscopy Using a Time-Gated CMOS SPAD. *Opt. Express* **2013**, *21* (25), 31632–31645. https://doi.org/10.1364/OE.21.031632.

(59) Lipiäinen, T.; Pessi, J.; Movahedi, P.; Koivistoinen, J.; Kurki, L.; Tenhunen, M.; Yliruusi, J.; Juppo, A. M.; Heikkonen, J.; Pahikkala, T.; Strachan, C. J. Time-Gated Raman Spectroscopy for Quantitative Determination of Solid-State Forms of Fluorescent Pharmaceuticals. *Anal. Chem.* **2018**, *90* (7), 4832–4839. https://doi.org/10.1021/acs.analchem.8b00298.

(60) Desroches, J.; Jermyn, M.; Pinto, M.; Picot, F.; Tremblay, M.-A.; Obaid, S.; Marple, E.; Urmey, K.; Trudel, D.; Soulez, G.; others. A New Method Using Raman Spectroscopy for in Vivo Targeted Brain Cancer Tissue Biopsy. *Sci. Rep.* **2018**, *8* (1), 1–10.

(61) McGregor, H. C.; Short, M. A.; Lam, S.; Shaipanich, T.; Beaudoin, E.-L.; Zeng, H. Development and in Vivo Test of a Miniature Raman Probe for Early Cancer Detection in the Peripheral Lung. *J. Biophotonics* **2018**, *11* (11), e201800055.

(62) Prats-Mateu, B.; Bock, P.; Schroffenegger, M.; Toca-Herrera, J. L.; Gierlinger, N. Following Laser Induced Changes of Plant Phenylpropanoids by Raman Microscopy. *Sci. Rep.* **2018**, *8* (1), 11804. https://doi.org/10.1038/s41598-018-30096-3.

(63) Lindquist, N. C.; de Albuquerque, C. D. L.; Sobral-Filho, R. G.; Paci, I.; Brolo, A. G. High-Speed Imaging of Surface-Enhanced Raman Scattering Fluctuations from Individual Nanoparticles. *Nat. Nanotechnol.* **2019**, *14* (10), 981–987. https://doi.org/10.1038/s41565-019-0535-6.

(64) Jelken, J.; Mazaheri, L.; Lagugné-Labarthet, F. Wide-Field Raman Microscopy with STORM Post-Processing: A Powerful Tool to Increase Spatial Resolution and Acquisition Speed in Raman Imaging. In *Multiscale Imaging and Spectroscopy III*; Campagnola, P. J., Maitland, K. C., Roblyer, D. M., Eds.; SPIE, 2022; Vol. PC11944. https://doi.org/10.1117/12.2608984.

(65) Nicolson, F.; Kircher, M. F.; Stone, N.; Matousek, P. Spatially Offset Raman Spectroscopy for Biomedical Applications. *Chem. Soc. Rev.* **2021**, *50* (1), 556–568. https://doi.org/10.1039/d0cs00855a.

(66) Kalkanis, S. N.; Kast, R. E.; Rosenblum, M. L.; Mikkelsen, T.; Yurgelevic, S. M.; Nelson, K. M.; Raghunathan, A.; Poisson, L. M.; Auner, G. W. Raman Spectroscopy to Distinguish Grey Matter, Necrosis, and Glioblastoma Multiforme in Frozen Tissue Sections. *J. Neurooncol.* **2014**. https://doi.org/10.1007/s11060-013-1326-9.

(67) Wei, L.; Hu, F.; Shen, Y.; Chen, Z.; Yu, Y.; Lin, C.-C.; Wang, M. C.; Min, W. Live-Cell Imaging of Alkyne-Tagged Small Biomolecules by Stimulated Raman Scattering. *Nat. Methods* **2014**, *11* (4), 410–412. https://doi.org/10.1038/nmeth.2878.

(68) Ando, J.; Dodo, K.; Fujita, K.; Sodeoka, M. Visualizing Bioactive Small Molecules by Alkyne Tagging and Slit-Scanning Raman Microscopy. *Methods Mol. Biol.* **2019**, *1888*, 99–114. https://doi.org/10.1007/978-1-4939-8891-4_5.

(69) Liao, Z.; Sinjab, F.; Hany, |; Elsheikha, M.; Notingher, I. Optical Sectioning in Multifoci Raman Hyperspectral Imaging. *J. Raman Spectrosc.* **2018**, 1–8. https://doi.org/10.1002/jrs.5450.

(70) Papour, A.; Kwak, J. H.; Taylor, Z.; Wu, B.; Stafsudd, O.; Grundfest, W. Wide-Field Raman Imaging for Bone Detection in Tissue. *Biomed. Opt. Express* **2015**, *6* (10), 3892–3897. https://doi.org/10.1364/BOE.6.003892.

(71) Rowlands, C. J.; Varma, S.; Perkins, W.; Leach, I.; Williams, H.; Notingher, I. Rapid Acquisition of Raman Spectral Maps through Minimal Sampling: Applications in Tissue Imaging. *J. Biophotonics* **2012**, *5* (3), 220–229. https://doi.org/10.1002/jbio.201100098.

(72) Boitor, R. Automated Multimodal Spectral Histopathology for Quantitative Diagnosis of Residual Tumour during Basal Cell Carcinoma Surgery by Radu Boitor MPhys. (Hons.) Supervised by Prof Ioan Notingher, University of Nottingham, 2019.

(73) Kong, K.; Rowlands, C. J.; Varma, S.; Perkins, W.; Leach, I. H.; Koloydenko, A. A.; Williams, H. C.; Notingher, I. Diagnosis of Tumors during Tissue-Conserving Surgery with Integrated Autofluorescence and Raman Scattering Microscopy. *Proc. Natl. Acad. Sci.* **2013**, *110* (38),

15189–15194. https://doi.org/10.1073/pnas.1311289110.

(74) Efremov, E. V; Ariese, F.; Gooijer, C. Achievements in Resonance Raman Spectroscopy: Review of a Technique with a Distinct Analytical Chemistry Potential. *Anal. Chim. Acta* **2008**, *606* (2), 119–134. https://doi.org/https://doi.org/10.1016/j.aca.2007.11.006.

(75) Tipping, W. J.; Lee, M.; Serrels, A.; Brunton, V. G.; Hulme, A. N. Stimulated Raman Scattering Microscopy: An Emerging Tool for Drug Discovery. *Chem. Soc. Rev.* **2016**, *45*, 2075–2089. https://doi.org/10.1039/C5CS00693G.

(76) Cheng, J. X.; Min, W.; Ozeki, Y.; Polli, D. *Stimulated Raman Scattering Microscopy: Techniques and Applications*; Elsevier Science, 2021.

(77) Virga, A.; Ferrante, C.; Batignani, G.; De Fazio, D.; Nunn, A. D. G.; Ferrari, A. C.; Cerullo, G.; Scopigno, T. Coherent Anti-Stokes Raman Spectroscopy of Single and Multi-Layer Graphene. *Nat. Commun.* **2019**, *10* (1), 3658. https://doi.org/10.1038/s41467-019-11165-1.

(78) Zheng, F.; Xiong, W.; Sun, S.; Zhang, P.; Zhu, J. J. Recent Advances in Drug Release Monitoring. *Nanophotonics* **2019**, *8* (3), 391–413. https://doi.org/10.1515/nanoph-2018-0219.

(79) Fornasaro, S.; Bonifacio, A.; Marangon, E.; Buzzo, M.; Toffoli, G.; Rindzevicius, T.; Schmidt, M. S.; Sergo, V. Label-Free Quantification of Anticancer Drug Imatinib in Human Plasma with Surface Enhanced Raman Spectroscopy. *Anal. Chem.* **2018**, *90* (21), 12670–12677. https://doi.org/10.1021/acs.analchem.8b02901.

(80) Chen, C.; Liu, W.; Tian, S.; Hong, T. Novel Surface-Enhanced Raman Spectroscopy Techniques for DNA, Protein and Drug Detection. *Sensors (Basel).* **2019**, *19* (7). https://doi.org/10.3390/s19071712.

(81) Tian, F.; Conde, J.; Bao, C.; Chen, Y.; Curtin, J.; Cui, D. Gold Nanostars for Efficient in Vitro and in Vivo Real-Time SERS Detection and Drug Delivery via Plasmonic-Tunable Raman/FTIR Imaging. *Biomaterials* **2016**, *106*, 87–97. https://doi.org/https://doi.org/10.1016/j.biomaterials.2016.08.014.

(82) Sinjab, F.; Kong, K.; Gibson, G.; Varma, S.; Williams, H.; Padgett, M.; Notingher, I. Tissue Diagnosis Using Power-Sharing Multifocal Raman Micro-Spectroscopy and Auto-Fluorescence Imaging. *Biomed. Opt. Express* **2016**, *7* (8), 2993–3006. https://doi.org/10.1364/BOE.7.002993.

(83) Bocklitz, T.; Bräutigam, K.; Urbanek, A.; Hoffmann, F.; von Eggeling, F.; Ernst, G.; Schmitt, M.; Schubert, U.; Guntinas-Lichius, O.; Popp, J. Novel Workflow for Combining Raman Spectroscopy and MALDI-MSI for Tissue Based Studies. *Anal. Bioanal. Chem.* **2015**, *407*, 7865–7873. https://doi.org/10.1007/s00216-015-8987-5.

(84) Kirchberger-Tolstik, T.; Ryabchykov, O.; Bocklitz, T.; Dirsch, O.; Settmacher, U.; Popp, J.; Stallmach, A. Nondestructive Molecular Imaging by Raman Spectroscopy vs. Marker Detection by MALDI IMS for an Early Diagnosis of HCC. *Analyst* **2021**, *146* (4), 1239–1252. https://doi.org/10.1039/D0AN01555E.

(85) Lasch, P.; Noda, I. Two-Dimensional Correlation Spectroscopy for Multimodal Analysis of FT-IR, Raman, and MALDI-TOF MS Hyperspectral Images with Hamster Brain Tissue. *Anal. Chem.* **2017**, *89*, 5008–5016. https://doi.org/10.1021/acs.analchem.7b00332.

(86) Jadoul, L.; Malherbe, C.; Calligaris, D.; Longuespée, R.; Gilbert, B.; Eppe, G.; De Pauw, E. Matrix-Assisted Laser Desorption/Ionization Mass Spectrometry and Raman Spectroscopy: An Interesting Complementary Approach for Lipid Detection in Biological Tissues. *Eur. J. Lipid Sci. Technol.* **2014**, *116* (8), 1080–1086. https://doi.org/https://doi.org/10.1002/ejlt.201300198.

(87) Smith, G. P. S.; McGoverin, C. M.; Fraser, S. J.; Gordon, K. C. Raman Imaging of Drug Delivery Systems. *Adv. Drug Deliv. Rev.* **2015**, *89*, 21–41. https://doi.org/10.1016/j.addr.2015.01.005.

(88) Naemat, A.; Elsheikha, H. M.; Boitor, R. A.; Notingher, I. Tracing Amino Acid Exchange during Host-Pathogen Interaction by Combined Stable-Isotope Time-Resolved Raman Spectral Imaging. *Sci. Rep.* **2016**, *6*, 20811. https://doi.org/10.1038/srep20811.

(89) Larion, M.; Dowdy, T.; Ruiz-Rodado, V.; Meyer, M. W.; Song, H.; Zhang, W.; Davis, D.; Gilbert, M. R.; Lita, A. Detection of Metabolic Changes Induced via Drug Treatments in

Live Cancer Cells and Tissue Using Raman Imaging Microscopy. *Biosensors* **2019**, *9* (1). https://doi.org/10.3390/bios9010005.

(90) Sinjab, F.; Elsheikha, H. M.; Dooley, M.; Notingher, I. Induction and Measurement of the Early Stage of a Host-Parasite Interaction Using a Combined Optical Trapping and Raman Microspectroscopy System. *J. Biophotonics* **2020**, *13* (2), e201960065. https://doi.org/https://doi.org/10.1002/jbio.201960065.

(91) Wang, J.; Lin, K.; Hu, H.; Qie, X.; Huang, W. E.; Cui, Z.; Gong, Y.; Song, Y. In Vitro Anticancer Drug Sensitivity Sensing through Single-Cell Raman Spectroscopy. *Biosensors* **2021**, *11* (8). https://doi.org/10.3390/bios11080286.

(92) Heidari Torkabadi, H.; Bethel, C. R.; Papp-Wallace, K. M.; de Boer, P. A. J.; Bonomo, R. A.; Carey, P. R. Following Drug Uptake and Reactions inside Escherichia Coli Cells by Raman Microspectroscopy. *Biochemistry* **2014**, *53* (25), 4113–4121. https://doi.org/10.1021/bi500529c.

(93) Franzen, L.; Anderski, J.; Windbergs, M. Quantitative Detection of Caffeine in Human Skin by Confocal Raman Spectroscopy - A Systematic in Vitro Validation Study. *Eur. J. Pharm. Biopharm.* **2015**, *95*, 110–116. https://doi.org/10.1016/j.ejpb.2015.03.026.

(94) Galler, K.; Requardt, R. P.; Glaser, U.; Markwart, R.; Bocklitz, T.; Bauer, M.; Popp, J.; Neugebauer, U. Single Cell Analysis in Native Tissue: Quantification of the Retinoid Content of Hepatic Stellate Cells. *Sci. Rep.* **2016**, *6*. https://doi.org/10.1038/srep24155.

(95) Yildirim, T.; Matthäus, C.; Press, A. T.; Schubert, S.; Bauer, M.; Popp, J.; Schubert, U. S. Uptake of Retinoic Acid-Modified PMMA Nanoparticles in LX-2 and Liver Tissue by Raman Imaging and Intravital Microscopy. *Macromol. Biosci.* **2017**, *17* (10). https://doi.org/10.1002/mabi.201700064.

(96) Chuchuen, O.; Henderson, M. H.; Sykes, C.; Kim, M. S.; Kashuba, A. D. M. Quantitative Analysis of Microbicide Concentrations in Fluids , Gels and Tissues Using Confocal Raman Spectroscopy. **2013**, *8* (12), 1–23. https://doi.org/10.1371/journal.pone.0085124.

(97) Liston, D. R.; Davis, M. Clinically Relevant Concentrations of Anticancer Drugs: A Guide for Nonclinical Studies. *Clin. cancer Res. an Off. J. Am. Assoc. Cancer Res.* **2017**, *23* (14),

3489–3498. https://doi.org/10.1158/1078-0432.CCR-16-3083.

(98) Masia, F.; Glen, A.; Stephens, P.; Borri, P.; Langbein, W. Quantitative Chemical Imaging and Unsupervised Analysis Using Hyperspectral Coherent Anti-Stokes Raman Scattering Microscopy. **2013**. https://doi.org/10.1021/ac402303g.

(99) Fisusi, F. A.; Siew, A.; Chooi, K. W.; Okubanjo, O.; Garrett, N.; Lalatsa, K.; Serrano, D.; Summers, I.; Moger, J.; Stapleton, P.; Satchi-Fainaro, R.; Schätzlein, A. G.; Uchegbu, I. F. Lomustine Nanoparticles Enable Both Bone Marrow Sparing and High Brain Drug Levels - A Strategy for Brain Cancer Treatments. *Pharm. Res.* **2016**, *33* (5), 1289–1303. https://doi.org/10.1007/s11095-016-1872-x.

(100) Garrett, N. L.; Lalatsa, A.; Begley, D.; Mihoreanu, L.; Uchegbu, I. F.; Schätzlein, A. G.; Moger, J. Label-Free Imaging of Polymeric Nanomedicines Using Coherent Anti-Stokes Raman Scattering Microscopy. *J. Raman Spectrosc.* **2012**, *43* (5), 681–688. https://doi.org/10.1002/jrs.3170.

(101) Belsey, N. A.; Garrett, N. L.; Contreras-Rojas, L. R.; Pickup-Gerlaugh, A. J.; Price, G. J.; Moger, J.; Guy, R. H. Evaluation of Drug Delivery to Intact and Porated Skin by Coherent Raman Scattering and Fluorescence Microscopies. *J. Control. Release* **2014**. https://doi.org/10.1016/j.jconrel.2013.11.002.

(102) Belsey, N. A.; Contreras-Rojas, L. R.; Guy, R. H. Imaging Drug Delivery to Skin with Coherent Raman Scattering Microscopy. *Non Invasive Diagnostic Tech. Clin. Dermatology* **2014**, 225–231. https://doi.org/10.1007/978-3-642-32109-2_20.

(103) Zhang, L.; Shi, L.; Shen, Y.; Miao, Y.; Wei, M.; Qian, N.; Liu, Y.; Min, W. Spectral Tracing of Deuterium for Imaging Glucose Metabolism. *Nat. Biomed. Eng.* **2019**, *3* (5), 402–413. https://doi.org/10.1038/s41551-019-0393-4.

(104) Krafft, C.; Diderhoshan, M. A.; Recknagel, P.; Miljkovic, M.; Bauer, M.; Popp, J. Crisp and Soft Multivariate Methods Visualize Individual Cell Nuclei in Raman Images of Liver Tissue Sections. *Vib. Spectrosc.* **2011**, *55* (1), 90–100. https://doi.org/10.1016/j.vibspec.2010.09.003.

(105) Kochan, K.; Marzec, K. M.; Chruszcz-Lipska, K.; Jasztal, A.; Maslak, E.; Musiolik, H.;

Chłopicki, S.; Baranska, M. Pathological Changes in the Biochemical Profile of the Liver in Atherosclerosis and Diabetes Assessed by Raman Spectroscopy. *Analyst* **2013**, *138* (14), 3885–3890. https://doi.org/10.1039/C3AN00216K.

(106) Patil, C. A.; Pence, I. J.; Lieber, C. A.; Mahadevan-Jansen, A. 1064nm Dispersive Raman Spectroscopy of Tissues with Strong Near-Infrared Autofluorescence. *Opt. Lett.* **2014**, *39* (2), 303–306. https://doi.org/10.1364/OL.39.000303.

(107) Dochow, S.; Bergner, N.; Matthäus, C.; Praveen, B. B.; Ashok, P. C.; Mazilu, M.; Krafft, C.; Dholakia, K.; Popp, J. Etaloning, Fluorescence and Ambient Light Suppression by Modulated Wavelength Raman Spectroscopy. *Biomed. Spectrosc. Imaging* **2012**, *1* (4), 383–389.

(108) Cadusch, P. J.; Hlaing, M. M.; Wade, S. A.; Mcarthur, S. L.; Stoddart, P. R. Improved Methods for Fluorescence Background Subtraction from Raman Spectra. *J. Raman Spectrosc.* **2013**, *44* (11), 1587–1595.

(109) Morris, M. D.; Finney, W. F. Recent Developments in Raman and Infrared Spectroscopy and Imaging of Bone Tissue. *Spectroscopy* **2004**, *18*, 155–159.

(110) Venkatakrishna, K.; Kurien, J.; Pai, K.; Kumar, N.; Chilakapati, M. K.; Ullas, G.; Kartha, V. Optical Pathology of Oral Tissue: A Raman Spectroscopy Diagnostic Method. *Curr. Sci.* **2001**.

(111) Stone, N.; Kendall, C.; Shepherd, N.; Crow, P.; Barr, H. Near-Infrared Raman Spectroscopy for the Classification of Epithelial Pre-Cancers and Cancers. *J. Raman Spectrosc.* **2002**, *33* (7), 564–573. https://doi.org/10.1002/jrs.882.

(112) Swanson, L. *Brain Maps: Structure of the Rat Brain*; Gulf Professional Publishing, 2004.

(113) Anna, I.; Bartosz, P.; Lech, P.; Halina, A. Novel Strategies of Raman Imaging for Brain Tumor Research. *Oncotarget* **2017**, *8* (49), 85290–85310. https://doi.org/10.18632/oncotarget.19668.

(114) Armbruster, D. A.; Pry, T. Limit of Blank, Limit of Detection and Limit of Quantitation. *Clin. Biochem. Rev.* **2008**, *29 Suppl 1* (August), S49-52.

(115) Schlücker, S.; Schaeberle, M. D.; Huffman, S. W.; Levin, I. W. Raman Microspectroscopy: A Comparison of Point, Line, and Wide-Field Imaging Methodologies. *Anal. Chem.* **2003**, *75*, 4312–4318. https://doi.org/10.1021/ac034169h.

(116) Takamori, S.; Kong, K.; Varma, S.; Leach, I.; Williams, H. C.; Notingher, I. Optimization of Multimodal Spectral Imaging for Assessment of Resection Margins during Mohs Micrographic Surgery for Basal Cell Carcinoma. *Biomed. Opt. Express* **2015**, *6* (1), 98–111. https://doi.org/10.1364/BOE.6.000098.

(117) Shipp, D. W.; Rakha, E. A.; Koloydenko, A. A.; Macmillan, R. D.; Ellis, I. O.; Notingher, I. Intra-Operative Spectroscopic Assessment of Surgical Margins during Breast Conserving Surgery. *Breast Cancer Res.* **2018**, *20* (1), 69. https://doi.org/10.1186/s13058-018-1002-2.